

**NANOFABRICATED BIOHYBRID
STRUCTURES FOR CONTROLLED
DRUG DELIVERY**

Alma Dudia

The work was carried out at the Biophysical Engineering Group, Faculty of Science and Technology, Institute for Biomedical Technology (BMTI), University of Twente, P.O. Box 217, 7500 AE, Enschede, The Netherlands.

The research presented in this thesis was financially supported by the Institute for Biomedical Technology (BMTI) and Biophysical Engineering Group, Faculty of Science and Technology, University of Twente.

A. Dudia

Nanofabricated Biohybrid Structures for Controlled Drug Delivery
Proefschrift Universiteit Twente, Enschede.

ISBN 978-90-365-2535-0

Copyright © 2007 by Alma Dudia

Printed by GILDEPRINT DRUKKERIJEN B.V., Enschede.

NANOFABRICATED BIOHYBRID STRUCTURES FOR CONTROLLED DRUG DELIVERY

PROEFSCHRIFT

ter verkrijging van
de graad van doctor aan de Universiteit Twente,
op gezag van de rector magnificus,
prof. dr. W.H.M. Zijm,
volgens besluit van het College voor Promoties
in het openbaar te verdedigen
op woensdag 4 juli 2007 om 15:00 uur

door

Alma Dudia
geboren op 1 maart 1973
te Peqin, Albanië

Dit proefschrift is goedgekeurd door

promotor:	prof. dr. V. Subramaniam
assistent-promotor:	dr. ir. J.S. Kanger

to Aurel and my parents

Contents

1. Introduction

1.1. General Introduction	3
1.2. Drug delivery systems	4
1.2.1. Current systems	4
1.2.2. DDV characteristics	7
1.3. Motivation for developing hybrid vehicles	8
1.4. Designing a hybrid spherical vehicle	9
1.5. Goal of the thesis	10

2. Introduction to the techniques

2.1. Introduction	17
2.2. Nanofabrication	17
2.2.1. Reactive Ion Etching	17
2.2.2. Phase Separation Micro-Molding	17
2.2.3. Focused ion beam drilling	18
2.3. Optical tweezers	19
2.4. Voltage-clamp	20
2.5. Imaging techniques	21
2.5.1. Epifluorescence microscopy	21
2.5.2. Total internal reflection fluorescence microscopy	22
2.5.3. Confocal laser scanning microscopy	23
2.5.4. Atomic force microscopy	24

3. Fabrication of membrane platforms

3.1. Introduction	29
3.2. Requirements	29
3.3. Substrate fabrication	30
3.4. Lipid composition	31
3.5. Brushing method for Black Lipid Membrane formation	32
3.5.1. Theory	32

- 3.5.2. Materials and methods 34
- 3.5.3. Results and discussion 35
- 3.6. Lipid Vesicles 38
 - 3.6.1. Materials and methods 39
 - 3.6.2. Results 40
 - 3.6.3. Membrane characterization 42
 - 3.6.3.1. Atomic Force Microscopy 43
 - 3.6.3.2. Electrical measurements on a free-standing BiLM . . . 44
- 3.7. Conclusions 48

4. Controlled deposition of an artificial bilayer lipid membrane onto microwells in a flat substrate

- 4.1. Introduction 55
- 4.2. Manipulation and controlled rupture of the vesicles 56
 - 4.2.1. OT manipulation 56
 - 4.2.2. Controlled pattern formation of membrane patches 62
- 4.3. Characterization of vesicle collapse 62
 - 4.3.1. Vesicle size vs. membrane patch area 63
 - 4.3.2. Dynamics of vesicle rupture 64
- 4.4. Artificial BiLM deposition onto microwells in a flat substrate 66
 - 4.4.1. Substrate fabrication 66
 - 4.4.2. Hole sealing with an artificial BiLM 67
- 4.5. Conclusions 72

5. Biofunctionalized membranes on flat substrates

- 5.1. Introduction 79
- 5.2. MscL channel protein 80
- 5.3. Theory: Passive diffusion through a nanopore 82
- 5.4. Materials and methods 85
- 5.5. Results and discussion 86
- 5.6. Conclusions 96

6. Development of the scaffold

- 6.1. Introduction 101
- 6.2. Choice of the scaffold 101
- 6.3. Materials and methods 103

6.4. Results 105
 6.5. Discussion and conclusions 108

7. Nanofabricated biomimetic devices

7.1. Introduction 113
 7.2. Methods to load scaffolds 113
 7.3. Modeling the diffusion through a nanohole in a scaffold 114
 7.4. Materials and methods 116
 7.5. Results and discussion 118
 7.5.1. Loading of the scaffold 118
 7.5.2. Sealing the scaffold with a lipid membrane 121
 7.5.3. Functionalization of the spherical hybrid vehicles 124
 7.6. Conclusions 126

8. Conclusions and outlook

8.1. Conclusions 131
 8.2. Outlook 133
 8.2.1. Improvement of the throughput 133
 8.2.2. Further development of the spherical hybrid vehicle 135
 8.2.3. Hybrid flat platforms 135

Appendices 139

Summary 149

Samenvatting 151

List of abbreviations 153

Acknowledgments 154

Publications 155

CHAPTER ONE

INTRODUCTION

In this chapter, we give a brief introduction to the field of artificial drug delivery systems, and introduce a new approach to a biohybrid drug delivery vehicle.

1.1 General Introduction

Diseases can be treated by administration of drugs that are delivered orally or intravenously. One of the problems in drug delivery is the overdoses caused in the first stage of drug administration which gives side effects in the organism. Also, the use of toxic drugs in treatment of diseases such as tumors could damage the normal cells, e.g. in chemotherapy [1].

Development of artificial vehicles that carry a drug and are aimed for *in vivo* targeted drug delivery and controlled drug release is a key target of intensive research and very important for future medical science.

It is beneficial to target and deliver a pharmaceutical agent locally to a pathological region or to specific body sites to either modify a target cell and/or cell function, or to fully destroy that cell without affecting and damaging the other cells. One of the approaches for targeted drug delivery is the use of hybrid vehicles, which are a combination of non-biological and biological elements, e.g. polymers and biomolecules. This approach of drug delivery vehicles (DDV) allows achievement of specific functionality such as targeted drug delivery, controlled drug release, and pharmaceutical agent transport [2,3]. Hybrid vehicle applications include tumor therapy [4-6], gene therapy [7-10], sustained and controlled release [11], artificial cell such as red blood cell substitute [12], correction of enzyme deficiency [13], and diagnostics [14,15].

Most systems developed so far are those based on liposomes and polymersomes. Although liposomes support a natural biofunctionality of biomolecules [16] and enable immobilization of different types of biomolecules in the lipid scaffold, their major drawback is the short temporal stability [17,18]. Biodegradable polymersomes, on the other hand, provide a high stability and allow tuning of vehicle surface properties [18]. However, since they are non-natural supports for biomolecules, denaturation of biomolecules may occur, and therefore have limited biofunctionalization ability.

To improve the performance of the existing systems, i.e. liposomes and polymersomes, we have designed a new hybrid DDV, based on a polymeric scaffold and lipid membranes, that benefits from the advantages of both systems. This approach could yield a hybrid DDV that is stable, inert, biodegradable, and supports biofunctionalization.

1.2 Drug delivery systems

Principal features of a drug delivery vehicle are depicted schematically in Figure 1.1. The structure may consist of the vehicle body, which can be a shell (hollow scaffold) or a solid material matrix, a payload that is the therapeutic agent carried by the vehicle body, a bioinert (stealth) surface that inhibits an immune response, and biofunctional units that provide biospecific targeting and functionality.

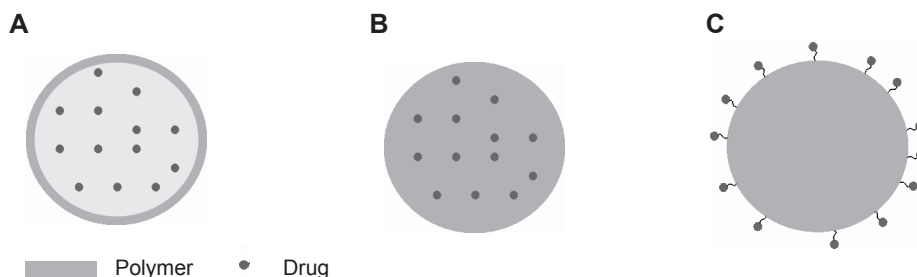


Figure 1.1. Schematic representation of three basic DDVs consisting of (A) a hollow carrier loaded with a drug, (B) a matrix carrier having the payload distributed in the matrix or (C) attached on the matrix surface.

A pharmaceutical agent can be encapsulated inside a scaffold, integrated in the scaffold matrix, or attached on the surface of the scaffold. Encapsulation has the advantage of providing a higher drug carrying capacity. In this section we briefly discuss commonly used drug delivery systems.

1.2.1 Current systems

Liposomes. Liposomes are composed of lipid bilayers enclosing aqueous solution. The properties of liposomes, such as rigidity (fluidity) and membrane charge are determined by the lipid composition [3]. The liposome shell closely resembles the plasma cell membrane and has been the rationale for liposome use as a tool in biology, biochemistry and medicine.

Liposomes are used as DDVs in pharmacology and medicine for cancer treatment and gene therapy [4]. They have been explored as carriers for sustained, controlled, and targeted drug delivery [1-4,19-24]. Different payloads have been encapsulated into the liposomes, including different aqueous and toxic agents [21], macromolecules such as antigens [22], DNA [25], and cell extracts [24].

An advantage of liposomes is the higher capacity of the drug carrier due to encapsulation as compared to drug attachment to a polymer surface. In sustained release, encapsulation prevents the early dilution and degradation of the payload as compared to a free drug in solution and allows a prolonged release of the payload, preventing overdoses in the first stage of release. Biocompatibility, the ability to incorporate different biomolecules, and the availability of a range of sizes, starting from ~ 25 nm, are some other advantages of liposomes. Some of their drawbacks are limited stability and leakage of the liposome contents, e.g. due to osmolarity [17,18,20].

Polymersomes. Polymer technology has had a high impact in pharmacology and medicine. The most attractive polymer vehicles are polymersomes. They are made of block-copolymers that form an amphiphilic thin membrane similar to liposomes. Potential applications of polymersomes include sustained, controlled, and targeted drug delivery for cancer and gene therapy. In sustained and controlled release, carriers that maintain a long circulation time and continuous release of a payload such as proteins [11] have been realized. In gene therapy, DNA loaded capsules [7] and cationic nanocapsules [26] have been developed for DNA delivery. For cancer therapy, systems for targeting the tumor by enhancing the selectivity [27] have been demonstrated.

An advantage of polymersomes is that their properties such as permeability, elasticity, and toughness can be controlled by tuning the membrane thickness [18]. Most interesting are polymersomes that are biodegradable and have a longer lifetime (e.g. two fold longer [28]) as compared to liposomes. The possibility to tailor polymer properties such as hydrophilicity and lifetime, and their biocompatibility enables designing a drug delivery vehicle with predefined scaffold properties. Various porous and nonporous biodegradable polymersomes have been developed [29] since the porosity and biodegradability of polymersomes influences the kinetics of the release.

However, since polymers are not natural supports for biomolecules and are relatively thick compared to lipid membranes, it is not easy to integrate biomolecules. Because the proteins are not in their natural (membrane) environment there is a high risk for biomolecule denaturation and malfunction.

Solid matrix particles. Matrix particles, also called nano- and microspheres, are matrix systems within which a pharmaceutical agent is physically and uniformly dispersed. They are common systems for controlled drug release. The matrix material can consist of polymers [30], proteins [31], or polysaccharides [32]. Efforts have been made to develop systems for a controlled and sustained delivery of a drug to maintain a constant therapeutic level [33-35]. Porous polymer microcarriers with a drug dispersed in the polymer matrix, and which show zero-order release kinetics, have been developed [33]. Biodegradable matrix particles have also been developed. Combination of porous and biodegradable polymer

systems allows control of drug release rates [2]. The release kinetics depends upon drug solubility in the polymer matrix or in the pore for a porous matrix. Specific targeting is achieved by conjugation to the carriers of cell specific ligands that can be recognized by the surface cell receptors. Of interest is the development of ligand-coupled biodegradable nanospheres (matrix particles in nanometer scale) [35,36].

Such systems are easy to fabricate compared to the capsules and there is no risk of an overdose caused by the rupture of the capsule membrane. The small size enables penetration into smaller capillaries and an efficient drug accumulation at the cell target sites. In the case of long-circulating polymeric biodegradable nanospheres, processes such as swelling, degradation, and erosion of the polymer matrix induce morphological and surface changes that are favorable for opsonization and phagocytosis.

Micelles. Amphiphilic block copolymers can self associate to form micelles with a core-shell type architecture. The micelles consist of a hydrophobic core formed by hydrophobic polymer segments and a hydrophilic shell formed by biocompatible polymers such as PEO (poly (ethylene oxide)) [37]. The micelles do not dissociate in physiological environments and have sizes in the nanometer range, making them useful for intravenous application [38]. The particles have been used in sustained, targeted drug delivery, and diagnostics [39,40]. The hydrophilic surface minimizes the uptake of the particles by the reticulo-endothelial system, prolonging the particle circulation time [41]. Immunomicelles (ligand conjugated micelles) have been developed that can specifically bind to tumors [42]. Compared to the free drug, micelle-incorporated drugs may accumulate to a greater extent into tumors and much less in non-targeted areas [43].

Magnetic particles. Magnetic particles have been used as injectable drug carriers [44]. They are made of iron oxide and metallic iron and have a drug or ligands adsorbed on the surface. Applications in drug release are achieved by desorption of the therapeutic drugs (e.g. doxorubicin) from the particles to a target, e.g. tumor [44]. To do so, the particles are localized and retained in the target by means of an external permanent magnet. In diagnostics, immunolabelled magnetic particles have been used to detect a disease cell [45].

Silicon particles. Silicon particles are used for oral drug delivery [46]. In addition, silicon and silicon dioxide particles of micrometer-size such as hemispherical shells and asymmetrical squares containing nanopores have been developed as injectable particles for smart targeting [47,48]. *In vitro* tests with these particles resulted in safe circulation of the particles in mouse vasculature models when particles smaller than 6 μm were injected. However, being an inorganic material, silicon particles are not as attractive as polymers.

1.2.2 DDV characteristics

Stealth surface

To achieve a long circulation time of a DDV, it is important to avoid an immunoresponse by the reticulo-endothelial system (RES). Another problem is particle opsonization, i.e. the adsorption of plasma proteins onto particle surface, resulting in particle recognition by phagocytes. These problems could be coped with by engineering a surface coat (an inert surface) that avoids RES recognition and reduces the opsonization of plasma proteins. Such a surface is usually realized by coating the DDV surface with a nonionic and hydrophilic material such as polyethylene glycol (PEG). PEG-coated immunoliposomes have been developed [4,42,49], resulting in a reduced clearance of the liposomes from the RES system and in a significantly prolonged circulation time. Subsequently, a sustained and efficient drug release could be obtained. PEG coating is applied on several drug delivery systems such as polymersomes [7,50], solid matrix particles [30], and micelles [41,42,51,52] and has improved the particle functionality and properties.

Targeting and release mechanisms

The DDVs can be categorized as being active and passive. Active DDVs introduce bioactivity during their functioning. For example, they use specific antibodies to detect a disease cell such as tumors [5,53]. Another form of active bioactivity could be the controlled drug release through biomolecules such as channel proteins. Potential applications include smart drug delivery [7,54], microsurgery (e.g. in gene therapy [7]), and diagnostics [55]. Active drug targeting allows high efficiency of drug release, prevention of side effects in the cells due to overdoses, and economical use of pharmaceutical agents. Passive DDVs on the other hand do not introduce any bioactivity during their functioning. Drug release from such systems is based on physical-chemical phenomena such as diffusion.

Some drug release mechanisms are introduced below.

Diffusion. This is the most common phenomena in oral drug delivery systems, such as capsules and matrix-porous particles. The solute concentration gradient is the driving mechanism. Exchange of water and solutes between particle interior and exterior can occur through the porous structure until a concentration equilibrium is reached. In biodegradable systems, the release kinetics is governed by both the diffusion and polymer biodegradation (erosion) processes [30].

Dissolution. Such a process is characterized by a phase erosion of the polymer carrier that is associated with dissolution of the macromolecular chains. This approach has been used for the development of swelling-controlled release particles [34]. Here, a drug dispersed in a polymer matrix dissolves as water penetrates the polymer and a gel layer is formed on the particle surface. The layer thickness controls the drug delivery. By controlling of the swelling process, one can design a swelling-controlled release particle.

Osmolarity. This is a typical process associated with liposomes and polymersomes when merged in a solution with physiological characteristics that are different from the encapsulated solution [18,20]. The fluidity of their membranes allows the exchange of water and small solutes between the particle interior and exterior medium. Accumulation of liposomes, e.g. in a tumor, enables a local increase of a pharmaceutical agent on the target tissue due to osmolarity and hence, a more efficient drug delivery.

pH. pH mechanism has also been used in controlled drug release. It is known that the pH round a tumor is lower than the normal physiological pH [53]. Incorporation of pH sensitive proteins in stable vesicle particles such as polymersomes has resulted in a pH controlled protein opening and subsequently, a local drug release as demonstrated *in vitro* [50].

1.3 Motivation for developing hybrid vehicles

So far, the most developed and studied drug delivery vehicles are liposomes and polymersomes. The major drawbacks of these systems are the short temporal stability (liposomes) and limited biofunctionalization ability of commonly used nonbiological supports (polymersomes).

The performance of the current systems could be improved by combining the advantages of both existing systems. This goal could be achieved by using a polymeric scaffold combined with a lipid membrane. A polymer-based scaffold could provide a structure that is more stable than liposomes, is biocompatible, biodegradable, and has desired surface properties such as hydrophilicity [18]. For applications in targeted drug delivery and controlled release, biomolecules play a crucial role in targeting and in release mechanisms. Lipid membranes could be a natural support for these biomolecules, allowing functionality and vehicle biomodification with different types of biomolecules.

We introduce a new approach of a hybrid vehicle consisting of a nonbiological polymer scaffold and lipid membranes modified with biomolecules.

1.4 Designing a hybrid spherical vehicle

The aim of this work is to develop a freestanding spherical hybrid vehicle on the (sub-micron) cellular scale that carries a payload, can micro-circulate, and can specifically deliver the payload to a target, e.g. a disease cell, without being rejected by the immune system.

The main components of such a hybrid vehicle are the scaffold with a hole, the membrane that seals the hole, and the functional biomolecules that are incorporated in the membrane, as depicted schematically in Figure 1.2.

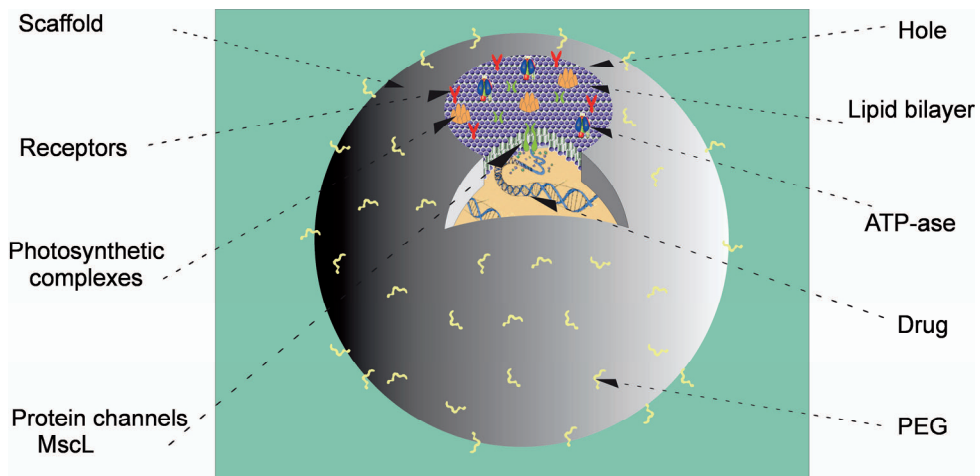


Figure 1.2. Schematic representation of a hybrid DDV, consisting of an impermeable hollow polymeric scaffold with a single small opening and a payload such as a drug loaded inside the scaffold. An artificial bilayer lipid membrane, with functional biomolecules embedded, seals the hole. Functional biomolecules, e.g. MscL channel protein, ATPase, photosynthetic complexes, and receptors, are embedded in the bilayer. PEG coating of the surface is provided to prevent nonspecific binding. Typical dimension of this structure is $\sim 1 \mu\text{m}$; hole dimension is in the submicrometer range.

The scaffold separates the inner content of the vehicle from the environment, in analogy with the compartmentalization functionality of a real cell membrane. It will carry a payload such as a drug, biomolecules, proteins, or DNA. The scaffold should be stable and biocompatible in order not to alter the properties of the biological medium. It will be made of polymer material. Preferably, the polymer should be biodegradable. The scaffold should also not be leaky to avoid any

uncontrolled release through its wall. This can be achieved by choosing an impermeable polymer material. The release will occur only through the designed hole in the scaffold. The hole is also designed for loading purposes. It will be sealed by a stable lipid membrane to prevent any uncontrolled release of the vehicle content due to diffusion that might occur through an open hole. Small hole dimensions (in sub-micron range) are desirable to achieve a high stability of the lipid membrane [56].

The membrane will also serve as a natural support for the biomolecules that are required for the functionality of the vehicle such as targeting ability, motility, and release. Incorporation of biomolecules that recognize a specific disease site based on, e.g. antibody-antigen and enzymatic interaction, will provide targeting functionality of the vehicle in a bio-environment. A PEG vehicle coating can provide an inert surface. Micro-circulation and directed movements of the vehicle could be realized by incorporating biomolecules that produce energy in combination with motor proteins that convert the energy into mechanical movement. Micro-circulation properties impose limitations to vehicle size. In the membrane, biomolecules such as channel proteins will be incorporated to enable a controlled release. In our hybrid vehicle, we are going to incorporate at least one biomolecule to deliver drugs in a controllable manner.

1.5 Goal of the thesis

The goal of this thesis is the development of robust and stable spherical hybrid vehicles that benefit from both existing biological and nonbiological systems and are aimed for multipurpose use such as drug delivery, diagnostics, and sensory applications.

Toward achievement of this goal, the work will be focused on the development of:

- Hybrid flat platforms, to enable system characterization in analogy with spherical systems.
- Spherical scaffolds, consisting of scaffold fabrication as the basic element in our design.
- Biofunctionalized spherical scaffolds including realization of a hybrid spherical device, promoted by the functionality of a biomolecule embedded in the membrane that seals a nanohole in a polymeric scaffold.

References

- [1] L.H. Lindner, M.E. Eichhorn, H. Eibl, N. Teichert, M. Schmitt-Sody, R.D. Issels, and M. Dellian, Novel Temperature-Sensitive Liposomes with Prolonged Circulation Time, *Clinical Cancer Research*, 2004, **10**, 2168-2178.

-
- [2] R. Langer, Drug delivery and targeting, *Nature*, 1998, **392**, 5-10.
- [3] S.K. Sahoo and V. Labhasetwar, Nanotech approaches to drug delivery and imaging, *Drug Discovery Today*, 2003, **8**, 1112-1120.
- [4] M.C. Woodle, Controlling liposome blood clearance by surface-grafted polymers, *Advanced Drug Delivery Reviews*, 1998, **32**, 139-152.
- [5] J.W. Park, D.B. Kirpotin, K. Hong, R. Shalaby, Y. Shao, U.B. Nielsen, J.D. Marks, D. Papahadjopoulos, and C.C. Benz, Tumor targeting using anti-her2 immunoliposomes, *Journal of Controlled Release*, 2001, **74**, 95-113.
- [6] C.J.T. Hoes *et al*, Synthesis and biological evaluation of Immunoconjugates of adriamycin and a human IgM linked by poly[N⁵-(2-hydroxyethyl)-L-glutamine], *Journal of Controlled Release*, 1996, **38**, 245-266.
- [7] A. Graff, M. Sauer, P.V. Gelder, and W. Meier, Virus-assisted loading of polymer nanocontainer, *PNAS*, 2002, **99** (8), 5064-5068.
- [8] T.M.S. Chang, Artificial Cells with Emphasis on Cell Encapsulation of Genetically Engineered Cells, *Artificial Organs*, 1998, **22**, 958-965.
- [9] E.K. Gaidamakova, M.V. Backer, and J.M. Backer, Molecular vehicle for target-mediated delivery of therapeutics and diagnostics, *Journal of Controlled Release*, 2001, **74**, 341-347.
- [10] W.F. Anderson, Human gene therapy, *Nature*, 1998, **392**, 25-30.
- [11] H. Sah, R. Toddywala, and Y.W. Chien, Continuous release of proteins from biodegradable microcapsules and in vivo evaluation of their potential as a vaccine adjuvant, *Journal of Controlled Release*, 1995, **35**, 137-144.
- [12] T.M.S. Chang, *Artificial Cells*, Springfield: C.C. Thomas, 1972.
- [13] S. Bruni and T.M.S. Chang, Kinetic Analysis of UDP-Glucuronosyltransferase in Bilirubin Conjugation by Encapsulated Hepatocytes for Transplantation into Gunn Rats. *Artificial Organs*, 1995, **19**, 449-457.
- [14] V.P. Torchilin, V.S. Trubetskoy, A.M. Milshteyn, J. Canillo, G.L. Wolf, M.I. Papisov, A.A. Bogdanov, J. Narula, B. An Khaw, and V.G. Omelyanenko, Targeted delivery of diagnostic agents by surface-modified liposomes, *Journal of Controlled Release*, 1994, **28**, 45-48.
- [15] R. Duncan, S. Dimitrijevic, and E.G. Evagorou, The role of polymer conjugates in the diagnoses and treatment of cancer, *STP Pharma Sci.*, 1996, **6**, 237-263.
- [16] G. Steinberg-Yfrach, J-L. Rigaud, E.N. Durantini, A.L. Moore, D. Gust, and T.A. Moore, Light-driven production of ATP catalysed by F₀F₁-ATP synthase in an artificial photosynthetic membrane, *Nature*, 1998, **392**, 479-482.
- [17] D.D. Lasic, *Liposomes: from physics to applications*, Elsevier Science Publishers B.V., Amsterdam, The Netherlands, ISBN 0 444 89548 5, 1993.
- [18] D.E. Discher and A. Eisenberg, Polymer Vesicles, *Science*, 2002, **297**, 967-973.
- [19] J.W. Park, K. Hong, D. Kirpotin, D. Papahadjopoulos, and C.C. Benz, Immunoliposomes for cancer treatment, *Adv. Pharmacol.*, 1997, **40**, 399-435.
- [20] J. Mönkkönen, J. Liukkonen, M. Taskinen, T.D. Heath, and A. Urtti, Studies on liposome formulations for intra-articular delivery of clodronate, *Journal of Controlled Release*, 1995, **35**, 145-154.
- [21] D.D. Spragg, D.R. Alford, R. Greferath, C.E. Larsen, K-D. Lee, G.C. Gurtner, M.I. Cybulsky, P.F. Tosi, C. Nicolau, and M.A. Gimbrone Jr., Immunotargeting of liposomes to activated vascular endothelial cells: A strategy for site-selective delivery in the cardiovascular system, *Proc. Natl. Acad. Sci. USA*, 1997, **94**, 8795-8800.

- [22] K-D. Lee, Y-K. Oh, D.A. Portnoy, and J.A. Swanson, Delivery of Macromolecules into Cytosol Using Liposomes Containing Hemolysin from *Listeria monocytogenes*, *The Journal of Biological Chemistry*, 1996, **271**, 7249-7252.
- [23] V. Budker, V. Gurevich, J.E. Hagstrom, F. Bortzov, and J.A. Wolff, pH-sensitive, cationic liposomes: A new synthetic virus-like vector, *Nature Biotechnology*, 1996, **14**, 760-764.
- [24] V. Noireaux and A. Libchaber, A vesicle bioreactor as a step toward an artificial cell assembly, *Proc. Natl. Acad. Sci. USA*, 2004, **101**, 17669-17674.
- [25] O. Lambert, L. Letellier, W.M. Gelbart, and J-L. Rigaud, DNA delivery by phage as a strategy for encapsulating toroidal condensates of arbitrary size into liposomes, *Proc. Natl. Acad. Sci. USA*, 2000, **97**, 7248-7253.
- [26] K.W. Leong, H-Q. Mao, V.L. Truong-Le, K. Roy, S.M. Walsh, and J.T. August, DNA-polycation nanospheres as non-viral gene delivery vehicles, *Journal of Controlled Release*, 1998, **53**, 183-193.
- [27] D.E. Meyer, B.C. Shin, G.A. Kong, M.W. Dewhirst, and A. Chilkoti, Drug targeting using thermally responsive polymers and local hyperthermia, *Journal of Controlled Release*, 2001, **74**, 213-224.
- [28] P.J. Photos, L. Bacakova, B. Discher, F.S. Bates, and D.E. Discher, Polymer vesicles in vivo: correlation with PEG molecular weight, *Journal of controlled release*, 2003, **90**, 323-334.
- [29] G. Crotts and T.G. Park, Preparation of porous and nonporous biodegradable polymeric hollow microspheres, *Journal of Controlled Release*, 1995, **35**, 91-105.
- [30] K.S. Soppimath, T.M. Aminabhavi, A.R. Kulkarni, and W.E. Rudzinski, Biodegradable polymeric nanoparticles as drug delivery devices, *Journal of Controlled Release*, 2001, **70**, 1-20.
- [31] K. Fujioka, M. Maeda, T. Hojo, and A. Sano, Protein release from collagen matrices, *Advanced Drug Delivery Reviews*, 1998, **31**, 247-266.
- [32] S. Dumitriu and E. Chornet, Inclusion and release of proteins from polysaccharide-based polyanion complexes, *Advanced Drug Delivery Reviews*, 1998, **31**, 223-246.
- [33] W. Landgraf, N-H. Li, and J.R. Benson, Polymer Microcarrier Exhibiting Zero-Order Release, *Drug Delivery Technology*, 2003, **3**, 1-12.
- [34] B. Narasimhan and N.A. Peppas, Molecular Analysis of Drug Delivery Systems Controlled by Dissolution of the Polymer Carrier, *Journal of Pharmaceutical Sciences*, 1997, **86**, 297-304.
- [35] S.M. Moghimi, A.C. Hunter, and J.C. Murray, Long-Circulating and Target-Specific Nanoparticles: Theory to Practice, *Pharmacological Reviews*, 2001, **53**, 283-318.
- [36] A. Lamprecht, N. Ubrich, H. Yamamoto, U. Schäfer, H. Takeuchi, P. Maincent, Y. Kawashima, and C-M. Lehr, Biodegradable Nanoparticles for Targeted drug Delivery in Treatment of Inflammatory Bowel Disease, *The Journal of Pharmacology and Experimental Therapeutics*, 2001, **299**, 775-781.
- [37] M-C. Jones and J-C. Leroux, Polymeric micelles – a new generation of colloidal drug carriers, *European Journal of Pharmaceutics and Biopharmaceutics*, 1999, **48**, 101-111.
- [38] R. Savić, L. Luo, A. Eisenberg, and D. Maysinger, Micellar Nanocontainers Distribute to Defined Cytoplasmic Organelles, *Science*, 2003, **300**, 615-618.

- [39] A. Rösler, G.W.M. Vandermeulen, and H-A. Klok, Advanced drug delivery devices via self-assembly of amphiphilic block copolymers, *Advanced Drug Delivery Reviews*, 2001, **53**, 95-108.
- [40] V.S. Trubetsky, Polymeric micelles as carriers of diagnostic agents, *Advanced Drug Delivery Reviews*, 1999, **37**, 81-88.
- [41] K. Kataoka, A. Harada, and Y. Nagasaki, Block copolymer micelles for drug delivery: design, characterization and biological significance, *Advanced Drug Delivery Reviews*, 2001, **47**, 113-131.
- [42] V.P. Torchilin, A.N. Lukyanov, Z. Gao, and B. Papahadjopoulos-Sternberg, Immunomicelles: Targeted pharmaceutical carriers for poorly soluble drugs, *Proc. Natl. Acad. Sci. USA*, 2003, **100**, 6039-6044.
- [43] T. Nakanishi, S. Fukushima, K. Okamoto, M. Suzuki, Y. Matsumura, M. Yokoyama, T. Okano, Y. Sakurai, and K. Kataoka, Development of the polymer micelle carrier system for doxorubicin, *Journal of Controlled Release*, 2001, **74**, 295-302.
- [44] S. Rudge, C. Peterson, C. Vessely, J. Koda, S. Stevens, and L. Catterall, Adsorption and desorption of Chemotherapeutic drugs from a magnetically targeted carrier (MTC), *Journal of Controlled Release*, 2001, **74**, 335-340.
- [45] Y.R. Chemla, H.L. Grossman, Y. Poon, R. McDermott, R. Stevens, M.D. Alper, and J. Clarke, Ultrasensitive magnetic biosensor for homogeneous immunoassay, *Proc. Natl. Acad. Sci. USA*, 2000, **97**, 14268-14272.
- [46] M. Ferrari, P.J. Dehlinger, F.J. Martin, C.F. Grove, and D.R. Friend, Particles for oral Delivery of Peptides and Proteins, US Patent No. 6,355,270, March 12, 2002.
- [47] M.H. Cohen, K. Melnik, A.A. Boiarski, M. Ferrari, and F.J. Martin, Microfabrication of Silicon-Based Nanoporous Particulates for Medical Applications, *Biomedical Microdevices*, 2003, **5**, 253-259.
- [48] A.B. Foraker, R.J. Walczak, M.H. Cohen, T.A. Boiarski, C.F. Grove, and P.W. Swaan, Microfabricated Porous Silicon Particles Enhance Paracellular Delivery of Insulin across Intestinal Caco-2 Cell Monolayers, *Pharmaceutical research*, 2003, **20**, 110-116.
- [49] S. Zalipsky, C.B. Hansen, D.E. Lopez de Menezes, and T.M. Allen, Long-circulating polyethylene glycol-grafted immunoliposomes, *Journal of Controlled Release*, 1996, **39**, 153-161.
- [50] P. Broz, S. Driamov, J. Ziegler, N. Ben-Haim, S. Marsch, W. Meier, and P. Hunziker, Toward intelligent nanosize bioreactors: a pH switchable, channel-equipped functional polymer nanocontainer, *Nano Letters*, 2006, **6**, 2349-2353.
- [51] K. Kataoka, T. Matsumoto, M. Yokoyama, T. Okano, Y. Sakurai, S. Fukushima, K. Okamoto, and G.S. Kwon, Doxorubicin-loaded poly(ethylene glycol)-poly(β -benzyl-L-aspartate) copolymer micelles: their pharmaceutical characteristics and biological significance, *Journal of Controlled Release*, 2000, **64**, 143-153.
- [52] V.P. Torchilin, Structure and design of polymeric surfactant-based drug delivery systems, *Journal of Controlled Release*, 2001, **73**, 137-172.
- [53] K. Ulbrich and V. Šubr, Polymeric anticancer drugs with pH-controlled activation, *Advanced Drug Delivery Reviews*, 2004, **56**, 1023-1050.
- [54] F. Pasorino, D. Stuart, M. Ponzoni, T.M. Allen, Targeted delivery of antisense oligonucleotides in cancer, *Journal of Controlled Release*, 2001, **74**, 69-75.

- [55] S. Dagar, M. Sekosan, B.S. Lee, I. Rubinstein, and H. Önyüksel, Vip receptors as molecular targets of breast cancer: implications for targeted imaging and drug delivery, *Journal of Controlled Release*, 2001, **74**, 129-134.
- [56] M. Mayer, J.K. Kriebel, M.T. Tosteson, and G.M. Whitesides, Microfabricated Teflon membranes for low-noise recordings of ion channels in planar lipid bilayers, *Biophysical Journal*, 2003, **85**, 2684-2695.

CHAPTER TWO

INTRODUCTION TO THE TECHNIQUES

This chapter gives a background of the techniques used in this project for nanofabrication, nanomanipulation, characterization, and imaging of submicron objects.

2.1 Introduction

This thesis deals with nanostructuring and manipulation of submicron objects such as hollow beads and lipid vesicles, and imaging of membrane bilayers, biomolecules, and dynamic processes occurring in our hybrid system. We use advanced techniques for nanofabrication, manipulation, and imaging. In this chapter, I describe several techniques that are used throughout the thesis.

2.2 Nanofabrication

2.2.1 Reactive Ion Etching

Reactive ion etching (RIE) technique plays an important role in etching small geometries. RIE is based on the interaction of gaseous species with the solid surfaces to be etched to form volatile products [1,2].

Some advantages of this technique are the achievement of etch directionality without using the crystal orientation as in the case of wet etching and the capability to truly transfer lithographically defined photoresist patterns. A drawback is its extreme sensitivity to variables such as pressure and power. Therefore it is important to carefully control these parameters to achieve satisfactory etching results. This standard cleanroom technique was used to manufacture arrays of microwells in flat Pyrex substrates (Chapters 3 and 4).

2.2.2 Phase Separation Micro-Molding

Phase separation micromolding [3] consists of the replication of a mold (a microstructured master) based on polymer phase separation. In this method, a film of polymer solution dissolved in a solvent is applied on the mold, e.g. by casting. Upon inducing a thermodynamic change either by heating the solution or by immersion in a non-solvent solution that is miscible with the solvent, the solution will phase separate into a polymer-rich part which solidifies and adapts to the shape of the mold. Subsequently, the film is released from the mold. This method offers an easy, fast, and inexpensive microstructuring capability that can accommodate a wide variety of polymers. A drawback is that it can be used for soluble polymers only. We used this method to prepare poly(methyl methacrylate) (PMMA) samples containing microwells (see Chapter 3).

2.2.3 Focused ion beam drilling

The Focused Ion Beam drilling method is used for nanostructuring objects. The method consists of etching material by bombarding a surface with a focused accelerated ion beam. The main components of the FIB system are the ion column, the work chamber, the vacuum and gas systems, and the workstation that provides the user interface [4,5]. The sample to be etched can be mounted in a stage inside the working chamber that is maintained under vacuum in the low 10^{-7} mbar range. An ion (Ga^+) beam is generated from a liquid-metal ion source while applying a strong electrical field that causes the emission of positively charged ions from a liquid gallium cone. By means of electrostatic lenses, the ion beam is accelerated and finally focused (beam currents are typically in the range of 1 pA to 10 nA). These energetic primary ions, while hitting the surface of a solid sample, give energy to the atoms and electrons, sputtering physically a small amount of material, which leaves the surface as either secondary ions or neutral atoms. Hence, etching of the sample occurs. A desired shape can be etched by scanning the focused beam over the sample, as shown schematically in Figure 2.1. The sputtered ions or secondary electrons are used for imaging (similar principle as in scanning electron microscope (SEM)) by collecting them on a biased detector. FIB drilling is a maskless and fast method with flexible working dimensions and imaging ability on nanometer scale.

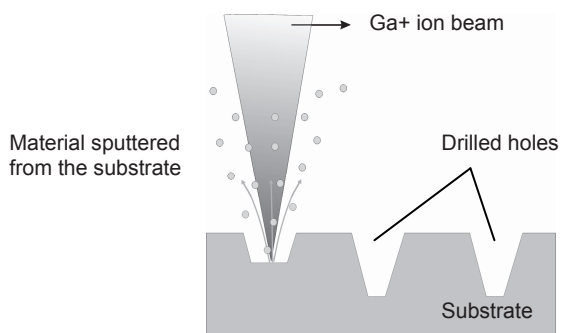


Figure 2.1. Schematic representation of the FIB drilling process.

We use FIB to drill nanoholes in hollow polystyrene beads (see Chapter 6). This method has traditionally been used for etching of conductive materials [4]. In the case of insulators such as polystyrene, charging of the surface could influence the etching process. Also, because of the character of the etching process, redeposition of the etched material might occur. By proper adjustment of sample configuration, nanomachining of polystyrene was possible. The method is limited to small sample dimensions and etching thickness, which however do not influence our system.

We used two FIB systems. The FEI FIB Nova 600 NanoLab [6] is a dual beam FIB/SEM system. Such a system combines ultra-high resolution field emission scanning electron microscopy and precise focused ion beam etch and deposition of the materials. SEM reaches 1 nm spatial resolution and FIB reaches ~ 7 nm at the lowest etching current of 1.5 pA. FEI FIB 200 [7] is a single beam machine and reaches a spatial resolution of ~ 10 nm at the lowest ion current of 1 pA. To etch polystyrene beads, the lowest etching current was used (Chapter 6). For glass beads and flat polystyrene substrates (Appendix C) we used higher etching currents.

2.3 Optical tweezers

Optical tweezers (OT) are single-beam light traps for trapping small particles with refractive index higher than the surrounding [8]. The laser light is brought to a diffraction-limited focal spot through a large numerical aperture microscope objective to form the gradient of the trapping force [9,10] to which optical tweezers owe their trapping capability. OT can trap particles of different sizes in the range smaller than the wavelength of the light (the Rayleigh regime), bigger than the wavelength of light (the Ray optics regime), and the region in between (the Mie regime). The actual trapping force is dependent on both the scattering force and gradient force. The scattering force may be regarded as a consequence of the momentum delivered by the scattered photons. It is defined as the force due to light scattering that is proportional to the incident light intensity; it acts in the

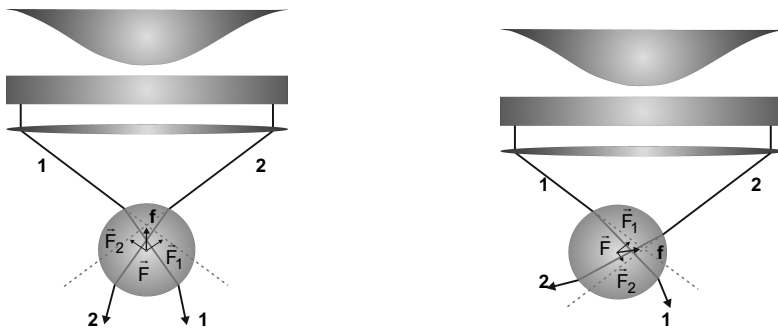


Figure 2.2. Schematic of the forces acting on a bead displaced below (left panel) or to the left (right panel) of the focal point f based on ray optics. \vec{F}_1 and \vec{F}_2 are the forces resulting from ray 1 and 2, respectively, from a Gaussian beam. The net gradient force \vec{F} is pointed toward the focal point f .

direction of propagation of the incident light. The gradient force arises from fluctuating electrical dipoles that are induced when light passes through transparent objects, which consequently experience a time-averaged force in the direction of the field gradient. It is proportional to the spatial gradient in light intensity and acts in the direction of that gradient. A stable trapping occurs when the gradient force overcomes the scattering force. A schematic illustrating the phenomenon based on ray optics is presented in Figure 2.2. Trapping forces can vary from 1 to ~ 100 pN with a sub-piconewton resolution [11]. The force depends on different parameters such as particle size, refractive index, laser power, and numerical aperture (NA) of the objective used for trapping.

OT is used for the manipulation of lipid vesicles with precise position control. To enable trapping by OT the refractive index of lipid vesicles is increased by loading with glucose. An infrared Nd:YVO₄ laser wavelength of 1064 nm (TEM₀₀) was used for trapping and typical powers were 0.2 - 2W (see Chapter 4).

2.4 Voltage-clamp

The dielectric properties of biological membranes enable the study of these membranes and ionic transport occurring through the membranes.

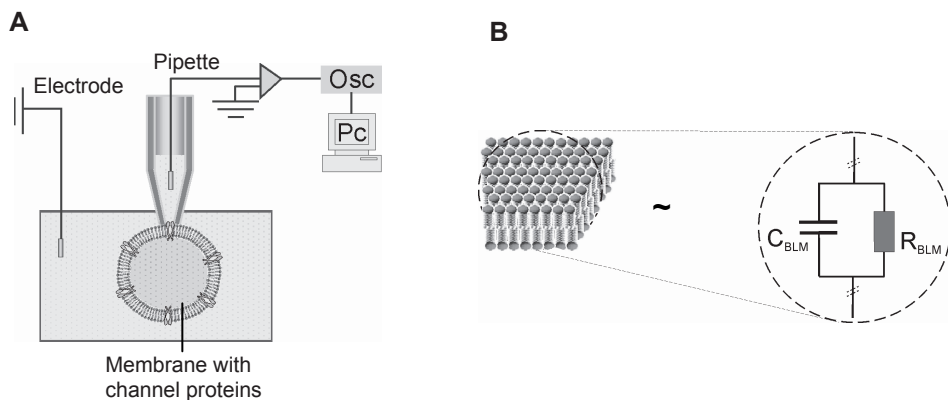


Figure 2.3. (A) Patch-clamping in electrophysiology; (B) Electrical model (right) of a biological membrane composed of packed lipids (left). The membrane is modeled as a gigaohmic resistor, R_{BLM} , in parallel with a weak capacitor ($\sim 1 \mu\text{F}/\text{cm}^2$), C_{BLM} .

In the voltage-clamp electrophysiological method [12], usually two fine electrodes (Ag/AgCl) are positioned on both sides of the membrane. A constant voltage (AC or DC) is applied and the current flow through the membrane is measured.

A widely used technique is patch-clamping. The method allows current measurements in pA range. A simplified schematic of a patch-clamp system is presented in Figure 2.3.A. In such a system, usually a membrane seals a small tip of a glass pipette filled with salt solution while being immersed in the same solution. Electrodes are positioned in the bath solution and in the pipette and connected to an amplifier. The signals are recorded in a computer. In the case when a pulsed input voltage is applied, the ohmic behavior of the system before and after the sealing of the pipette with the membrane supplies information about the membrane resistance. The capacitive transition peaks reflect the information of the capacitance of the membrane. A schematic of the membrane electrical modeling is shown in Figure 2.3.B.

The voltage-clamp method was used to monitor and characterize membrane formation onto a hole and channel protein functionality (see Chapter 3). Typical applied voltages were < 100 mV and sampling rates were ~ 1 kHz.

2.5 Imaging techniques

2.5.1 Epifluorescence microscopy

The basis of fluorescence is the excitation of atoms by absorption of incident light of certain wavelength, resulting in the promotion of electrons from the ground state to higher energy levels. Relaxation of the electrons back to the ground state is accompanied with loss of energy and photon emission, resulting in fluorescence at a longer wavelength. Epifluorescence is the most common fluorescence microscopy technique. The excitation light is focused by an objective lens into the fluorescent sample and the fluorescent light is collected by the same objective. Discrimination between excitation light and fluorescent light is done by means of an emission filter that matches the spectral emission properties of the sample, while a dichroic mirror largely removes the excitation light in the fluorescence path, allowing the passage of the fluorescent light in the detection pathway (see Figure 2.4).

This method enables the illumination of the sample through the objective and a simultaneous imaging of the entire field. An advantage of this method is its simplicity. All fluorescent objects in the field of view will be excited at the same time. A drawback is that a high background signal will be generated from out-of-focus illuminated objects.

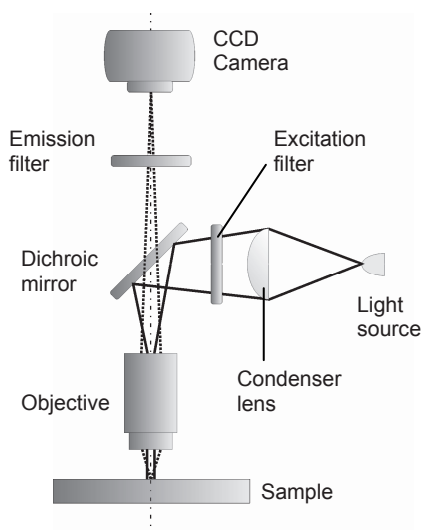


Figure 2.4. Schematic principle of epifluorescence microscopy.

We use this technique to image fluorescently labeled lipid vesicles and membranes. A 488 nm Argon laser was used for excitation of DiO and DiA fluorophores (power < 1 mW). Emission filters were BP 515/30 and BP 615/60. Images were acquired using an integration time of 100-200 ms.

2.5.2 Total internal reflection fluorescence microscopy

When light propagates through the interface of two media of different refractive indices, light is partially reflected at the same angle from the normal with the surface and partially refracted at an angle that satisfies the criteria $n_1 \sin \theta_i = n_2 \sin \theta_t$ (see Figure 2.5.A). The beam is totally reflected when the incident angle θ_i of the beam is $> \arcsin(n_2/n_1)$, a process known as total internal reflection and is accompanied by the appearance of evanescent waves at the interface, with an intensity that decays exponentially with the distance from the interface [13]. The evanescent field decays rapidly (~ 200 nm penetration depth) and has been utilized in fluorescence microscopy (total internal reflection fluorescence (TIRF) microscopy) to selectively excite thin fluorescent objects in the vicinity of the interface [14]. A schematic of the TIRF microscopy principle is presented in Figure 2.5.B. A very thin layer of the sample can be excited by the tail of the evanescent field generated by a beam that is totally reflected off the glass-water interface. The fluorescence intensity is collected from an objective, basically using the same detection pathway as in the case of epifluorescence (see section 2.5.1).

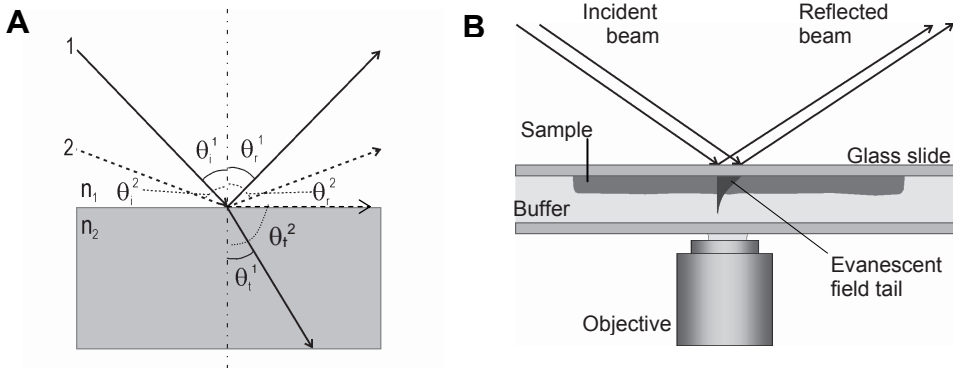


Figure 2.5. (A) Light pathways through media with different optical properties. n_1 and n_2 denote the refractive index of the first and second medium, respectively; $\theta_{r,t}^m$ is the angle of incidence, reflection, and transmission light ray, $m = 1, 2$, respectively. (B) Schematic principle of total internal reflection fluorescence microscopy.

We apply this technique to visualize the dynamics of lipid membrane formation on a support upon vesicle rupture (see Chapter 4). A 488 nm laser (Argon) was used to excite the DiO fluorophore. To prevent dye bleaching, a laser power < 1 mW was used. The illuminated area was $\sim 50 \times 50 \mu\text{m}^2$. Typical integration time for imaging was ~ 100 ms. Emission filters were the same as in epifluorescence (see section 2.5.1).

2.5.3 Confocal laser scanning microscopy

Confocal fluorescence microscopy is a technique that provides three-dimensional optical resolution [15]. It operates in bright field and fluorescence modes. In this technique, the light is focused through an objective lens into a diffraction-limited spot (focal volume) in a fluorescent sample and the fluorescence light, collected by the same objective, comes from the in-focus plane, while out-of-focus plane information is actively suppressed. This is possible by placing a pinhole in front of the detector. The thickness of the excitation volume (or thickness of optical slice) is defined by the pinhole diameter and NA of the objective lens. A schematic of the principle is presented in Figure 2.6. Scanning with the light beam across the sample in a focal plane and imaging all the data points builds up a fluorescence image of that single plane (confocal slice). Collecting confocal slice images for various depths in the sample by an automated adjustment of the objective in the z-direction, results in a map of 2D images in depth (z-stack) that enables

construction of a 3D image which provides detailed information through the sample. The spatial resolution of such a system is \sim half the wavelength of the excitation light.

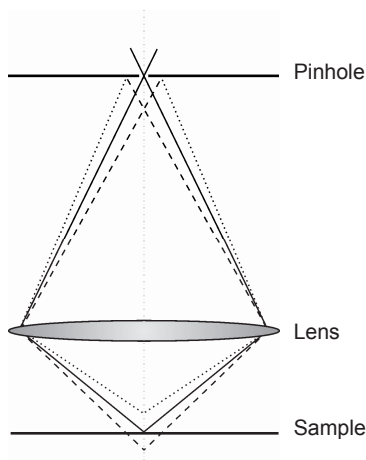


Figure 2.6. Illustration of the confocal fluorescence microscopy principle. Only the fluorescence signal collection is shown.

We used the Zeiss LSM 510 confocal laser scanning microscope (Carl Zeiss, Oberkochen, Germany) to image different objects such as fluorescently labeled vesicles, beads, and membranes on supports. For these experiments we used excitation wavelengths of 488 nm (Argon laser, \sim 3.5 - 5.6 mW) to excite DiO (emission filter BP 500-530), Calcein (BP 500-530), FITC (LP 505), Rhodamine 123 (LP 505) and DiA (LP 560) and 543 nm (HeNe laser \sim 1.25 - 2 mW) to excite Alexa (LP 560). A C-Apochromat 63 \times /1.2 water immersion objective was used. Typical scanning time to acquire images was $<$ 3 sec, and the thickness of confocal (optical) slices was $<$ 1 μ m. For this scanning time dye bleaching was not critical. The multichannel recording capability of the system allowed us to excite multiple fluorophores at the same time (DiA and Calcein). The system facilitates automated acquisition of time-series images. This allowed us to monitor dynamics of several processes such as vesicle rupture and diffusion of fluorophores in microwells and spherical hybrid vehicles.

2.5.4 Atomic force microscopy

Atomic force microscopy (AFM) is an imaging technique that offers a high spatial resolution, yielding detailed information of various objects at nanometer scale [16-19]. In this technique, a sharp conducting tip, located on the free end of a soft spring (cantilever), scans the sample surface [20]. The cantilever is deflected due to the forces between the tip and the sample surface. The nature of such interactions includes Van der Waals forces and electrostatic interactions.

Deflections of the cantilever from point to point are detected, resulting in a map of surface topography. This technique offers an atomic resolution.

A schematic of an AFM microscope is presented in Figure 2.7. Two modes of scanning are possible: contact mode and non-contact mode. In contact mode, a constant force between the tip and sample is adjusted by feedback controlling the distance between the tip and the sample while the tip constantly probes the sample surface. Such a mode shows drawbacks when working with sensitive samples where the lateral forces exerted by continuous scanning of the tip on the surface cause defects or damages of the sample.

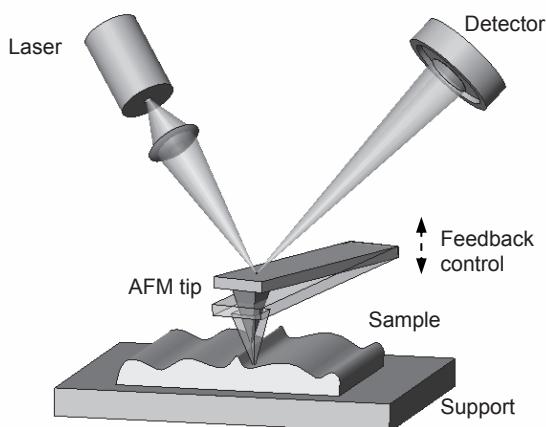


Figure 2.7. Schematic representation of an AFM microscope.

In this aspect, non-contact mode such as tapping mode shows an improvement. In this case, the cantilever is oscillated near its resonance frequency and the tip gently touches the surface. Changes of the oscillation amplitude due to the tip interaction with the sample provide topographic information for the sample.

A stand-alone AFM developed in our group [21] was used to characterize the lipid membranes immersed in aqueous solution (see Chapter 3). Experiments were performed in tapping mode using a silicon nitride cantilever and a frequency of ~ 33 - 36 kHz.

References

- [1] H.F. Winters, Role of chemisorption in plasma etching, *Journal of Applied Physics*, 1978, **49**, 5165-5170.
- [2] H. Jansen, H. Gardeniers, M. de Boer, M. Elwenspoek, and J. Fluitman, A survey on the reactive ion etching of silicon in microtechnology, *J. Micromech. Microeng.*, 1996, **6**, 14-28.

- [3] L. Vogelaar, J.N. Barsema, C.J.M. van Rijn, W. Nijdam, and M. Wessling, Phase Separation Micromolding – P Σ μM, *Advanced Materials*, 2003, **15**, 1385-1389.
- [4] S. Reyntjens and R. Puers, A review of focused ion beam applications in microsystem technology, *Journal of Micromechanics and Microengineering*, 2001, **11**, 287-300.
- [5] J. Orloff, M. Utlaut, and L. Swanson, *High Resolution Focused Ion Beams: FIB and its Applications*, Kluwer Academic / Plenum Publishers, New York, USA, ISBN 0-306-47350-X, 2003.
- [6] FEI FIB Nova 600 NanoLab, FEI, Eindhoven, The Netherlands, 2006, http://www.fei.com/Portals/_default/PDFs/content/2006_06_Nova600NanoLab_pb.pdf
- [7] FEI FIB 200, MASER Engineering B.V., Enschede, The Netherlands, 2006, <http://www.maser.nl/equipmentlest.pdf>.
- [8] A. Ashkin, J.M. Dziedzic, J.E. Bjorkholm, and S. Chu, Observation of a single-beam gradient force optical trap for dielectric particles, *Opt. Lett.*, 1986, **11**, 288-290.
- [9] P.A. Maia Neto and H.M. Nussenzveig, Theory of optical tweezers, *Europhysics Letters*, 2000, **50**, 702-708.
- [10] K. Svoboda and S.M. Block, Biological Applications of Optical Forces, *Annual Review of Biophysical and Biomolecular Structure*, 1994, **23**, 247-285.
- [11] E.A. Abbondanzieri, W.J. Greenleaf, J.W. Shaevitz, R. Landick, and S.M. Block, Direct observation of base-pair stepping by RNA polymerase, *Nature*, 2005, **438**, 460-465.
- [12] R. Latorre (Ed.), *Ionic Channels in Cells and Model Systems*, Plenum Press, New York, ISBN 0-306-42194-1, 1986.
- [13] E. Hecht, *Optics*, Addison-Wesley, Reading, Mass, 1998.
- [14] P.B. Conibear and C.R. Bagshaw, A comparison of optical geometries for combined flash photolysis and total internal reflections fluorescence microscopy, *Journal of Microscopy*, 2000, **200**, 218-229.
- [15] T. Wilson (Ed.), *Confocal microscopy*, Academic Press Limited, St Edmundsbury Press Ltd, Suffolk, UK, ISBN 0-12-757270-8, 1990.
- [16] R.P. Goncalves and S. Scheuring, Manipulating and imaging individual membrane proteins by AFM, *Surface and Interface Analysis*, 2006, **38**, 1413-1418.
- [17] C. Rivetti, M. Guthold, and C. Bustamente, Scanning force microscopy of DNA deposited onto mica: Equilibration versus kinetic trapping studied by statistical polymer chain analysis, *J. Molec. Biol.*, 1996, **264**, 919-932.
- [18] T. Hughes, B. Strongin, F.P. Gao, V. Vijayvergiya, D.D. Busath, and R.C. Davis, AFM Visualization of Mobile Influenza A M2 Molecules in Planar Bilayers, *Biophysical Journal*, 2004, **87**, 311-322.
- [19] H. Arakawa, K. Umemura, and A. Ikai, Protein images obtained by STM, AFM and TEM, *Nature*, 1992, **358**, 171-173.
- [20] G. Binnig, C.F. Quate, C. Gerber, Atomic force microscope, *Physical Review Letters*, 1986, **56**, 930-933.
- [21] K.O. van der Werf, C.A.J. Putman, B.G. de Grooth, F.B. Segerink, E.H. Schipper, N.F. van Hulst, and J. Greve, Compact stand-alone atomic force microscope, *Rev. Sci. Instr.*, 1993, **64**, 2892-2897.

CHAPTER THREE

FABRICATION OF MEMBRANE PLATFORMS

Different approaches to depositing an artificial bilayer lipid membrane onto a micrometer-sized hole in a flat substrate are explored. A procedure for the formation of membrane patches based on vesicle collapse on charged surfaces is devised. The resulting membrane structures are characterized using AFM and electrophysiological techniques.

3.1 Introduction

We investigated essential features of the biological construct that was used for development of a stable spherical hybrid vehicle. We explored methods for membrane formation and evaluated the stability of the formed membrane. Existing methods for bilayer lipid membrane (BiLM) formation are 'brushing' [1] and vesicle collapse [2]. We explored these techniques to determine which one would be useful for our application. We used a planar substrate as an easy platform for membrane formation and characterization. So far, flat substrates containing holes have been extensively used as supports for biological or synthetic BiLMs to study membrane properties [3], conformational changes of different biomolecules embedded in the membrane [4,5], or as nanosensors to study e.g. DNA and RNA structures [6-8]. Membranes deposited on such supports are extremely delicate and susceptible to breakage, requiring vibration isolation, low acoustic noise environment, and special solution handling procedures. For our application, it is important to have a stable membrane. Therefore we needed to find alternative ways to achieve a stable membrane. To do so, we designed a system in which the hole dimensions were scaled down to one micrometer, much smaller than those in conventional approaches. The reduction of the free standing membrane area positively influences the membrane stability [9-12], and is the rationale for development of membrane supports with small diameter, e.g. below 40 micrometer as reported in Ref. 12.

We first realized a model of a hybrid flat platform having a stable membrane covering a hole where functional biomolecules were incorporated. We designed a new planar system based on arrays of microwells and developed a procedure to deposit a synthetic bilayer lipid membrane onto microwells in the flat substrate. The procedure generates a sealed microwell comprising a defined volume that allows environmental changes only from one side: from the well exterior. We used optical monitoring to provide both qualitative and quantitative information on membrane properties like stability and sealing properties.

3.2 Requirements

Our goal was to develop a hybrid flat platform containing arrays of compartments of micrometer size, sealed with an artificial bilayer lipid membrane that is stable in time and contains functional biomolecules. The criteria to achieve this goal are defined as follows:

- High temporal stability of the deposited lipid membrane is essential, making the system more robust. Conventional black lipid membranes are very unstable, lasting a few hours and rarely exceeding one day [9]. The ideal platform would be stable for a longer period, that is, at least for a few days.
- The membrane should provide a good seal of the hole. The process of molecular transport should only take place specifically through the membrane by means of incorporated functional biomolecules.
- Membranes should be minimally sensitive towards detrimental environmental factors like temperature. These physical properties of a membrane are defined by the lipid composition. Different lipids have different transition temperatures. Therefore, the choice of the lipid molecules forming the membrane is important.
- The material of the flat substrate should be optically transparent to facilitate the monitoring of transport processes occurring through the membrane.
- The substrates should be biocompatible, and possibly, reusable.
- The size of the access hole of the well should be in the micrometer range, e.g. $\sim 1 \mu\text{m}$, in order to increase the stability [9,12] of the membrane by making it less sensitive to mechanical disturbance, vibrations, and surface tension. On the other hand, for optical measurements, the hole size should be larger than the optical resolution, that is, larger than the diffraction limit ($\sim \lambda/2$, with the wavelength $\lambda \sim 500 \text{ nm}$).
- Deep holes are required, with a depth higher than the axial resolution of the optical microscope ($\sim 1 \mu\text{m}$) and having a high hole depth / hole diameter aspect ratio. To optically address the interior of the well independently from the bulk solution, e.g. by measuring the fluorescence, the depth should be larger than the axial resolution of the microscope. Possible bending of the membranes on the holes could yield an ambiguous result, a problem which could be overcome by the high aspect ratio.

Based on this analysis, we settled on the preliminary design of our flat hybrid platform, consisting of a flat substrate containing microwells. The substrate material was chosen to be Pyrex or poly(methyl methacrylate) (PMMA). The diameter of the microwell was selected $\sim 1 - 3 \mu\text{m}$ and the well depth $> 3 \mu\text{m}$. The membrane composition was based on phosphatidylcholine lipids. Further details about lipid composition will be presented below and in Chapter 4. Sealing may depend on the method and will be further discussed below.

3.3 Substrate fabrication

Optically transparent substrates containing arrays of microwells were prepared using Pyrex and PMMA.

Pyrex shows good stability and allows multiple use. The samples were prepared using cleanroom technology. Arrays of microwells were prepared in Pyrex substrates ($\sim 400 \mu\text{m}$ thick) using a micro patterned photo resist mask and Reactive Ion Etching (RIE) for ~ 1 hour (see steps 1-5 in Appendix A). Hole diameter was $\sim 1.1 \mu\text{m}$ and hole-to-hole center spacing $4 \mu\text{m}$. For the substrates used in this chapter, it was difficult to obtain wells with a depth $> 400 \text{ nm}$. The parameters were further optimized as discussed in Chapter 4.

The results with Pyrex substrates were hampered by insufficient well depth and large substrate thickness ($400 \mu\text{m}$), which does not allow the use of high NA objectives that are required to address the well interior independently from the exterior. We thus chose PMMA for the ease of fabrication and flexibility in preparation. PMMA substrates ($< 100 \mu\text{m}$ thick) were prepared using Phase Separation Micro-molding method, as described elsewhere [13]. They were supported on round glass coverslips. First PMMA was dissolved at 16-23 wt-% in acetic acid. Next, a sandwich made of glass substrate-polymer film-mold was formed by casting. The glass-supported polymer sample was released from the mold using liquid-induced phase separation in water. The hole diameter was ~ 6.5 to $7 \mu\text{m}$, depth $\sim 7 \mu\text{m}$, and hole-to-hole center spacing $10 \mu\text{m}$ which were limited by the parameters of the available mold.

3.4 Lipid composition

Cell membranes are composed of lipids, which are amphiphilic molecules, packed in two layers where the hydrophobic part forms the core of the membrane. Lipid composition is an important parameter that influences the membrane stability and sealing, and depends on the method we are using for membrane deposition. We investigated two methods for membrane deposition: brushing, which is an easy and well developed method, yielding a “black lipid membrane” (BLM), and vesicle collapse, which has an advantage over the brushing method because the biomolecules can be incorporated prior to membrane deposition, resulting in a bilayer lipid membrane. These methods will be presented in sections 3.5 and 3.6, respectively.

Black lipid membranes. Phospholipids are easy to handle and to synthesize [1]. The composition of the lipids used here is based on previous work on planar BLM that showed satisfactory results with a lipid mixture dissolved in a volatile solution [14]. The composition we used consisted of phosphatidylcholine, combined with cholesterol and phosphatidic acid. Planar membranes based on phosphatidylcholine such as 1,2-Diphytanoyl-sn-Glycero-3-Phosphocholine (DPhPC, a synthetic saturated phospholipid) have been extensively used as model membranes and in nanosensors [6,8,15-18]. Such membranes show

higher stability against mechanical disturbances, temperature fluctuations, and external electrical field change, as compared to other types of lipid membranes [1,19,20]. Addition of cholesterol and phosphatidic acid further increases the stability [15] and the rate of membrane thinning [14]. Typically used lipid concentrations vary from 1 to 10 percent (weight in n-Decane) [21,22].

We used a stock solution of DPhPC (mixed with cholesterol and phosphatidic acid in a ratio respectively of 1:0.26:0.02 by MW) of a concentration of 1 and 4 mg/ml in n-Decane.

Vesicle-based membranes. Phosphatidylcholine is one of the basic components in a cell membrane [1,23]. It has been extensively used to synthesize quasi-stable free-standing planar artificial membranes [6,8]. Addition of a small percentage of cholesterol increases the fluidity and stability of the membrane. Cholesterol acts as a 'spacer' and reduces the attractive forces between the hydrocarbon chains [15]. However, addition of high percentage of cholesterol, e.g. above 20%, affects and restricts the biofunctionality in the membrane and its stability [1,15,24]. For the vesicle collapse method we are using, it is important to use lipids that have a net charge to facilitate the electrostatic interaction of vesicles with the surface. Natural membranes always contain a certain amount of negatively charged lipids, which are preferred not only because they possess a net charge enabling reasonable electrostatic interaction [24], but also because protein incorporation is favored in such membranes [15]. However, membranes formed from a high percentage of negatively charged lipids tend to be unstable [1]. We used zwitterionic lipids (DPhPC) combined with charged lipids. Vesicles based on different combinations of lipids, with or without a small percentage of cholesterol, were investigated for defining a composition that allowed the controlled deposition of vesicles, a sufficiently high resistance and reliable microwell seal, and a long temporal stability of the free-standing membrane on the hole. Charged lipids, containing long hydrocarbon chains comparable with the chain length of phospholipids, were chosen and will be discussed further in section 3.6.

3.5 Brushing method for Black Lipid Membrane formation

3.5.1 Theory

Principle. The brushing method consists of a spontaneous formation of the BiLM onto a hole in a support, and follows from the thinning of the deposited mass of lipids under favorable conditions [1,3]. Usually in this method, the hole ($> 30 \mu\text{m}$) is present in a vertical support separating two aqueous compartments. A small droplet of lipids dissolved in an organic solvent such as n-Decane is painted onto

the hole with a fine 'brush' or plastic tip. Three distinguishable stages during bilayer formation may be observed, schematically presented in Figure 3.1. In the first stage, the thick lipid membrane initially formed may consist of a bulk hydrophobic phase of membrane-forming solution with an adsorbed monolayer of lipid molecules at each oil-water interface. In the second stage, while the membrane thins, the attractive forces between the adsorbed lipid monolayers are small and the driving force for membrane thinning is the pressure difference due to the presence of the Plateau-Gibbs border (i.e. the margin of bulk phase lipid in which the membrane terminates). At this border, the concave interfaces create a pressure which is less than that in the interior of the thick planar membrane. Thus, the border exerts a strong negative pressure upon the interior of the thick portion of the membrane, causing bulk flow of the interior phase and rapid reduction in the membrane thickness. From that moment, the third stage is the double layer membrane formation that has been suggested to be a 'zipper-like' mechanism. Optical observation of such a membrane results either in a transparent or black area confined with a golden-color border [25,26]. The amount of deposited lipids is larger than the amount of lipid resting in the hole and the border. The additional lipids leave these regions in different ways: in the form of micelles or free bulk lipids, a process favored by stirring and refreshment of the bulk solution.

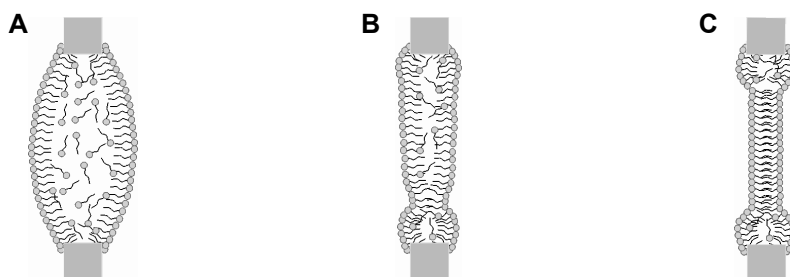


Figure 3.1. Three stages present during the formation of a painted bilayer on a substrate. (A) A lipid-organic solvent droplet painted on the aperture in the support; (B) Thinning of the droplet and starting of membrane formation; (C) Bilayer black membrane completely formed on the hole surrounded by the thick Plateau-Gibbs border.

Brushing the microwells. Pre-treating the region of the hole by drying lipids dissolved in a volatile solution on this region speeds up bilayer membrane formation by brushing. However, given the small well dimensions we are using it is very difficult to selectively coat only the border of the hole. Therefore, we did not apply this method. We applied the brushing method by controlled delivery of

small droplets of phospholipids-Decane onto the holes, as will be shown in the following section.

3.5.2 Materials and methods

Materials. Zwitterionic Phospholipids (DPhPC, 1,2-Diphytanoyl-sn-Glycero-3-Phosphocholine) and Phosphatidic acid (PA, 1-Stearoyl-2-Oleoyl-sn-Glycero-3-Phosphate, monosodium Salt) were obtained from Avanti Polar Lipids (Alabaster, USA). Cholesterol (3β -Hydroxy-5-cholestene, $C_{27}H_{46}O$) and DiO (3,3'-Dioctadecyloxacarbocyanine perchlorate, $C_{53}H_{85}ClN_2O_6$) were purchased from Sigma (Zwijndrecht, The Netherlands). N-Decane ($C_{10}H_{22}$) was a product of Merck (Darmsstadt, Germany). Borosilicate glass capillaries of 0.94 and 1.2 mm inner and outer diameter, respectively (GC120TF-15) were obtained from Harvard Apparatus (Holliston, MA, USA). Poly(methyl methacrylate) (PMMA) was purchased from Polyscience (Warrington, PA, USA). Round glass coverslips (thickness of 150 μ m and diameter of 30 mm) were obtained from Menzel-Gläser (Braunschweig, Germany).

Lipid composition. We used a stock solution of DPhPC (mixed with cholesterol and PA in a ratio respectively of 1:0.26:0.02 by MW) dissolved in n-Decane at a concentration of 1 and 4 mg/ml.

Fabrication of glass pipettes. Pipettes based on borosilicate glass capillaries were produced using a pipette puller (Sutter P-87 micropipette puller, Novato, CA, USA). The typical inner diameter of the pipettes was < 1 μ m and taper length ~ 4 mm as revealed from SEM and white light imaging. Parameter settings of the puller used to fabricate such pipettes are presented in Table 3.1.

Table 3.1. Parameter settings of the puller used to fabricate submicron glass pipettes.

Step nr.	Heat	Pull	Velocity	Time	Pressure
1	320	0	20	200	400
2	320	0	20	200	400
3	320	150	30	100	400

Prior to pulling, the capillaries were cleaned by incubating them in 100% ethanol, removing most of ethanol and allowing the remaining ethanol to dry for ~ 2 days in a clean environment. Pipettes were pulled in a multi-step process and were reproducible as observed for more than 30 samples. Heating parameter was

adjusted slightly above the ramp (melting) temperature. Scanning electron imaging of fabricated pipettes showed a smooth tip edge (Figure 3.2).



Figure 3.2. Scanning electron imaging of borosilicate glass pipettes produced with a pipette puller (A). (B) Higher magnification image of tip in (A). Scale bars are 500 μm and 500 nm, respectively.

Lipid deposition. Controlled deposition of lipid-Decane solution onto the holes in the flat substrates was done by using a microinjector (Eppendorf Microinjector 5242, VWR International B.V., Amsterdam, The Netherlands). To deposit small lipid droplets, pipettes having a tip diameter less than 1 μm (inner diameter \sim 0.7 μm) were used. The pipette was positioned on a XYZ translation stage and was located close to the holes. Droplets with a diameter of $>$ 10 μm were deposited on the substrates using injecting pressures of $>$ 615 hPa, holding pressure of about 40-70 hPa, and an injection time \sim 0.1 seconds. The process was followed using white light microscopy.

3.5.3 Results and discussion

Membrane formation

Painted membranes on Pyrex holes. Figure 3.3 depicts membrane formation by painting lipid-Decane droplets (1 mg/ml) on sub-micron holes on Pyrex substrates using the microinjector. From the first 3 images (A, B, and C), thinning of the droplet was visualized until it was not recognizable anymore in white light. Fluorophore (DiO) was added to the solution to label the lipid membrane. Fluorescence microscopy was used to visualize membrane formation. An increase of the fluorescence intensity in the regions of the holes (Figure 3.3.D) was observed, indicating the membrane formation on these holes. A drawback is the long time interval (days) required for droplet thinning to form a membrane (see section 3.5.1). In addition, the small well depth makes it difficult to distinguish

between the membrane covering the hole and the well interior. To better monitor the membrane formation, a PMMA substrate with deeper wells was prepared.

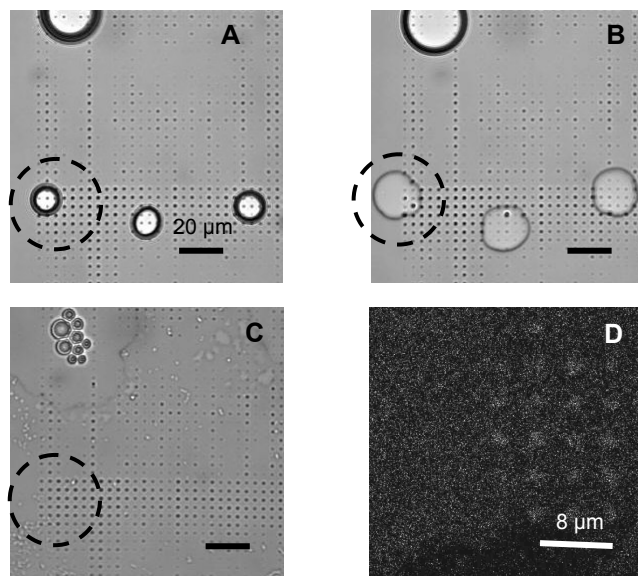


Figure 3.3. CLSM images of a painted membrane on sub-micron holes in a Pyrex substrate. Region of interest is indicated with a dashed-ring. (A) White light image of a pattern of lipid-Decane (concentration of 1 mg/ml) droplets in water solution deposited with a glass pipette (inner diameter of 0.5 μm) using the microinjector. Injection pressure was 615 hPa, holding pressure 55 hPa, and automated injection time 0.1 seconds. White light image of the thinned droplets after 2 days (B) and \sim 1 week (C). (D) Fluorescence image of DiO-labeled membranes organized on the holes. This is a zoom in of the region of interest in (C).

Membranes painted on PMMA substrates. Figure 3.4 presents a pattern of lipid-Decane droplets deposited on the PMMA holes. The sample was maintained in aqueous solution. During thinning of the droplets the sample was incubated at 4 $^{\circ}\text{C}$ and the bulk solution was refreshed every day. Furthermore, the sample was kept tilted to accelerate the primary bulk thinning of the lipid droplets due to gravity. After the droplets became thinner (transparent regions appear when observing with white light), the dye that stains the lipid membrane was added to the bulk solution (200 μl of 10 $\mu\text{g/ml}$ DiO in MeOH stock solution). Membrane formation onto the holes was further visualized using CLSM.

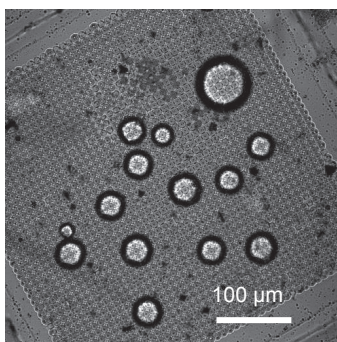


Figure 3.4. CLSM image of a pattern of lipid-Decane (concentration of 4 mg/ml) droplets in water solution deposited with a glass pipette (inner diameter of 0.6 μm) on the PMMA substrate using the microinjector. Injection and holding pressure were 667 and 47 hPa, respectively, and automated injection time was 0.2 seconds.

Figure 3.5 shows a confocal slice inside the well and on the surface, as well as the X-Y cross section of the fluorescence intensity in different depths of the lipid membrane covering the PMMA hole. The thin membrane layer covering the hole (Figure 3.5.B, indicated with a dashed ring) can be clearly recognized, while no membrane exists inside the hole (Figure 3.5.A). The time required for this droplet to thin and form the membrane was approximately 1 week, which is a long time scale compared with the results reported in literature for brushing methods.

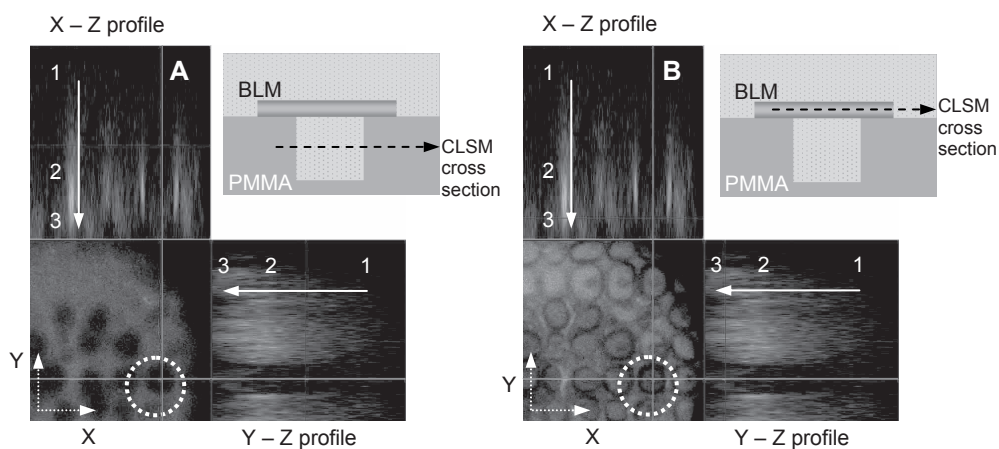


Figure 3.5. CLSM X-Y cross section in different depths of a fluorescently-labeled lipid membrane covering a hole in the PMMA substrate. Membrane labeled with DiO (excitation and emission wavelengths of 488 nm and 505 nm, respectively). Solid arrows indicate layers from glass (1) towards PMMA (2) and bulk solution (3). A cross (within the dashed-ring) points out the hole of interest. Depth images are captured (A) inside the well (PMMA) and (B) on the well surface, as indicated schematically by dashed arrows.

3.6 Lipid Vesicles

The brushing method required long times for membrane formation, and was judged not effective enough to proceed with biomolecules. Therefore, we followed an alternative way to form a bilayer lipid membrane.

When lipids are in contact with water, several aggregation forms are possible. Of these forms, the lipid bilayer is a stable form where the lipid tails are grouped together and the lipid heads are in contact with water. Lipid vesicles are small liquid droplets enclosed by one or more lipid bilayers, accordingly called unilamellar and multilamellar vesicles. When being in contact with a surface, unilamellar vesicles can rupture, forming a BiLM. It is believed that a strong adsorption of the vesicle on the surface occurs first and later the interaction of the vesicle with the surface causes a tension in the vesicle membrane, followed by vesicle deformation and, subsequently, its rupture and spreading of the BiLM on the surface [2,35,36]. The process can be influenced by different factors such as vesicle size, surface properties and chemistry, temperature and osmotic pressure [2].

We used vesicle rupture to deposit a membrane on a flat substrate as depicted schematically in Figure 3.6. When a vesicle with a diameter larger than the diameter of the hole is deposited onto the hole, rupture of the vesicle can occur, resulting in the formation of a membrane patch.

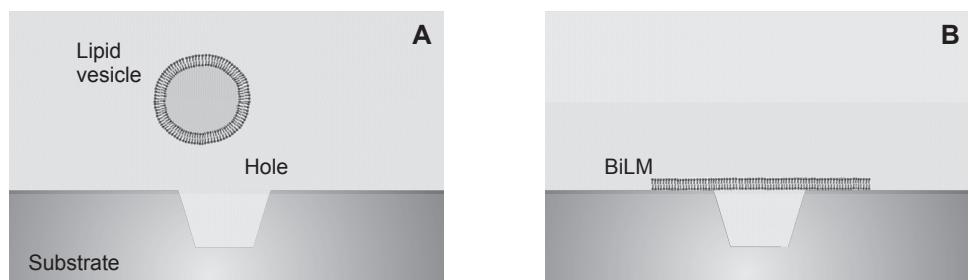


Figure 3.6. Vesicle collapse onto a hole. (A) A flat substrate containing a microwell and incubated in buffer. Vesicle is approaching the microwell. (B) The vesicle collapse on the region of the hole, resulting in a membrane patch that spans and seals the hole.

In this section, we describe the production of giant unilamellar vesicles (GUVs) of different lipid compositions and investigate their collapse on supports with different surface properties. We characterized the membrane patches with respect to the thickness and quality of the sealing of a hole in a support using

different methods such as fluorescence microscopy to monitor the membrane formation, AFM to give topological information, and electrophysiology to provide information about hole sealing and membrane thickness. The addition of glucose inside the vesicles is used as required for optical tweezers experiments that will be discussed in Chapter 4.

3.6.1 Materials and methods

Materials. Zwitterionic Phospholipids (DPhPC, 1,2-Diphytanoyl-sn-Glycero-3-Phosphocholine), Phosphatidic acid (PA, 1-Stearoyl-2-Oleoyl-sn-Glycero-3-Phosphate, monosodium Salt), and POPG (PG, 1-Palmitoyl-2-Oleoyl-sn-Glycero-3-[Phospho-rac-(1-glycerol)]), Sodium salt) were purchased from Avanti Polar Lipids (Alabaster, USA). Asolectin (Asolectin from soybean), Cholesterol (3β -Hydroxy-5-cholestene, $C_{27}H_{46}O$), DiO (3,3'-Diocetadecyloxycarbocyanine perchlorate, $C_{53}H_{85}ClN_2O_6$), and PLL (poly-L-lysine hydrobromide) were obtained from Sigma (Zwijndrecht, The Netherlands). PD10 desalting columns were purchased from Amersham Biosciences (Roosendaal, The Netherlands). Glucose (D(+)-Glucose) and chloroform were products of Merck (Darmstadt, Germany). Microscope slides and coverslips (thickness of 170 μ m) were obtained from Menzel-Gläser (Braunschweig, Germany). Parafilm (Parafilm M) was purchased from Alcan Packaging (Zutphen, The Netherlands).

Vesicle preparation. Giant vesicles were prepared using the freeze-thaw method. Lipids, e.g. 1,2-Diphytanoyl-sn-Glycero-3-Phosphocholine (DPhPC), phosphatidic acid (PA), and cholesterol of ratio 70:25:5 wt.-%, were mixed with chloroform in a round flask. Using a rotary evaporator apparatus, a uniform dried lipid film was prepared under vacuum conditions. 25 ml of 400 mM glucose solution in de-ionized water was added in the flask and left for less than 30 minutes to swell the film and form the vesicles. After swelling, a thermo-shock was given to the vesicle solution to produce unilamellar vesicles. The round flask was placed shortly once in liquid nitrogen and then in water at a temperature ~ 35 $^{\circ}$ C, repeating this cycle 5-8 times. Different combinations of lipid composition that were used to produce vesicles are listed in Table 3.2.

Swelling the vesicles yielded a multi-disperse vesicle size distribution. Large vesicles were collected using a PD10 desalting column by flowing buffer to filter the small vesicles and the glucose from the bulk solution, yielding vesicles loaded with 400 mM glucose solution. Next, the vesicles were labeled with DiO by adding 30 μ l of DiO stock solution (DiO concentration of 10 μ g/ml in MeOH) to 1 ml vesicle solution.

Table 3.2. Lipid compositions used for vesicle preparation.

Lipid Composition	Ratio (wt.-%)
DPhPC	100
DPhPC:cholesterol	95:5
DPhPC:PA:cholesterol	70:25:5
DPhPC:POPG:cholesterol	70:25:5
Asolectin:cholesterol	95:5
Asolectin:POPG:cholesterol	70:25:5
DPhPC:cholesterol in 0.017mM SDS	95:5

3.6.2 Results

Membrane formation

Vesicle collapse on bare flat glass, polystyrene, and PMMA surfaces.

Free collapse of the glucose loaded vesicles (DPhPC-cholesterol composition) on supports made of different materials was observed by imaging the membrane patches using epifluorescence or CLSM microscopy. To achieve the collapse, the vesicles, immersed in buffer, were introduced for 4 hours at room temperature on these supports positioned at the bottom of a cuvette. We found that free collapse of the vesicles takes place on glass and PMMA surfaces while no collapse occurs on hydrophobic polystyrene surfaces.

The rate of vesicle collapse on the glass substrate was observed for different lipid compositions. The rate is defined as the percentage of the surface covered with membranes due to vesicle collapse for a defined time interval. In Table 3.3, the rate of collapse of the lipid vesicles on bare glass surface is presented. These tests indicated that the rate of collapse of the vesicles increases upon adding charged lipids such as Asolectin, POPG, and PA. A reason for this observation might be that the transition temperature decreases when mixing DPhPC with other charged lipids of lower transition temperature than DPhPC, resulting in weaker membrane lipid cohesion, and hence higher collapse rates. The addition of charged lipids could cause an additional interaction force between the vesicles and the glass surface which could cause faster vesicle collapse.

Vesicle collapse on chemically modified flat surfaces.

Free collapse of the vesicles (DPhPC-cholesterol) was observed for the abovementioned flat surfaces, chemically modified with poly-L-lysine (PLL). PLL is a polymer that has a net positive charge at neutral pH and binds electrostatically to the slightly negatively charged glass surface, resulting in a

positively charged coating of the glass surface. Free collapse of vesicles on the surface is presented in Figure 3.7. The process was monitored using CLSM by focusing on the surface and acquiring a time series of images. The rate of collapse of glucose loaded vesicles on PLL modified glass substrate was monitored for different lipid compositions. A qualitative estimate of the collapse rate is indicated in Table 3.3.

Table 3.3. Free collapse of vesicles on a bare and PLL modified glass surface estimated qualitatively for vesicles with different lipid compositions. ---, --, -, +, ++, and +++ indicate a extremely low, very low, low, average, high, and very high collapse rate, respectively, expressing the percentage of imaged area covered with membrane patches.

Vesicle composition	Collapsing of vesicles on a glass surface	
	Bare	PLL-modified
DPhPC	--	-
DPhPC:cholesterol	---	-
DPhPC:cholesterol:PA	-	+
DPhPC:cholesterol:POPG	-	+
DPhPC:cholesterol in SDS	-	++
Asolectin:cholesterol	++	+++
Asolectin:cholesterol:POPG	++	+++

We observed an improvement of the vesicle collapse on the PLL modified glass surface compared to bare glass surfaces. Patches were observed more often and the time required for vesicle collapse was shorter. In the case of PMMA, less improvement was observed, while for polystyrene, patches were only rarely observed.

The collapsing of zwitterionic phospholipid-containing vesicles increased by coating the substrate with PLL. The rate of collapse is significantly higher for negatively charged vesicles (Asolectin) compared to neutral vesicles. The increase was smaller for POPG and PA.

The observed higher collapse rates for PLL surfaces are caused by increased surface charge – lipid charge interaction that takes place when a vesicle is in the Van der Waals interaction range (~ nm). Once a contact between a vesicle and the surface is established, the interaction of the neighboring lipids with the surface is facilitated, increasing the vesicle contact area on the surface, resulting ultimately in vesicle rupture.

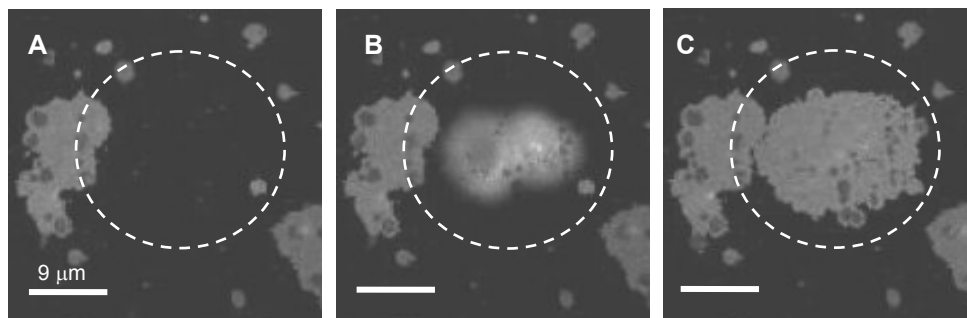


Figure 3.7. Free collapse of vesicles on a PLL modified glass support. CLSM fluorescence image of the glass surface (A) prior to vesicle collapse; (B) vesicle approaching the surface; (C) after collapse of the vesicle in (B), forming a membrane patch. Region of interest is enclosed by the dashed circle.

3.6.3 Membrane characterization

We showed membrane formation on supports based on free vesicle collapse. When a unilamellar vesicle comes in contact with a surface, two situations might be possible: either the vesicle deforms forming 2 bilayers or it collapses forming a single bilayer on the surface as depicted schematically in Figure 3.8. In order to distinguish between these two situations, the formed membranes were characterized with respect to the membrane thickness, homogeneity, and number of bilayers.

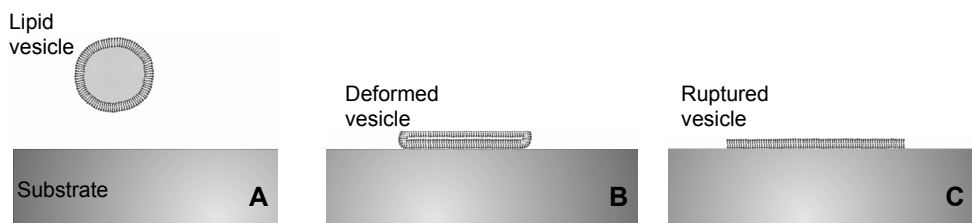


Figure 3.8. Schematics of membrane formation on flat supports due to vesicle collapse. (A) A vesicle approaching the surface of the substrate that is immersed in buffer. (B) Vesicle deformation on the surface forming stacked bilayers. (C) Vesicle collapse on the surface, forming a single bilayer membrane.

3.6.3.1 Atomic Force Microscopy

We used AFM to characterize the deposited artificial lipid membrane patches with respect to the number of bilayers, thickness, and structure regularity. A dedicated AFM set-up [27] was used to carry out this work. Measurements were performed in aqueous medium using AFM tapping mode. A flat and round glass coverslip (thickness of 170 μm and diameter of 30 mm) was cleaned with 65% HNO_3 and rinsed with de-ionized water. The coverslip was supported on a cuvette where de-ionized water was added prior to vesicle addition. Vesicles, composed of phosphatidylcholine (DPhPC) and cholesterol of ratio 95:5 wt.-% and loaded with

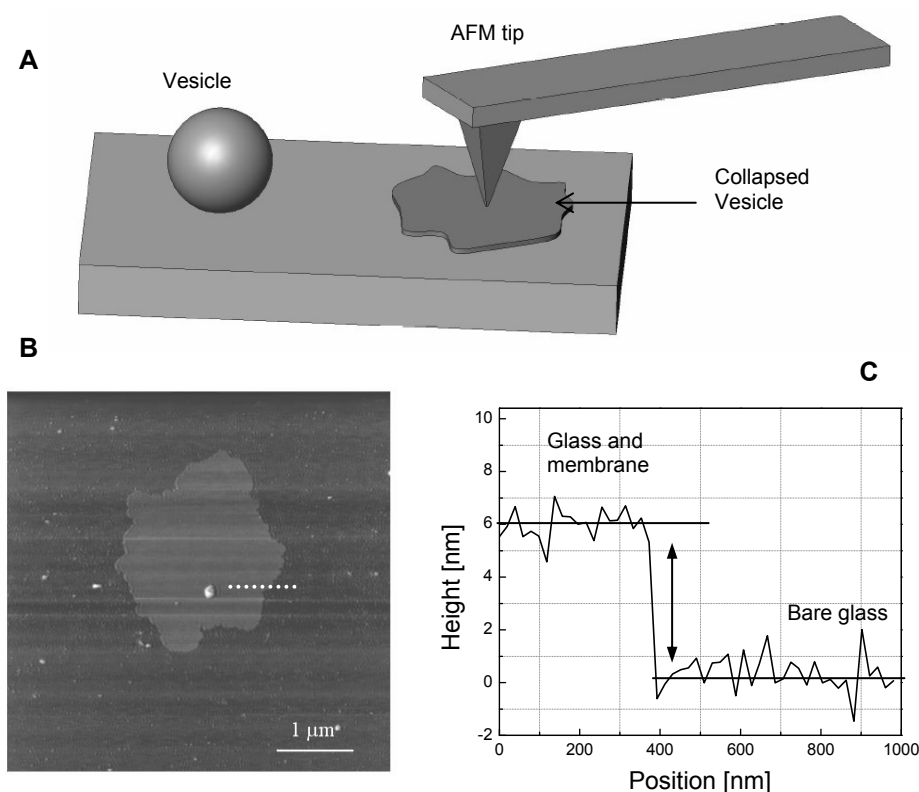


Figure 3.9. (A) Schematics of AFM tip probing membrane patches; (B) AFM image of a lipid membrane patch on a glass surface. (C) Line profile across the membrane patch as shown in (B), indicating deflections in tip height as function of the tip position.

glucose, were prepared using freeze-thaw method (see section 3.6.1). They were added in the cuvette and left for less than 3 hours to collapse and form membrane patches on the flat glass surface at the bottom of the cuvette. Figure 3.9 depicts an AFM image of a membrane patch formed on the glass surface by vesicle collapse. It shows a lipid membrane patch with a thickness of ~ 6 nm. The patch was uniform and homogeneous with no evidence of holes or structural irregularities.

From the AFM measurements performed on several patches, an average membrane thickness of 6 ± 1 nm was found. This thickness is in good agreement with literature values for bilayer membranes [3,23]. The membrane patches measured by AFM were uniform in thickness, suggesting that these supported artificial membranes were single bilayers. The roughness of the glass substrate obtained by AFM measurements is in line with the results obtained elsewhere [28].

3.6.3.2 Electrical measurements on a free-standing BiLM

So far, we observed that the collapse of vesicles on flat supports is possible. Since the aim is the development of a platform to seal a small hole with an artificial BiLM, we explored possibilities for membrane deposition onto a hole by vesicle collapse. Membrane deposition has been previously realized by orienting the vesicles toward the hole via an electrical field [24] and monitoring the process using electrophysiological methods such as DC-voltage clamp [16-18]. We also applied this method to form a membrane onto a hole and to characterize the process of vesicle rupture and membrane formation, sealing quality, thickness of the membrane, and biofunctionality in such a membrane. The system used for such measurements is depicted in Figure 3.10.

Applying a DC voltage as input signal using Ag/AgCl electrodes results in a DC current output due to series resistance introduced in the system from the hole, electrolyte, and electrodes. Sealing of the hole with a membrane will result in a resistance increase to a giga ohm level due to the high resistance of the membrane. As a result, an essential drop in the current output can be observed. This yields information about the membrane and sealing quality, but does not indicate the membrane thickness. Therefore we introduced the channel protein α -Hemolysin in the artificial membrane. α -Hemolysin forms a nanopore in the membrane and allows the transport of ions through a single bilayer membrane. If after insertion of α -Hemolysin in our membrane we have transport of ions, that means that we have a single bilayer membrane.

α -Hemolysin is a bacterial channel protein [29] that causes virulent pathogenic diseases. It is the prototype of a family of toxins secreted by Gram-negative bacteria and causes hemolysis, or lysis of red blood cells, a process to which this protein owes its name. α -Hemolysin from *Staphylococcus aureus* [30,31] consists

of a 293 amino acids long polypeptide chain. Such toxin proteins are described as “amphitropic” [32] and exist as soluble proteins, but become integral (intrinsic) proteins when they bind to the target membrane by spontaneous insertion. Upon membrane-binding the monomers oligomerize, forming a heptameric pore with a 2.9 nm diameter at the exterior that narrows to 1.5 nm in the interior [7,9]. The protein has a mushroom-like shape consisting of cap, rim, and stem domains.

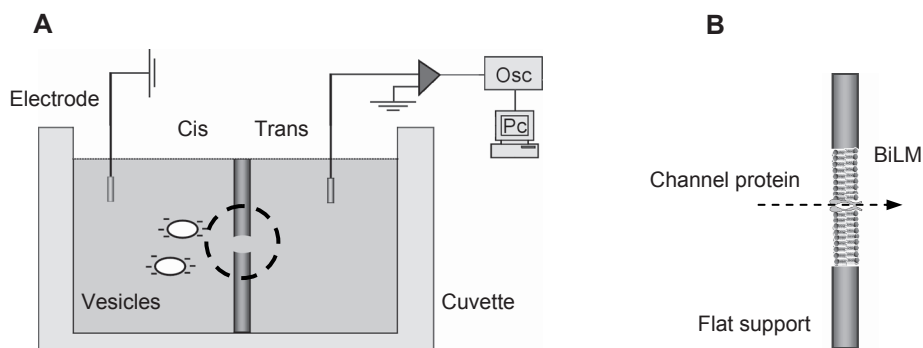


Figure 3.10. Representation of the electrophysiological method. (A) Schematics of the system and vesicles approaching the hole. (B) Zoom in of the hole region as indicated in (A). A lipid membrane spans the hole obtained by vesicle collapse and a channel protein is fused into the membrane.

The channel is defined by the stem domain, a 14 strand antiparallel β -barrel, which is 52 Å long and located in the hydrocarbon region of the membrane. Because of the structure simplicity and functionality, and the pore size reproducibility, this protein is extensively used in artificial membranes for probing and sensing different individual biomolecules, such as DNA [8] and RNA [6] in the presence of an external voltage bias applied across the membrane.

We observed the functionality of α -Hemolysin in our artificial lipid membrane, which mimics the thickness of natural bilayer membranes, by using the DC-voltage clamp method.

Methods and materials

Silicon sample with a single hole. An insulating Si_3N_4 layer of thickness 170 nm was deposited on the top of a silicon wafer (thickness $\sim 525 \mu\text{m}$). A square region of the silicon wafer was etched until reaching the insulating Si_3N_4 layer. The thinned platform area was $\sim 80 \times 80 \mu\text{m}^2$. The sample was further oxidized to

facilitate chemical surface modification. The recipe for sample processing is presented in Appendix B. Single holes were drilled in the thin platform of the silicon sample using Focused Ion Beam [33] drilling technique (FEI FIB Nova 600 NanoLab [34]). Holes with a diameter of 0.5 and 1 μm were drilled using an etching current of 9.7 pA, requiring an etching time of 32 and 128 s, respectively. Diameters of 2 and 3 μm required 67 and 196 s, respectively, when a current of 48 pA was used.

Materials and preparations. For this experiment, salt solution of 150 mM KCL in buffer (Hepes 5 mM / KOH of pH 7.5) was used. The surface of the silicon sample was modified with PLL by incubating the sample for 2 hours in a PLL solution with a concentration of 0.1% PLL in Hepes (5 mM) / KOH buffer (pH 7.5). α -Hemolysin from *Staphylococcus aureus* (product nr. H9395) was purchased from Sigma (Zwijndrecht, The Netherlands). N-Octyl-oligo-oxyethylene (OPOE) was a product of ALEXIS Biochemicals (Leiden, The Netherlands).

Results

The set-up used for this work is shown schematically in Figure 3.10.A. The silicon sample containing a single hole (Figure 3.11) was mounted vertically in a Perspex cuvette to separate two sides of the cuvette (cis and trans). Both compartments were filled with salt solution (typical volume was ~ 1.5 ml). Ag/AgCl electrodes positioned in each compartment were connected to an amplifier and the output signal was monitored with a personal computer.

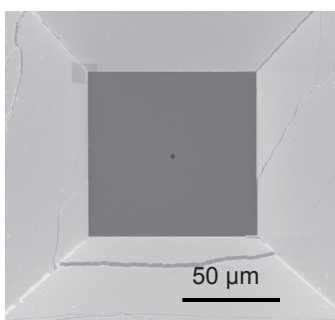


Figure 3.11. SEM image of a silicon sample containing a micro-hole.

To monitor the hole sealing and the membrane quality, a DC voltage was applied as input and the current through the microhole was recorded as output signal. As indicated in the graph in Figure 3.12.A, a major drop in the current took place after adding the vesicles in the cis-compartment of the cuvette. The drop in the current corresponds to the increase of the series ohmic resistance in the system caused by the membrane that spans the hole.

Sealing resistance R_{seal} was calculated by measuring a change in the current $\Delta I = I_2 - I_1$ (see Figure 3.12.B) caused by the change in the voltage ΔV as $R_{seal} = \Delta V / \Delta I$.

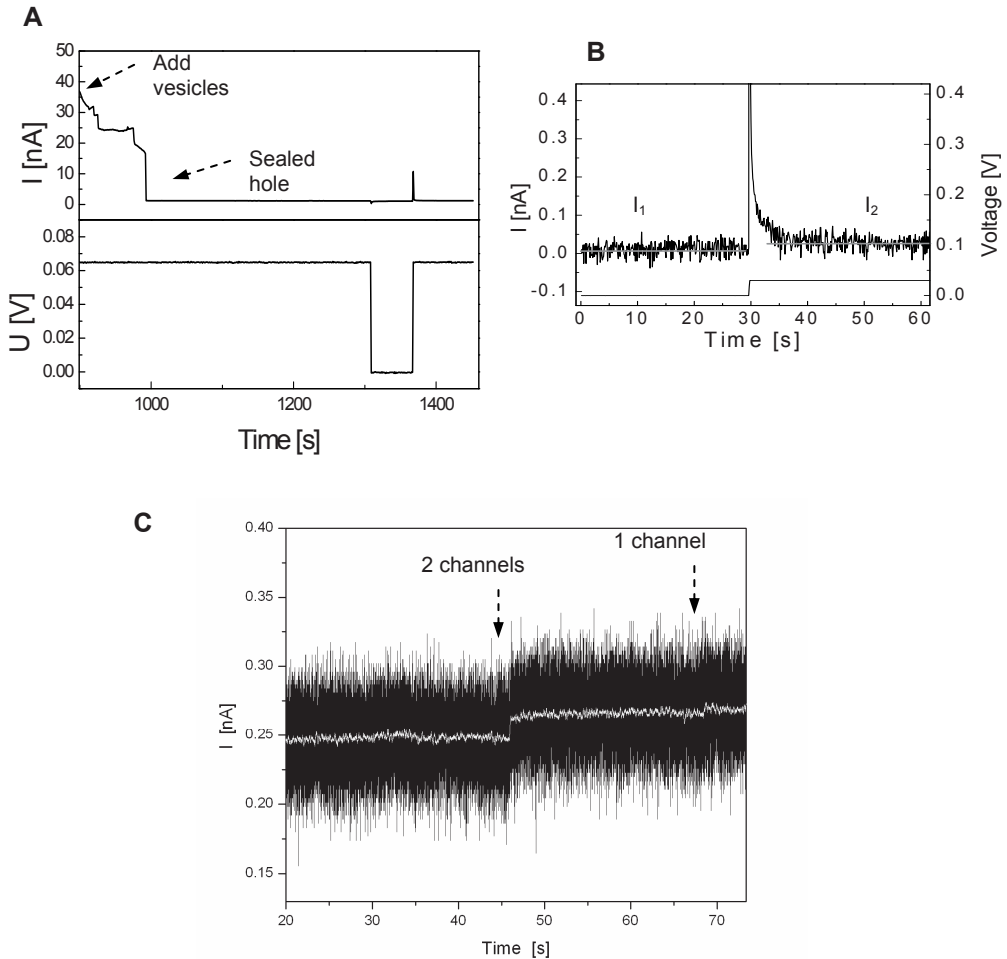


Figure 3.12. Electrical measurement of (A) hole sealing with a BiLM by vesicle collapse. (B) Typical current output before and after a step-voltage change (30 mV) was applied after sealing of the 1 μm hole. Sampling rate was 0.01 kHz. Sealing resistance was $\sim 4 \text{ G}\Omega$. Black line shows the measured data, light gray lines indicate the current plateaus before and after application of the step voltage. (C) α -Hemolysin insertion in the BiLM covering a hole of diameter 1 μm in silicon. Input voltage was 100 mV, sampling rate 1 kHz. Black line represents the measured data, gray line is obtained by applying adjacent averaging smoothing (100 points) of measured data.

Achievement of a high ohmic resistance of $\sim 4 \text{ G}\Omega$ indicated a good sealing of the hole with the lipid membrane. The capacitance of the system in these measurements mainly originating from the silicon sample was very large and could not be compensated, making it practically difficult to calculate the pF-capacitance change after membrane formation on the hole in the silicon support. Sealing of holes from collapsed vesicles was observed for vesicle compositions DPhPC:cholesterol and DPhPC:PA:cholesterol of ratios 95:5 and 90:5:5 wt.-%, respectively. During these measurements, capacitive drift of the silicon was very large and prevented the observation of a stable horizontal DC level prior to vesicle collapse. Figure 3.12.C presents the monitoring of the α -Hemolysin insertion into the free-standing BiLM. About $2 \mu\text{g}$ protein dissolved in 200 ml KCl/Hepes solution containing 0.1% OPOE was added on the same cis side of the cuvette. The step-like current increase of $\sim 10\text{-}12 \text{ pA}$ (appearing around the 46 second in Figure 3.12.C) and $\sim 5 \text{ pA}$ (appearing around the 68 second in Figure 3.12.C) correspond to the insertion of 2 channel proteins and 1 channel protein, respectively [5,7,8]. The insertion of α -Hemolysin and functioning in the membrane indicates that the artificial membrane is a bilayer.

Based on these results we have proven that the vesicles yield a bilayer lipid membrane upon collapse and that such membranes provide a good seal of the hole.

3.7 Conclusions

In this chapter, we have explored different techniques for deposition of a membrane onto a microwell in a flat substrate.

We investigated two approaches to generate an artificial bilayer lipid membrane: brushing method and vesicle collapse. Brushing method applied to microwells resulted in membrane formation. However, the long time (more than 1 week) required for the membrane to thin is a major drawback of such a method.

Membrane formation based on vesicle collapse was more efficient than the brushing method, requiring less time for membrane formation. The best results were achieved for negatively charged vesicles collapsed on PLL coated surfaces that promote electrostatic interaction of the vesicles with the surface. The effect of collapse rate on sealing properties will be explored further in Chapter 4.

AFM measurements of membrane patches on glass supports, obtained by free collapsed vesicles, revealed a BiLM with a uniform thickness of $\sim 6 \text{ nm}$. This result was confirmed by electrical measurements by monitoring the biofunctionality of α -Hemolysin protein, which functions in bilayer environments. In addition, the achievement of the $\text{G}\Omega$ sealing resistance indicates that a good seal of the hole is possible.

Vesicle collapse is a promising method for bilayer membrane formation onto a microhole in a support using the proper vesicle composition. The combination of this method with vesicle manipulation using optical tweezers can lead to a controlled membrane formation, as will be presented in Chapter 4.

Acknowledgement

We acknowledge the support of Dr. Laura Vogelaar from the Membrane Technology Group (University of Twente, The Netherlands) who kindly supplied the PMMA substrates, Dr. Michel Duits from the Physics of Complex Fluids (University of Twente, The Netherlands) who kindly provided the rotary evaporator apparatus, Huib van Vossen and Gerald Roelofs from Mesa⁺ Institute who developed the mask containing pattern of microholes and the Pyrex sample containing microwells, respectively, and Dr. Vishvas Gadgil from MESA⁺ Institute for Nanotechnology (University of Twente, The Netherlands) for the FIB work.

References

- [1] W. Hanke and W.-R. Schlue, *Planar Lipid Bilayers: Methods and Applications*, ed. D.B. Sattelle, Academic Press Limited, London, ISBN 0-12-322994-4, 1993.
- [2] E. Reimhult, F. Höök, and B. Kasemo, Intact Vesicle Adsorption and Supported Biomembrane Formation from Vesicles in Solution: Influence of Surface Chemistry, Vesicle Size, Temperature, and Osmotic pressure, *Langmuir*, 2003, **19**, 1681-1691.
- [3] H.T. Tien and A.L. Diana, Bimolecular Lipid Membranes: A Review and a Summary of some Recent Study, *Chemistry and Physics of Lipids*, 1968, **2**, 55-101.
- [4] R.E. Howard and R.M. Burton, Thin Lipid Membranes with Aqueous Interfaces: Apparatus Designs and Methods of Study, *Journal of the American Oil Chemists' Society*, 1968, **45**, 202-229.
- [5] B. Schuster and U.B. Sleytr, Single channel recordings of α -hemolysin reconstituted in S-layer-supported lipid bilayers, *Bioelectrochemistry*, 2002, **55**, 5-7.
- [6] M. Akeson, D. Branton, J.J. Kasianowicz, E. Brandin, and D.W. Deamer, Microsecond Time-Scale Discrimination Among Polycytidylic Acid, Polyadenylic Acid, and Polyuridylic Acid as Homopolymers or as Segments Within Single RNA Molecules, *Biophysical Journal*, 1999, **77**, 3227-3233.
- [7] D.W. Deamer and D. Branton, Characterization of Nucleic Acids by Nanopore Analysis, *Accounts of Chemical Research*, 2002, **35**, 817-825.
- [8] J. Nakane, M. Wiggan, and A. Marziali, A Nanosensor for Transmembrane capture and Identification of Single Nucleic Acid Molecules, *Biophysical Journal*, 2004, **87**, 615-621.
- [9] J. Schmidt, Stochastic sensors, *Journal of Materials Chemistry*, 2005, **15**, 831-840.

- [10] R. Pantoja, D. Sigg, R. Blunck, F. Bezanilla, and J.R. Heath, Bilayer Reconstitution of Voltage-Dependent Ion Channels using a Microfabricated Silicon Chip, *Biophysical Journal*, 2001, **81**, 2389-2394.
- [11] M.C. Peterman, J.M. Ziebarth, O. Braha, H. Bayley, H.A. Fishman, and D.M. Bloom, Ion Channels and Lipid Bilayer Membranes Under High Potentials Using Microfabricated Apertures, *Biomedical Microdevices*, 2002, **4**, 231-236.
- [12] M. Mayer, J.K. Kriebel, M.T. Tosteson, and G.M. Whitesides, Microfabricated Teflon Membranes for Low-Noise Recordings of Ion Channels in Planar Lipid Bilayers, *Biophysical Journal*, 2003, **85**, 2684-2695.
- [13] L. Vogelaar, J.N. Barsema, C.J.M. van Rijn, W. Nijdam, and M. Wessling, Phase Separation Micromolding – PS μ M, *Advanced Materials*, 2003, **15**, 1385-1389.
- [14] M. Montal and P. Mueller, Formation of biomolecular membranes from lipid monolayers and a study of their electrical properties, *Proc. Natl. Acad. Sci. USA*, 1972, **69**, 3561-3566.
- [15] R.B. Gennis, *Biomembranes Molecular Structure and Function*, ed. C.R. Cantor, Springer-Verlag New York Inc, New York, ISBN 0-387-96760-5, 1989.
- [16] W.A. Vercoutere, S. Winters-Hilt, V.S. DeGuzman, D. Deamer, S.E. Ridino, J.T. Rodgers, H.E. Olsen, A. Marziali, and M. Akesson, Discrimination among individual Watson-Crick base pairs at the termini of single DNA hairpin molecules, *Nucleic Acids Research*, 2003, **31**, 1311-1318.
- [17] J.J. Kasianowicz, E. Brandin, D. Branton, and D.W. Deamer, Characterization of individual polynucleotide molecules using a membrane channel, *Proc. Natl. Acad. Sci. USA*, 1996, **93**, 13770-13773.
- [18] L.-Q. Gu, O. Braha, S. Conlan, S. Cheley, and H. Bayley, Stochastic sensing of organic analytes by a pore-forming protein containing a molecular adapter, *Nature*, 1999, **398**, 686-690.
- [19] W.R. Redwood, F.R. Pfeiffer, J.A. Weisbach, and T.E. Thompson, Physical properties of bilayer membranes formed from a synthetic saturated phospholipids in n-Decane, *Biochimica et Biophysica Acta*, 1971, **233**, 1-6.
- [20] T. Baba, Y. Tushima, H. Minamikawa, M. Hato, K. Suzuki, and N. Kamo, Formation and characterization of planar lipid bilayer membranes from synthetic phytanyl-chained glycolipids, *Biochimica et Biophysica Acta*, 1999, **1421**, 91-102.
- [21] N. Fertig, R.H. Blick, and J.C. Behrends, Whole cell patch clamp recording performed on a planar glass chip, *Biophysical Journal*, 2002, **82**, 3056-3062.
- [22] H.T. Tien, Self-assembled lipid bilayers as a smart material for nanotechnology, *Materials Science and Engineering: C*, 1995, **3**, 7-12.
- [23] M.K. Jain, *Introduction to Biological Membranes*, 2nd edition, John Wiley & Sons, New York, USA, ISBN 0-471-84471-3, 1988.
- [24] C. Schmidt, M. Mayer, and H. Vogel, A Chip-Based Biosensor for the Functional Analysis of Single Ion Channels, *Angew. Chem. Int. Ed.*, 2000, **39**, 3137-3140.
- [25] R.J. Good, R.R. Stromberg, and R.L. Patrick, *Techniques of Surface and Colloid Chemistry and Physics*, Marcel Dekker, Inc., New York, USA, Volume 1, ISBN 0-8247-1262-5, 1972.
- [26] A. Ottova, V. Tvarozek, J. Racek, J. Sabo, W. Ziegler, T. Hianik, and H.T. Tien, Self-assembled BLMs: biomembrane models and biosensor applications, *Supramolecular Science*, 1997, **4**, 101-112.

- [27] K.O. van der Werf, C.A.J. Putman, B.G. de Grooth, F.B. Segerink, E.H. Schipper, N.F. van Hulst, and J. Greve, Compact stand-alone atomic force microscope, *Rev. Sci. Instr.*, 1993, **64**, 2892-2897.
- [28] R. Kassies, Atomic Force Fluorescence Microscopy: Combining the best of two worlds, *PhD Thesis*, 2005, University of Twente, Enschede, The Netherlands.
- [29] F.M. Goñi and H. Ostolaza, *E. coli* α -hemolysin: a membrane-active protein toxin, *Brazilian Journal of Medical and Biological Research*, 1998, **31**, 1019-1034.
- [30] G. Manestrina, M.D. Serra, and G. Prévost, Mode of action of β -barrel pore-forming toxins of the staphylococcal α -hemolysin family, *Toxicon*, 2001, **39**, 1661-1672.
- [31] E. Gouaux, α -Hemolysin from *Staphylococcus aureus*: an archetype of β -barrel, channel-forming toxins, *Journal of Structural Biology*, 1998, **121**, 110-122.
- [32] P. Burn, Amphitropic proteins: a new class of membrane proteins, *Trends in Biochemical Sciences*, 1988, **13**, 79-83.
- [33] J. Orloff, M. Utlaut, and L. Swanson, *High Resolution Focused Ion Beams: FIB and its Applications*, Kluwer Academic / Plenum Publishers, New York, USA, ISBN 0-306-47350-X, 2003.
- [34] FEI FIB Nova 600 NanoLab, FEI, Eindhoven, The Netherlands, 2006, http://www.fei.com/Portals/_default/PDFs/content/2006_06_Nova600NanoLab_pb.pdf
- [35] R. Lipowsky and U. Seifert, Adhesion of vesicles and membranes, *Mol. Crystals*, 1991, **202**, 17-25.
- [36] J.M. Johnson, T. Ha, S. Chu, and S.G. Boxer, Early Steps of Supported Bilayer Formation Probed by Single Vesicle Fluorescence Assay, *Biophysical Journal*, 2002, **83**, 3371-3379.

CHAPTER FOUR

CONTROLLED DEPOSITION OF AN ARTIFICIAL BILAYER LIPID MEMBRANE ONTO MICROWELLS IN A FLAT SUBSTRATE

This chapter describes a procedure for the controlled formation of membrane patches by collapsing lipid vesicles using optical tweezers. The deposition of an artificial bilayer lipid membrane onto a microhole in a flat substrate is presented. Characterization of the artificial membrane and the process of vesicle rupture using different methods is discussed.

4.1 Introduction

In the previous chapter, a protocol for membrane deposition using vesicle collapse was developed. In this chapter this method is further developed by adding spatial control of the vesicle collapse by means of optical tweezers.

The aim in this chapter is manifold: (1) to develop a method for controlled deposition of a membrane by means of lipid vesicles, (2) to characterize the vesicle collapse process, and (3) to realize and characterize hybrid flat substrates.

We showed that vesicle collapse on solid supports is possible. However, for the deposited membranes we were not able to control the position of collapse. In addition, this process was taking several hours. In order to have fast vesicle collapse onto a specific hole in the flat substrate we need to specifically control and manipulate the vesicles.

There are several ways to manipulate the vesicles. One method is electrophoretic self-positioning of charged lipid vesicles. Here the vesicle is oriented towards an electrical field gradient emerging from a hole through a support that separates two fluid compartments. The fact that our substrate is made of glass and that the geometry consists of microwells in a flat substrate, does not easily allow the use of this method because no electrical gradient emerging from the hole can be easily realized. An alternative way for manipulation of vesicles is to use optical tweezers (OT). Previous work has shown that giant vesicles could be trapped with optical tweezers [1]. Considering the geometry of our substrate, consisting of microwells, OT is a better suited method. OT can be easily integrated with the flat transparent substrates and offers a resolution in submicrometer range. We have explored the use of OT in our system to manipulate and collapse vesicles onto a hole to form a membrane.

The experiments in this chapter required redesigning of the substrate. To overcome the problems we encountered in Chapter 3 due to small well depth, we developed substrates with deeper wells.

We present a protocol using OT to manipulate and deposit unilamellar lipid vesicles onto microwells (Figure 4.1). We visualized the vesicle collapse by TIRF and epifluorescence.

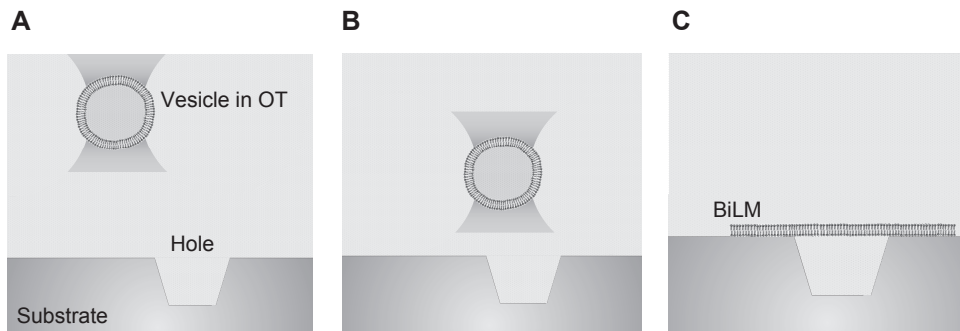


Figure 4.1. Schematics of controlled membrane deposition on a microhole. (A) Vesicle in the optical trap. (B) Manipulating the vesicle toward a hole prior to collapse. (C) Membrane deposited onto the hole upon vesicle rupture.

4.2 Manipulation and controlled rupture of the vesicles

4.2.1 OT manipulation

Trapping of the particles with OT [2-4] takes place for particles with a refractive index higher than the surrounding medium. In the case of vesicle formation in buffer, the refractive index in the interior and exterior of the vesicle is the same. The lipid wall, having a refractive index slightly different from the solution, enables trapping of the vesicles but the trapping force is extremely weak [1]. Therefore, we increased the refractive index of the vesicle interior by loading them with a glucose solution.

We characterized the trapping of vesicles by measuring the maximum trapping force. The maximum trapping force is determined by the so-called escape force, the minimum force that has to be exerted on the vesicle to pull it out of the trap. The maximum trapping force is slightly smaller than the escape force. To measure the escape force we apply a drag force by introducing a fluid flow around the vesicle.

The maximum trapping force F_{trap}^{max} for a vesicle with radius r , immersed in a solution with viscosity coefficient η , can be calculated against viscous drag F_{drag} [5,6] by the following relation:

$$F_{trap}^{max} = F_{drag} = \beta v_{esc} \quad [4.1]$$

where v_{esc} is the fluid velocity at which the vesicle escapes the optical trap and β is the drag coefficient, which according to Stokes' Law for a spherical particle is defined as:

$$\beta = 6\pi\eta r \quad [4.2]$$

We gradually increased the flow speed v to increase the drag force exerted on the trapped vesicle. The vesicle escapes the trap when $v > v_{esc}$. To determine the escape velocity, we recorded a video of the vesicle escaping from the trap. By measuring the vesicle displacement Δx from frame to frame and knowing the frame rate f , the velocity is calculated as $v_{esc} = \Delta x f$. We measured the maximum trapping force for vesicles of different diameters.

Glucose concentration. The maximum trapping force for a vesicle with radius r is proportional to the relative difference of the dielectric constants of the vesicle (glucose) $\epsilon_{glucose}$ and the surrounding medium (water) ϵ_w as [8]:

$$F_{trap}^{max} \sim \left(\frac{\epsilon_{glucose}}{\epsilon_w} - 1 \right) \quad [4.3]$$

where $\epsilon_{glucose} = \epsilon_0 n_{glucose}^2$ and $\epsilon_w = \epsilon_0 n_w^2$ (ϵ_0 is vacuum dielectric constant, $n_{glucose}$ is glucose refractive index, and n_w is water refractive index). The index of refraction scales proportionally with glucose concentration. The relation between the glucose molarity and refractive index is given by [7]:

$$n_{glucose} = n_w + 0.0252 M_{glucose} \quad [4.4]$$

Using Eq. 4.4, we find:

$$F_{trap}^{max} \sim 0.0504 \frac{M_{glucose}}{n_w} \quad [4.5]$$

where we neglected higher order terms in $M_{glucose}$. As shown from Eq. 4.5, the trapping force linearly depends on the glucose concentration inside the vesicle. A glucose concentration of 400 mM was a reasonable choice to load the vesicles. Such a concentration enables a reasonable trapping force in a moderately viscous medium, preventing any negative effect of the high viscosity on vesicle formation.

Materials and methods

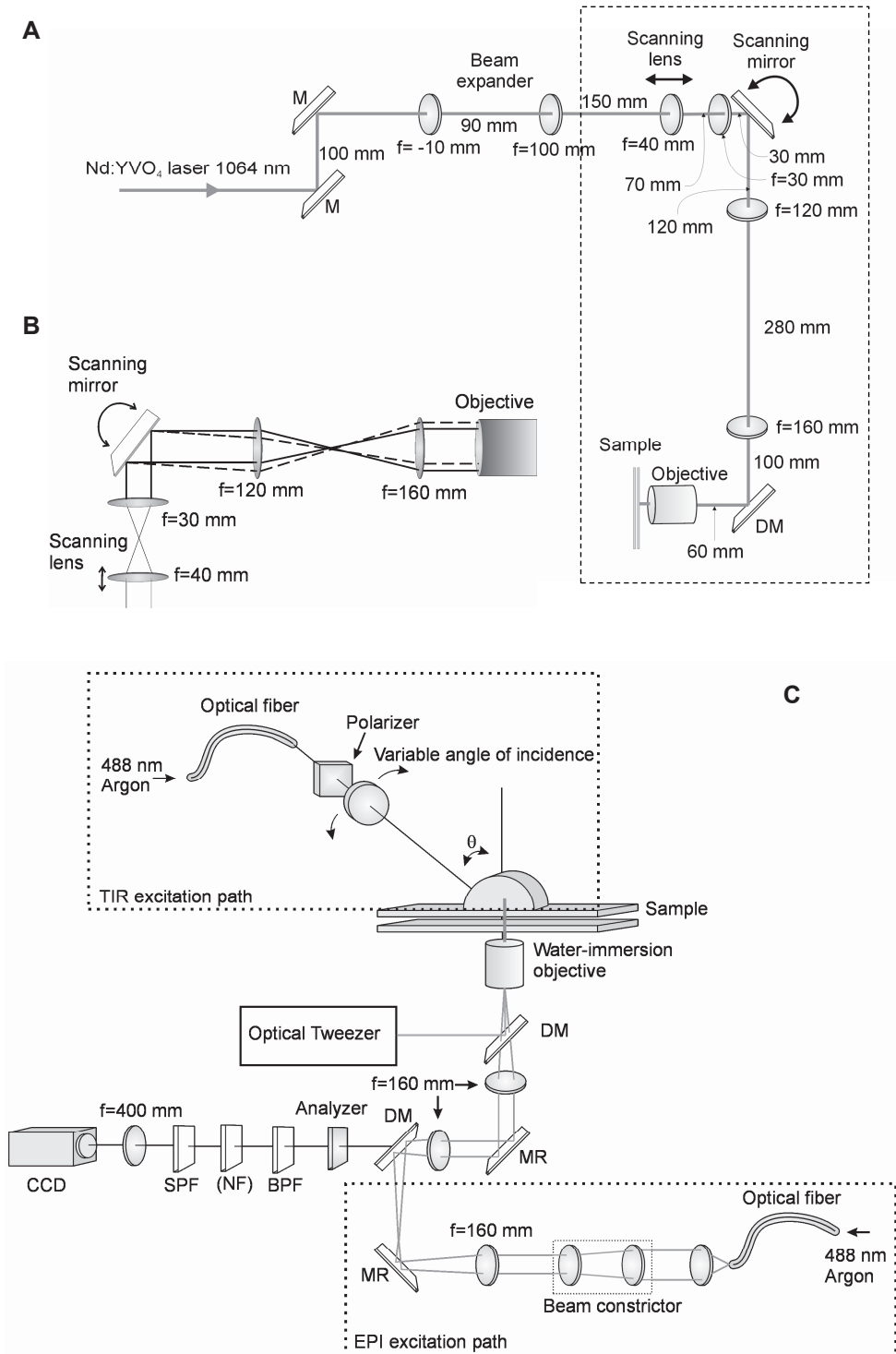
Materials. 1,2-Diphytanoyl-sn-Glycero-3-Phosphocholine (DPhPC), was purchased from Avanti Polar Lipids (Alabaster, USA). Cholesterol (3β -Hydroxy-5-cholestene, $C_{27}H_{46}O$) was obtained from Sigma (Zwijndrecht, The Netherlands). PD10 desalting columns were purchased from Amersham Biosciences (Roosendaal, The Netherlands). Glucose (D(+)-Glucose) and chloroform were products of Merck (Darmstadt, Germany). Microscope slides and coverslips (thickness of 170 μ m) were obtained from Menzel-Gläser (Braunschweig, Germany). Parafilm (Parafilm M) was purchased from Alcan Packaging (Zutphen, The Netherlands).

Vesicle preparation. Unilamellar vesicles were composed of 1,2-Diphytanoyl-sn-Glycero-3-Phosphocholine (DPhPC) and cholesterol of ratio 95:5 wt.-%. Vesicles loaded with glucose were prepared by vacuum drying a lipid film of lipids mixture at the bottom of a round flask and swelling the vesicles using buffer containing 400 mM glucose. Next freeze-thaw was applied by placing the flask once in liquid nitrogen (-196 °C) and then in water (~ 40 °C), repeating this cycle 5-8 times to form unilamellar vesicles. Finally, the vesicle solution was poured through a PD10 desalting column to remove the glucose from the bulk solution, yielding vesicles loaded with glucose (see section 3.6.1).

Set-up

We used a dedicated OT set-up to trap vesicles. OT was combined with epifluorescence and TIRF microscopy to visualize the trapped vesicles. A schematic drawing of the set-up is presented in Figure 4.2.

Figure 4.2 (facing page). Optical tweezers set-up. (A) Optical pathway for 3D movable optical trap. The diameter of the laser beam (Nd:YVO₄ laser, Spectra Physics, wavelength 1064 nm) is expanded to fill the back aperture of the microscope objective (Leica water immersion 100×1.2 NA). The location of trap focus can be computer controlled by means of scanning lens and mirror; (B) Zoom in of (A) indicated by the dash-rectangular selection. (C) Optical pathways for fluorescence excitation and detection. Argon laser line is split using a beam splitter to enter both optical fibers for EPI and TIRF. For EPI illumination, the back aperture of the microscope objective is slightly overfilled by the expanded beam. For the TIRF illumination, the angle of the incident light on the interface of the sample surface can be varied by changing the whole 'arm' of aligned optics. The same microscope objective is used to collect the fluorescent emitted light from the sample, routed by the dichroic mirror to the detection path, where it is further filtered and detected via a frame transfer intensified CCD camera (Pentamax, Princeton Instruments, Roper Scientific B.V., Vianen, The Netherlands). M=mirror, DM=Dichroic mirror, BPF=band pass filter, NF=neutral density filter, SPF=short pass filter, CCD=CCD camera.



The trap position is controlled by a computer. The movement of the trap position is enabled by a translating lens and a scanning mirror (see Figure 4.2.B). In this way the trap position can be controlled in both the axial and lateral directions. Due to the losses by reflections from different optical components and due to the losses in the high NA objective [5], only $\sim 30 - 40\%$ of the trap laser output power (2 W) was efficiently used for trapping.

The flow cuvette

A home-made cuvette was used to enable the controlled flow of the vesicles (see Figure 4.3). The cuvette was prepared as a sandwich of a microscope slide and a coverslip, with a parafilm layer as a spacer between them. Parafilm is a semitransparent, flexible thermoplastic, and a highly waterproof sheet material. The parafilm also seals the cuvette. The sandwich was first heated up to melt the parafilm. Later, it was left at room temperature to cool down, resulting in a solidified layer that grafts on the surfaces of both glass plates. The cuvette had an inlet and an outlet in order to flow the vesicle solution in and out of the cuvette. The flow speed of the vesicle solution was controlled by varying the hydrostatic pressure at the cuvette input upon vertical displacement of the reservoir solution that was connected to the cuvette input.

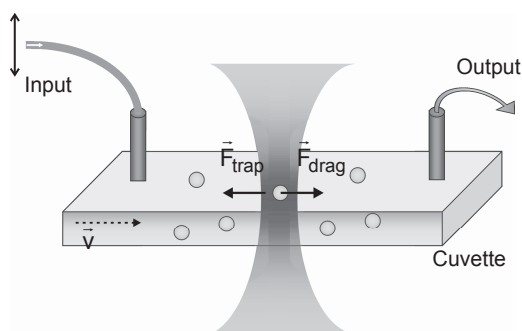


Figure 4.3. Schematics of the vesicle trapping and flow in the cuvette. The arrow indicates the vertical movement of the sample reservoir.

Results

Figure 4.4.A presents the maximum trapping force for vesicles (DPhPC-cholesterol composition) with different diameters. The results shown here were obtained for a trap laser output of 2 W. Further tests showed that the trapping was also achieved for different output laser powers, varying from 0.2 to 2 W. Vesicles of different sizes with a radius varying from 0.23 to 1.62 μm were trapped. The data show a linear behavior (correlation coefficients of 0.9 and 0.8 were found for dataset 1 and 2, respectively). The datasets 1 and 2 were measured on different days using different vesicle batches. The maximum

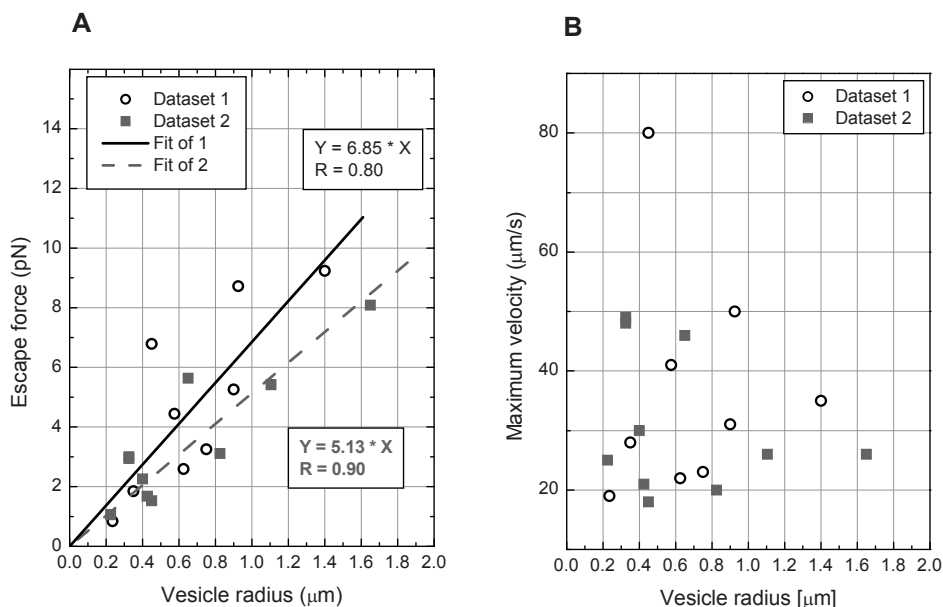


Figure 4.4. OT manipulation of vesicles. (A) Experimentally measured escape forces of 400 mM glucose-loaded vesicles for different diameters. The output laser power was kept constant at 2 W, wavelength was 1064 nm. (B) Experimentally measured escape velocity of vesicles in (A) caused by the drag force of the flow.

trapping force determines the maximum manipulation speed, which is plotted in Figure 4.4.B. Previous studies have shown that for spherical particles of radius r much smaller than the laser wavelength, the maximum trapping force depends on r^3 , for particles much larger than the wavelength the force is independent of r [9], and for the regime in between, the force exhibits a linear behavior [10]. The dependency in our case shows a reasonable linear behavior, as expected. For vesicles smaller than the wavelength, there is a deviation from the expected behavior. Since the vesicles are flexible structures, they tend to elongate when the drag force is increased. Therefore the frontal surface area decreases and alters the drag force. In this case, the determined maximum trapping force may be overestimated. Changes in the vesicle shape geometry might influence the linear behavior of the force as function of the initial diameter.

There is a slight change in the slope of the linear fit of measurements performed on different days (6.85 and 5.13 for dataset 1 and 2, respectively). Although the preparation procedure is the same, the batches will not be identical in terms of vesicle stability in time and leakage, and the remaining amount of glucose in the

bulk medium. These factors contribute to a small change in refractive index that influences the trapping force.

4.2.2 Controlled pattern formation of membrane patches

In this section, we study the controlled deposition of the membrane by inducing collapse of the vesicles.

For these measurements, a bare glass surface and a PLL modified surface were used. Once a vesicle was brought in contact with the PLL modified glass surface using OT, a fast rupture of the vesicle was observed, followed by formation of a membrane patch within a few seconds. In Figure 4.5, a pattern of 2×2 collapsed vesicles is presented. Vesicle collapse was reproducible and reliable. Experimentally we observed that when a vesicle approached a surface already covered by a patch, it did not collapse. The collapse was not affected by the laser power.

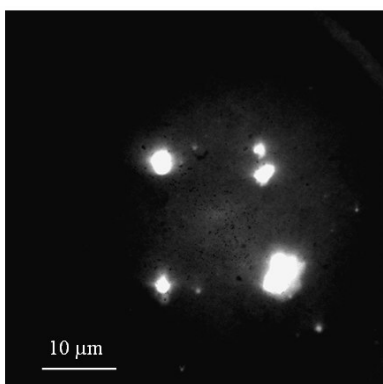


Figure 4.5. Pattern of controlled collapsed vesicles (DPhPC-cholesterol composition) on a PLL modified glass surface using optical tweezers.

Attempts to bring a glucose loaded vesicle with OT in contact with a bare glass surface did not result in vesicle collapse. The vesicle continuously attempted to escape the trap when brought close to the surface. For these experiments, vesicles composed of DPhPC and cholesterol were used. A similar behavior was observed for other vesicle compositions (see section 3.6.1) as well.

4.3 Characterization of vesicle collapse

After developing the procedure for membrane deposition based on vesicle collapse with OT, membranes were characterized with respect to homogeneity and number of bilayers. In this section, the characterization and the dynamics of the collapse process using epifluorescence and TIRF techniques is described.

Materials and methods

Preparation for epifluorescence observation. Commercial chambered glass coverslips with a polystyrene cuvette on the top containing small compartments of ~ 0.8 ml (Lab-Tek™ Chambered Coverglass, VWR International B.V., Amsterdam, The Netherlands) were used. The glass surface was modified with PLL (poly-L-lysine hydrobromide, Sigma, Zwijndrecht, The Netherlands) by incubating with 0.01% PLL in PBS buffer at 4 °C for a few hours. Before use, excess PLL was rinsed from the cuvette with buffer. Glucose loaded vesicles (DPhPC:cholesterol of ratio 95:5 wt.-%) were prepared using the freeze-thaw method and labeled prior to use with DiO fluorophore (3,3'-Diocetadecyloxycarbocyanine perchlorate, Sigma, Zwijndrecht, The Netherlands) by adding ~ 30 μ l of 10 μ g/ml DiO/methanol stock solution in 1 ml vesicle solution.

Preparation for TIRF. A cuvette made of two glass coverslips (170 μ m thick), with a water resistant tape spacer of less than 50 μ m was prepared. This spacing corresponds to the height tolerance of the actual microscope objective, allowing access to the upper surface of the cuvette with OT. The top coverslip surface was modified with PLL and the DiO labeled vesicles (DPhPC-cholesterol composition) were introduced in the cuvette. Vesicles and PLL surface modification were prepared as presented above.

4.3.1 Vesicle size vs. membrane patch area

AFM measurements confirmed that the membrane patches were single bilayers (see section 3.6.3). Here we begin with an intact vesicle, let it collapse, and measure patch formation on a surface in a controlled collapse process. We now have the opportunity to measure with fluorescence the vesicle collapse and characterize the patches. The fluorescently labeled vesicles were trapped with OT and brought to the bottom of the cuvette to collapse under continuous observation by epifluorescence microscopy. Figure 4.6 shows epifluorescence images of a vesicle in the optical trap prior to and after collapse on the glass surface.

First we want to measure if a vesicle fully collapses by comparing vesicle cross-sections with the surface area of the formed membrane. When a vesicle is completely collapsed, the area of the formed membrane patch should equal the vesicle area prior to collapse, being $S_{vesicle} = 4\pi r^2$, where r denotes vesicle radius. Hence, the vesicle cross-section area in the optical trap $S_{cross} = \pi r^2$, should be 4 times smaller than the area of the membrane patch after collapse.

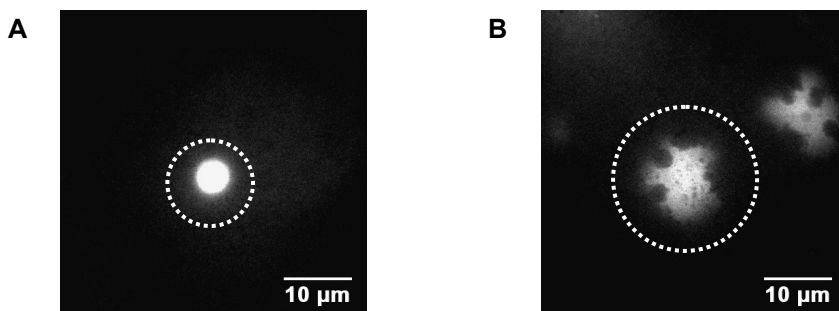


Figure 4.6. Epifluorescence images of (A) a vesicle in the optical trap (area $\sim 20 \mu\text{m}^2$) presented by the bright spot within the dotted circle, (B) membrane patch on a glass surface after collapse of the vesicle in (A) (area $\sim 78 \mu\text{m}^2$) presented by the bright area within the dotted circle.

Analysis using ImageJ [11] yielded a vesicle cross section area of $20 \mu\text{m}^2$ (Figure 4.6.A) and a membrane patch area of $78 \mu\text{m}^2$ (Figure 4.6.B), yielding a ratio of the membrane patch area to the vesicle cross section area of 3.9. A ratio ~ 4 was obtained for several observations, indicating that the unilamellar vesicles collapse totally on the surface, forming in this way single bilayer lipid membrane patches.

4.3.2 Dynamics of vesicle rupture

The controlled collapse of the vesicles enables us to follow the collapse process very carefully in time. In this section, we describe controlled vesicle collapse and simultaneous monitoring during patch formation and the characterization of the dynamics of the collapse process.

Total internal reflection fluorescence (TIRF) microscopy was used to characterize the deposited artificial membrane patches and the collapse process. For these measurements, the trapped vesicles were first visualized using epifluorescence and moved towards the upper PLL coated surface. Next, during the vesicle collapse on the surface, TIRF was used to monitor the dynamics of the collapse. During the measurements the laser trap was continuously switched on.

Figure 4.7 depicts an epifluorescence image of a trapped vesicle as well as time sequences of TIRF images recorded during vesicle collapse. We began with a small vesicle cross section and continuously monitor vesicle widening. We analyzed sequences of images by determining the surface area of the membrane patch in order to follow the collapse in time, as presented in Figure 4.8. The ratio of the collapsed membrane patch area with the vesicle cross section area is ~ 3.9 , in agreement with previous results obtained by AFM measurements.

Moreover, these experiments demonstrate that the collapse process is fast, with a time constant of about 200 ms, as shown in Figure 4.8.

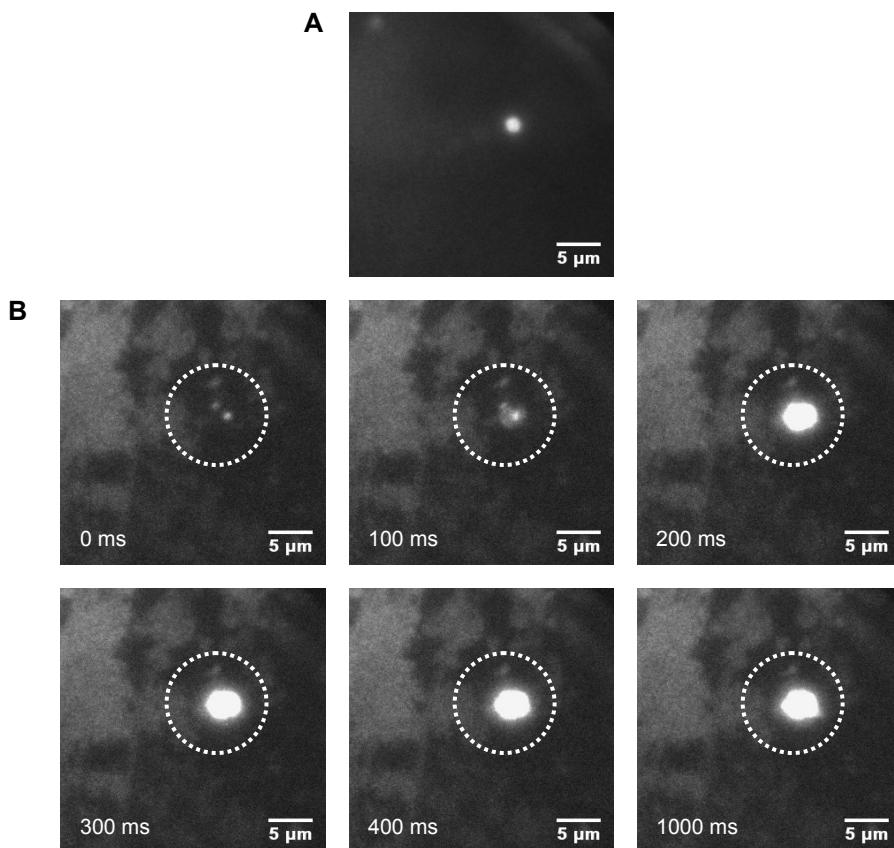


Figure 4.7. (A) Epifluorescence image of a trapped vesicle (*DPhPC-cholesterol* composition) with OT; (B) time sequences of TIRF images during vesicle collapse.

Previous studies have shown that the vesicle collapse depends on surface chemistry [12]. The collapse process is initiated with an adsorption of the vesicle on the surface without rupture, followed by a strong surface interaction resulting in collapse. In our case, the electrostatic interaction between the negative lipid charge and positive PLL charge on the surface drives the interaction and vesicle adsorption. The process is followed by an expansion of the adsorbed vesicle area on the surface, and as can be seen from Figure 4.8, a subsequent fast vesicle collapse occurs. The rupture of the vesicle is driven by the tension exerted on the vesicle wall due to vesicle deformation [12,13] and starts when the adhesion

interaction overcomes the membrane lipid cohesion. The fast kinetics of the vesicle rupture in our case is influenced by the strong electrostatic interaction. Previous work has shown a dependence of the vesicle rupture kinetics on the surface properties [12]. The properties of the vesicles and surfaces used in this work are different from ours, and thus prevent a direct comparison of the results.

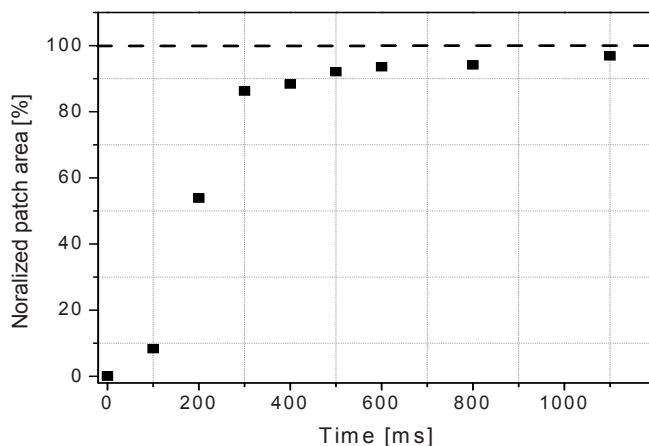


Figure 4.8. Patch area as a function of time. Patch area is normalized by $4 \times$ vesicle cross section.

4.4 Artificial BiLM deposition onto microwells in a flat substrate

In this section, we show the controlled deposition of the lipid membranes onto microwells in a flat Pyrex substrate based on vesicle collapse on charged surfaces. The vesicles were directed to collapse on specific holes using optical tweezers. Sealing of the microwells and membrane stability were characterized using fluorescence microscopy.

4.4.1 Substrate fabrication

In the substrates we used in Chapter 3, either the wells were not deep enough to discriminate fluorescence signals from the membrane on the hole and the well interior (Pyrex), or the substrate material (PMMA) was fragile and not reusable. Therefore, we improved the design of Pyrex substrates with respect to the well depth and substrate thickness. Samples containing arrays of microwells were prepared by using RIE technique. Patterns of hole arrays with diameters of $1\mu\text{m}$

and larger were etched in the Pyrex substrates of thickness ~ 150 - $180 \mu\text{m}$. The depth of the microwells was $\sim 4.5 \mu\text{m}$ achieved with reasonable etching time. The technology limits etching of deeper wells. The recipe applied for substrate fabrication is described in Appendix B.

In summary, during the course of the project we developed 3 substrate configurations: Pyrex, with small well depth ($\sim 400 \text{ nm}$); PMMA, which is flexible in preparation, but not reusable and fragile; and Pyrex with deep wells. For the remainder of the work we used the Pyrex substrates containing deep wells.

4.4.2. Hole sealing with an artificial BiLM

Experimental procedure. A polystyrene cuvette, containing small volume compartments (0.8 ml) was mounted on the Pyrex sample with microwells, using Parafilm. Vesicles composed of DPhPC-POPG-cholesterol (ratio of 70:25:5 wt.-%) were used for these measurements. This vesicle composition was used because of the reliable collapse of vesicles on a surface facilitated by electrostatic interaction when using OT. Additionally, these vesicles did not exhibit a high uncontrolled vesicle collapse that modifies the surface and prevents giant vesicle collapse. The vesicles were prepared using freeze-thaw method. Before use, they were labeled with DiA fluorophore ([4-(4-(dihexadecylamino)styryl)]-N-methylpyridinium iodide (excitation 488 nm, emission LP 560 nm, Molecular Probes, Leiden, The Netherlands) by adding $\sim 1 \mu\text{l}$ of $400 \mu\text{g/ml}$ DiA/Methanol stock solution in 1 ml vesicle solution. The glucose loaded vesicles, labeled with DiA, were trapped with OT and monitored using epifluorescence (excitation 488, emission filter BP 610/75). OT laser output was kept constant at 1 W. To locate

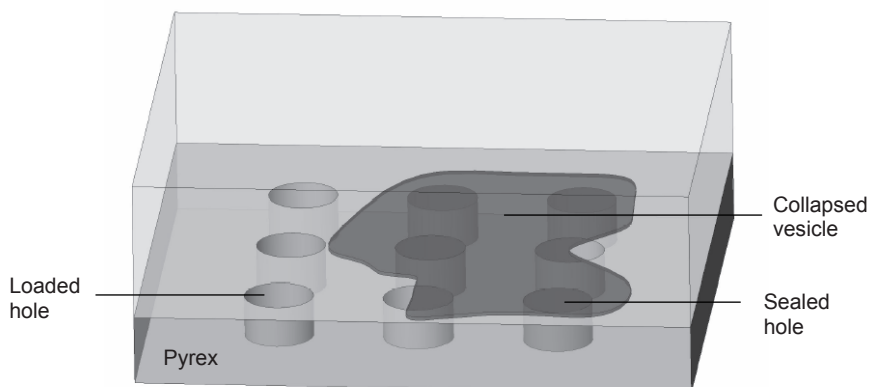


Figure 4.9. Schematic representation of the sample with micro-holes sealed with the membrane and incubated with aqueous calcein solution.

the vesicles for collapse on a certain hole position, white light imaging was used simultaneously with fluorescence imaging. After covering several holes with lipid membranes, the sample was transferred to the confocal fluorescence microscope to characterize the deposited membranes. In between measurements, the deposited membranes were stored for several days at 4 °C to prevent bacterial growth. A schematic of the sample with microwells is depicted in Figure 4.9.

Results. Confocal images of holes (diameter of 1 μm , depth of 4 μm , 3 x 3 pattern of holes) that were sealed with lipid membranes are presented in Figure 4.10.A. The holes were sealed first with a membrane, and later calcein dye (Sigma, Zwijndrecht, The Netherlands) was added to the bulk solution to probe possible diffusion into the holes. The negatively charged structure of the calcein makes it a good cell-impermeable molecule, unless the membrane contains pores through which calcein can passively diffuse. The confocal plane in the recorded image was $\sim 2 \mu\text{m}$ away from the surface into the hole. The bright spots represent the loaded holes that were not sealed properly with the lipid membrane. So, in total 4 out of 9 holes have a good seal. As a control, the membranes were ruptured by adding a detergent (Triton X100). When 20 μl of 10% Triton stock solution in water was added in $\sim 500 \mu\text{l}$ bulk medium, the sealed holes were also loaded with calcein within a minute after administration of the detergent (Figure 4.10.D).

Quantitative analysis of the data of Figure 4.10 is done by calculating fluorescence intensity profiles of cross sections through the holes (see Figure 4.11). The peak intensity difference between the loaded and the unloaded holes could be clearly distinguished (Figure 4.11.A). When the membrane was ruptured by Triton, the fluorescence intensity among the holes became comparable, as expected (see Figure 4.11.B).

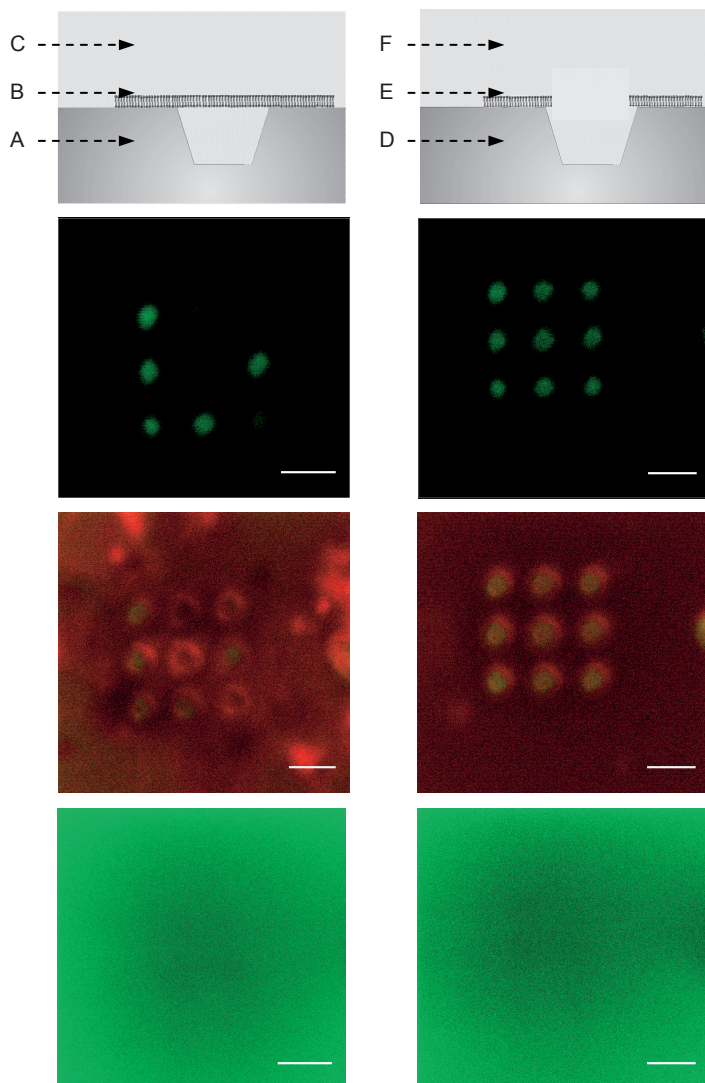


Figure 4.10. Schematic representation of a microwell in a Pyrex substrate, sealed with lipid membrane (top-left) and containing a ruptured membrane (top-right). Horizontal arrows indicate the focus position for the CLSM images. CLSM images of (A) sealed 1 μm holes with a membrane formed by vesicle collapse (DPhPC:POPG:cholesterol). Depth of image is $\sim 2 \mu\text{m}$ away from the surface deep into the hole. (B) Image depth on the surface. (C) Image depth in the bulk medium. (D) Loaded holes with Calcein after the rupture of the membrane by adding 10% Triton. Image depth is $\sim 2 \mu\text{m}$ below the hole surface. (E) Image depth on the surface. (F) Image depth in the bulk medium. Green and red colors correspond to the fluorescence intensity of Calcein solution and DiA labeled membrane. In all these images, the scale bar is 2 μm .

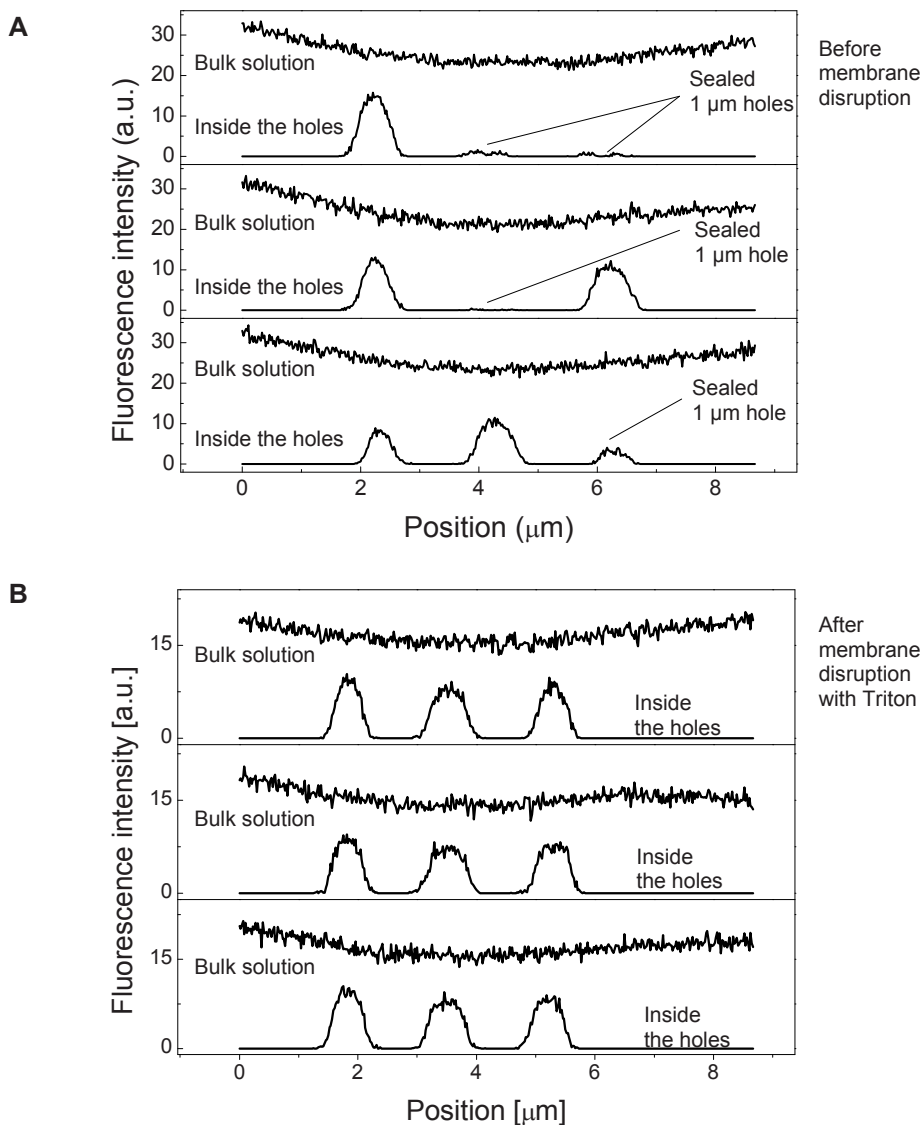


Figure 4.11. Fluorescence intensity profiles for cross sections through the holes in Figure 4.10. (A) Sealed holes with lipid membrane; (B) diffusion of the calcein aqueous solution into the sealed holes after the rupture of the membrane with Triton.

There is a difference in the fluorescence intensity level between the bulk and the peak intensity in the loaded holes. First, dye characteristics such as bleaching

and chemical stability are some factors that could influence this intensity difference. Secondly, to define the intensity profiles, we used averaging over rectangular region of interest rather than over a line in order to reduce the noise of the signal.

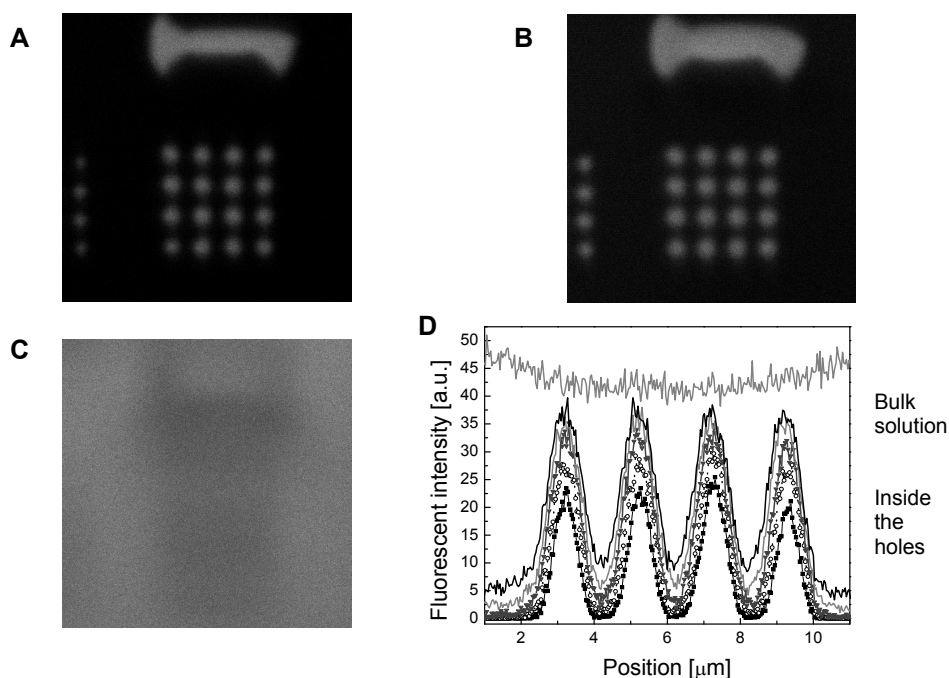


Figure 4.12. Holes of $1\ \mu\text{m}$ diameter loaded with Alexa 568 dissolved in DMSO. Confocal slice (A) $\sim 2\ \mu\text{m}$ below the surface (in the holes), (B) close to the surface, (C) in the bulk medium. (D) Fluorescence intensity line profile in the bulk and at different depths (step size of $0.9\ \mu\text{m}$) into the holes. Black line indicates the intensity profile close to the surface.

Since the intensity in the holes (on a CLSM plane) shows a Gaussian distribution, this averaging causes a reduction of the peak intensity, therefore further increasing the difference in the intensity level between the bulk and the holes. As a control, $1\ \mu\text{m}$ free holes were loaded with a dye solution (see Figure 4.12) chosen for a high extinction coefficient and stability (Alexa 568 dissolved in DMSO). Fluorescence intensities of line profiles through the holes are presented in Figure 4.12.D. The results indicated that peak intensity decreased when imaging deeper into the hole. Even in this case, although a line profile was used, there is still some difference between the fluorescence intensity in the holes and the bulk solution.

After sealing the holes with a membrane and adding the calcein, the sample was kept at 4 °C for ~ 1 week. The holes remained sealed until the soap was added, clearly indicating the good temporal stability of the membrane seal. Furthermore, the membrane showed a remarkable stability against tension forces, mechanical disturbance, temperature fluctuations, and vibrations occurring during the sample transportation. We demonstrated sealing of 1 μm holes. We also explored sealing of bigger holes. Holes with a diameter up to 5 μm could be sealed.

Additional vesicle compositions

We also investigated the collapse of other vesicle compositions that have shown a higher free collapse rate than the currently used composition (see Chapter 3).

SDS-vesicles collapsed onto holes. Addition of 0.017 mM SDS to the vesicle (DPhPC-cholesterol composition) solution increased the rate of vesicle collapse. Sealing of a hole with a membrane containing SDS was achieved for holes of 1 μm diameter. However, the addition of SDS increases the instability of the membrane, a fact that could explain the difficulty to seal holes bigger than 1 μm .

Asolectin-based vesicles. Attempts to seal the holes with membranes composed of Asolectin:cholesterol (ratio of 95:5 wt.-%) were not successful. Asolectin-based vesicles showed a fast uncontrolled collapse on the surface, resulting in a modified surface with membrane patches, which prevents the controlled collapse. Furthermore, the size distribution of vesicles prepared in this manner was dominated by small vesicles, which prevented sealing of the holes.

4.5 Conclusions

In this chapter, we have developed a protocol for controlled deposition of a lipid bilayer membrane onto microwells in a flat platform and demonstrated that a good seal of these microwells is possible.

The membrane deposition was obtained by collapsing unilamellar vesicles in a controlled fashion using optical tweezers. To the best of our knowledge, this is the first time demonstrating the use of OT to induce controlled collapse of vesicles onto a microwell. Trapping of the vesicles was realized by increasing the refractive index inside the vesicles by loading them with glucose. The observed trapping allows a manipulation speed of the vesicles at ~ 60 $\mu\text{m/s}$.

Controlled collapse of vesicles was further facilitated by enhancing their collapse rate by positively charging the substrate surface. Electrostatic interaction of the negatively charged vesicles with the positively charged substrate surface significantly improved the collapse process. Collapse of not only vesicles having a

negative net-charge, but also those based on zwitterionic lipid vesicles (zero net charge), was observed. The combination of DPhPC-POPG-Cholesterol lipids (70:25:5% wt.-%) showed a good controlled collapse on PLL modified surfaces as well as a low uncontrolled collapse rate from the free moving vesicles.

Epifluorescence and TIRF measurements showed a total vesicle collapse. Use of TIRF enables following the dynamics of collapse. The collapse process showed a fast dynamics, with a time constant ~ 200 ms. TIRF is a particularly appropriate tool to monitor such membrane associated processes.

Membranes sealing microwells in flat Pyrex substrates remained stable for \sim one week. Although no further testing regarding the membrane stability for longer time periods was made, this is quite an achievement when compared to the stability of planar membranes developed so far that last typically for a few hours [14-17]. No pressure control and vibrational isolation was required to avoid any uncontrolled membrane rupture, another improvement compared to the traditional planar lipid membrane systems [18,19], which are mechanically very sensitive, extremely delicate, and susceptible to breakage.

The hole dimensions in our system are scaled down to ~ 1 μm , and are much smaller compared to previously developed systems (typical hole sizes used for planar membranes are > 30 μm [18-25]. The reduction of the free standing membrane area positively influences the membrane stability [14,15]. In all traditional systems, both sides of the compartments separated from the membrane are accessible [18,19,22-25]. In our system, however, the microwells comprise a small and well-defined volume, which are accessed only from outside the membrane. The concept of a defined volume in such a system allows optical quantification of a transport process through the membrane. Therefore, our hybrid platform becomes interesting as an assay system and for fundamental biophysical studies.

We thus realized a stable hybrid flat platform that can now be used for further experiments aimed at the incorporation of the biomolecules in those membranes.

Acknowledgement

We acknowledge Ing. Robert Wijn from Lionix B.V. (Enschede, The Netherlands) for fabrication of Pyrex substrates, Huib van Vossen from the MESA⁺ Institute for Nanotechnology (Enschede, The Netherlands) who kindly provided the mask used to fabricate the Pyrex substrates, and Michel Duits from Physics of Complex Fluids (University of Twente, The Netherlands) who kindly provided the rotary evaporator apparatus.

References

- [1] M. Ichikawa and K. Yoshikawa, Optical transport of a single cell-sized liposome, *Applied Physics Letters*, 2001, **79**, 4598-4600.
- [2] A. Ashkin, Acceleration and Trapping of Particles by Radiation Pressure, *Physical Review Letters*, 1970, **24**, 156-159.
- [3] A. Ashkin, Optical trapping and manipulation of neutral particles using lasers, *Proc. Natl. Acad. Sci. USA*, 1997, **94**, 4853-4860.
- [4] P.A. Maia Neto and H.M. Nussenzveig, Theory of optical tweezers, *Europhysics Letters*, 2000, **50**, 702-708.
- [5] K. Svoboda and S.M. Block, Biological Applications of Optical Forces, *Annual Review of Biophysical and Biomolecular Structure*, 1994, **23**, 247-285.
- [6] K. Visscher, S.P. Gross, and S.M. Block, Construction of Multiple-Beam Optical Traps with Nanometer-Resolution Position Sensing, *IEEE Journal of Selected Topics in Quantum Electronics*, 1996, **2**, 1066-1076.
- [7] R.C. Weast, *Handbook of Chemistry and Physics*, 65th ed. (CRC press, Boca Raton, Fla., 1984-1985), pp. D-234.
- [8] T. Tlusty, A. Meller, and R. Bar-Ziv, Optical Gradient Forces of Strongly localized Fields, *Physical Review Letters*, 1998, **81**, 1738-1741.
- [9] A. Ashkin, Forces of a single-beam gradient laser trap on a dielectric sphere in the ray optics regime, *Biophysical Journal*, 1992, **61**, 569-582.
- [10] R.M. Simmons, J.T. Finer, S. Chu, and J.A. Spudich, Quantitative measurements of force and displacements using an optical trap, *Biophysical Journal*, 1996, **70**, 1813-1822.
- [11] W.S. Rasband, ImageJ, U.S. National Institute of Health, Bethesda, Maryland, USA, <http://rsb.info.nih.gov/ij/>, 1997-2007.
- [12] E. Reimhult, F. Höök, and B. Kasemo, Intact Vesicle Adsorption and Supported Biomembrane Formation from Vesicles in Solution: Influence of Surface Chemistry, Vesicle Size, Temperature, and Osmotic pressure, *Langmuir*, 2003, **19**, 1681-1691.
- [13] J.M. Johnson, T. Ha, S. Chu, and S.G. Boxer, Early Steps of Supported Bilayer Formation Probed by Single Vesicle Fluorescence Assay, *Biophysical Journal*, 2002, **83**, 3371-3379.
- [14] J. Schmidt, Stochastic sensors, *Journal of Materials Chemistry*, 2005, **15**, 831-840.
- [15] M. Mayer, J.K. Kriebel, M.T. Tosteson, and G.M. Whitesides, Microfabricated Teflon Membranes for Low-Noise Recordings of Ion Channels in Planar Lipid Bilayers, *Biophysical Journal*, 2003, **85**, 2684-2695.
- [16] M.C. Peterman, J.M. Ziebarth, O. Braha, H. Bayley, H.A. Fishman, and D.M. Bloom, Ion Channels and Lipid Bilayer Membranes Under High Potentials Using Microfabricated Apertures, *Biomedical Microdevices*, 2002, **4**, 231-236.
- [17] C. Schmidt, M. Mayer, and H. Vogel, A Chip-Based Biosensor for the Functional Analysis of Single Ion Channels, *Angew. Chem. Int. Ed.*, 2000, **39**, 3137-3140.
- [18] W. Hanke and W.-R. Schlue, *Planar Lipid Bilayers: Methods and Applications*, ed. D.B. Sattelle, Academic Press Limited, London, ISBN 0-12-322994-4, 1993.
- [19] W.A. Vercoutere, S. Winters-Hilt, V.S. DeGuzman, D. Deamer, S.E. Ridino, J.T. Rodgers, H.E. Olsen, A. Marziali, and M. Akeson, Discrimination among individual Watson-Crick base pairs at the termini of single DNA hairpin molecules, *Nucleic Acids Research*, 2003, **31**, 1311-1318.

- [20] D.W. Deamer and D. Branton, Characterization of Nucleic Acids by Nanopore Analysis, *Accounts of Chemical Research*, 2002, **35**, 817-825.
- [21] J. Nakane, M. Wiggin, and A. Marziali, A Nanosensor for Transmembrane capture and Identification of Single Nucleic Acid Molecules, *Biophysical Journal*, 2004, **87**, 615-621.
- [22] L.-Q. Gu, O. Braha, S. Conlan, S. Cheley, and H. Bayley, Stochastic sensing of organic analytes by a pore-forming protein containing a molecular adapter, *Nature*, 1999, **398**, 686-690.
- [23] J.J. Kasianowicz, E. Brandin, D. Branton, and D.W. Deamer, Characterization of individual polynucleotide molecules using a membrane channel, *Proc. Natl. Acad. Sci. USA*, 1996, **93**, 13770-13773.
- [24] A. Meller, L. Nivon, E. Brandin, J. Golovchenko, and D. Branton, Rapid nanopore discrimination between single polynucleotide molecules, *Proc. Natl. Acad. Sci. USA*, 2000, **97**, 1079-1084.
- [25] B. Baumeister, N. Sakai, and S. Matile, Giant artificial ion channels formed by self-assembled, cationic rigid-rod β -barrels, *Angew. Chem.*, 2000, **112**, 2031-2034.

CHAPTER FIVE

BIOFUNCTIONALIZED MEMBRANES ON FLAT SUBSTRATES

This chapter describes the successful introduction of the mechanosensitive channel of large conductance (MscL) protein into an artificial bilayer lipid membrane deposited onto an array of microholes in a flat glass substrate. We were able to visualize the transport of fluorescent molecules through this channel protein, and describe quantitatively the dynamics of passive diffusion of solutes through a single channel protein.

5.1 Introduction

Membrane proteins play a crucial role in cell activity. About 30-50% of the mass of the plasma cell membrane is lipid and most of the remainder comprises membrane proteins that constitute up to 70% of the membrane mass [1]. Some proteins are responsible for the transport of small molecules, electrons and ions across the membrane, and for signaling or triggering of events both inside and outside the cell. Many of these proteins perform an activity in response to an external stimulus such as electrical voltage [2,3], osmotic pressure [4,5], light [6], and mechanical stimuli [4].

Such selective activity is interesting in bioengineering for the construction of bionanodevices. Channel proteins can be used as a tool in drug delivery devices or in sensing. A widely studied protein is α -hemolysin [7]. This protein has been embedded in natural lipid [8] and artificial [9] membranes and has been used to study RNA and DNA. Moreover, selective channel activity is interesting from the point of view of the fundamentals of protein structure, activity, factors that trigger transport or protein conformational changes, manufacturing artificial nanochannels [10] or modifying them to show a specific functionality [11].

The mechanosensitive channel of large conductance (MscL), which is involved in the detection of osmotic stress in *Escherichia coli*, is especially interesting because modified mutants are available allowing protein opening and closing in a controllable manner. Also, MscL is stable against detergents [12] and temperature. In this chapter we report on the development of a novel hybrid flat platform that consists of microwells in a Pyrex substrate sealed by an artificial lipid membrane incorporating MscL proteins. MscL behaves as a natural nanovalve and enables the controlled load/release mechanism. We successfully studied diffusion through the protein that was triggered deliberately from outside the microwell. This is a closed system that allows access only from outside the microwell, in analogy with a cell where an activity is induced by applying an external stimulus. A schematic of the system is presented in Figure 5.1.

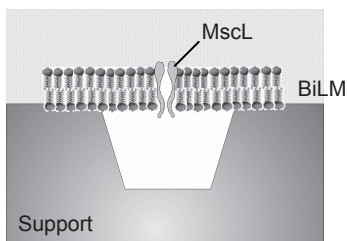


Figure 5.1. Schematic of a microwell in a Pyrex substrate sealed with a bilayer lipid membrane (BiLM) containing a MscL channel protein in the closed state.

5.2 MscL channel protein

The mechanosensitive channel of large conductance (MscL) from *Escherichia coli* has been extensively studied. It converts mechanical forces into electrical and chemical signals in the cell, in this way acting as a primary cellular mechano-transducer [13,14]. The protein is a homopentamer of five identical subunits, each 136 amino acids long and having two transmembrane helices (M1 and M2) per subunit. A schematic of MscL channel protein, showing also the orientation in the membrane, is presented in Figure 5.2. In the closed state, the five M1 helices that are tightly packed form the main gate of the channel (4 Å diameter pore) that is highly hydrophobic, while the hydrophobic M2 helices positioned on the periphery of the barrel face the lipid medium. The protein is embedded in the inner membrane of bacteria. In nature, the protein responds to the tension of the membrane created by osmotic shocks. As a result, the channel opens into a 3 nm pore [13] that allows molecular exchange (ions, solutes, and small proteins) between the interior and the exterior of the cell in order to equilibrate or minimize the osmotic differences and thus prevent cell lysis. The channel opens and closes continuously, resembling a nanovalve.

The opening of such a nanovalve in the absence of tension forces has been realized by introducing a charge covalently bound in the restriction region that causes the conformational changes of the protein [15]. This is due to the sensitivity of such a natural channel to the polarity of its hydrophobic narrow constriction region. In G22C MscL, the glycine residue has been replaced by a cysteine residue, providing a unique sulfhydryl group on each of the identical five subunits in the channel [15]. The introduction of charged or polar amino acids, or other charged compounds into the 22nd amino acid position of MscL causes opening of the channel in the absence of tension. Chemical modulators have been developed, including sulfhydryl-reactive molecules covalently attached to the engineered cysteine to enable triggering of charge-induced channel opening by pH [16]. Furthermore, photosensitive actuators coupled to the cysteine in this charge-sensitive part of the channel enable the gating of MscL by light [11].

In this chapter, we will use the functionality of engineered MscL proteins for the controlled loading/release mechanism of our device. The channel can be opened by adding [2-(trimethylammonio)ethyl]methanethiosulfonate (MTSET), which

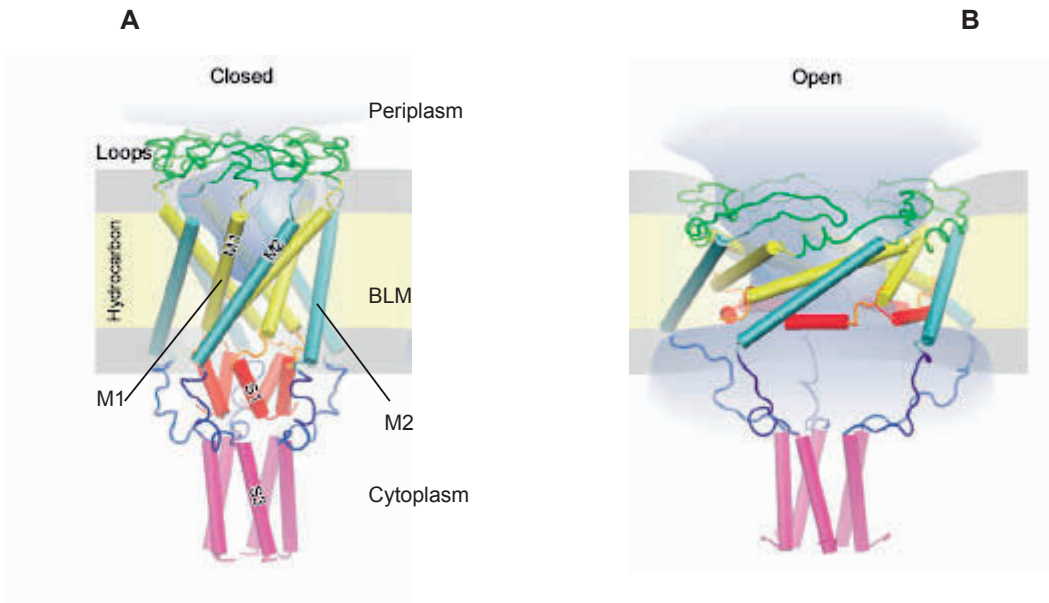


Figure 5.2. Conformational transitions of *Escherichia coli* MscL channel protein built by homology to the crystal structure of *Mycobacterium tuberculosis* MscL. Side view of MscL channel protein is depicted in its (A) closed and (B) open conformation. The M1 helices (yellow) form the main hydrophobic core of the channel and the hydrophobic M2 helices (blue) are positioned at the periphery of the barrel. The N-terminal domains presented from S1 α -helices (red) form an additional cytoplasmic gate and cytoplasmic domains (S3, purple) make a pre-filter. The light blue surface represents the water-filled volume in the pore. Reproduced with permission from [13]. Copyright Elsevier (2004).

results in five positive charges in the constriction region of the channel [15,16]. Previous work has shown that the residue G22C is accessible to MTSET from the periplasmic side (see Figure 5.2) even when the channel is closed and in the absence of tension [15]. In contrast, the residue 22 is not accessible to MTSET from the cytoplasmic side when the gate is closed. Therefore, activity of a single protein is dependent on which side the MTSET is added. In vesicles, however, the orientation of MscL proteins within the membrane is random (that is, it has no preferred orientation). This also holds for flat membranes obtained by vesicle collapse. Once a channel inserted in the proper orientation is activated, the

MTSET that diffuses through the channel could potentially induce an activation of the other channels inserted in the reversed orientation, although there is no experimental evidence that this will occur. If only one MscL protein is present and oriented in the wrong way, it will not be possible to open the channel by MTSET.

5.3 Theory: Passive diffusion through a nanopore

We derive a theoretical model that describes the release/loading of small molecules through a nanopore protein.

When a solute is introduced in a solution, mass transfer will occur from the region of high concentration towards the region of lower concentration, until equilibrium is reached. This diffusion can be represented by a basic equation, Fick's law [17,18], as shown below:

$$J = -D \frac{\partial C}{\partial x} \quad [5.1]$$

where J is the mass flux, D is the diffusion coefficient, C is the concentration of the solute, and x refers to the spatial coordinate.

We will use Eq. 5.1 to describe the loading of the microwell (see Figure 5.3) through a single MscL protein. In the case of a microwell of volume V , separated from the bulk medium by a thin wall that contains a single nanometer scale hole with a cross section S and length d , the diffusion of the solutes into the microwell depends on the diffusion through the hole (see Figure 5.3), for which the flux as a function of time is presented below:

$$J(t) = -D \frac{C(t) - C_b}{d} \quad [5.2]$$

where C_b refers to the concentration of the bulk solutes and $C(t)$ is the concentration inside the microwell at time t where we assume the concentration in the microwell to be homogeneous. Taking into account that the volume of the hole is much smaller than that of the bulk, the bulk concentration can be assumed constant. The concentration in the microwell as function of time can be expressed as:

$$\frac{\partial C(t)}{\partial t} = J(t) \frac{S}{V} \quad [5.3]$$

Solving Eq. 5.3 using Eq. 5.2 and by considering the boundary conditions ($C(t = 0) = 0$) gives:

$$C(t) = \left[1 - e^{-D \frac{St}{dV}} \right] C_b \quad [5.4]$$

Considering the fact that a single MscL channel resembles a nanovalve that opens and closes repeatedly, a factor γ_{on} that describes the fraction of time during which a channel remains open, is introduced. In case of n nanopores embedded in the membrane, Eq. 5.4 is modified as shown below:

$$C(t) = \left[1 - e^{-D \frac{nS\gamma_{on}t}{dV}} \right] C_b \quad [5.5]$$

Here we assume that the switching on and off time intervals are much smaller than the time constant defined in Eq. 5.7.

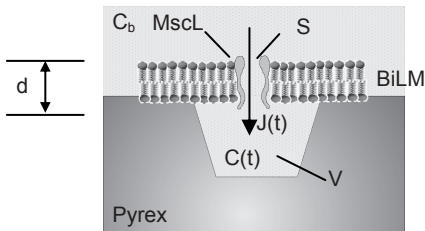


Figure 5.3. A sealed microwell with a lipid bilayer membrane (BiLM) containing a MscL channel protein in the open state, resulting in the diffusion of a solute into the microwell through the channel.

Eq. 5.5 can be written in a more general form as:

$$C(t) = \left[1 - e^{-\frac{t}{\tau}} \right] C_b \quad [5.6]$$

with the time constant τ given by:

$$\tau = \frac{dV}{DnS\gamma_{on}} \quad [5.7]$$

We now calculate the change in the concentration as function of time for diffusion through a MscL protein channel (see the schematics in Figure 5.3) based on Eq. 5.5 using the following parameters: $D = 3.3 \times 10^{-10} \text{ m}^2/\text{s}$ (calcein fluorophore in PBS buffer solution [19]), $d = 8.5 \text{ nm}$ [20], $S = 7.1 \times 10^{-18} \text{ m}^2$ (corresponding to a pore diameter of 3 nm of MscL protein), $V = 1.5 \times 10^{-17} \text{ m}^3$. These numbers correspond to the experiments described in section 5.4.

Figure 5.4 shows $C(t)$ for different values of n and γ_{on} . The diffusion takes place on a time scale of several hundreds of seconds for $n\gamma_{on} < 1$, allowing monitoring by fluorescence microscopy. Furthermore, measuring $C(t)$ provides quantitative information on $n\gamma_{on}$ since all other parameters in Eq. 5.6 and 5.7 are known. Also, considering a single pore that acts as a valve, the diffusion slows down when γ_{on} decreases, yielding an increase of τ . For example, when $n = 1$ and $\gamma_{on} = 1$, $\tau = 250 \text{ s}$. When γ_{on} decreases to 0.5 and 0.25, τ increases to ~ 500 and 1000 s , respectively.

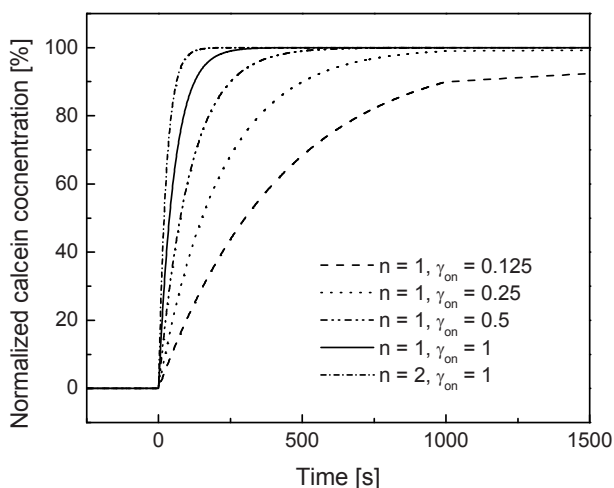


Figure 5.4. Theoretical time course of Calcein concentration in a microwell due to diffusion through a MscL channel. Different curves show results for different values of γ_{on} and n (see legend). The solute concentration inside the microwell is normalized with the bulk concentration.

Additionally, the same model as the one used above was evaluated using numerical calculations using a finite element method. The simulation was performed using FEMLAB from Comsol AB. Results showed only minor differences (see Figure 5.9) with the results obtained using Eq. 5.6 justifying the assumptions made in deriving the analytical expressions.

5.4 Materials and methods

Materials

Phosphatidylcholine (DPhPC, 1,2-Diphytanoyl-sn-Glycero-3-Phosphocholine) and POPG (PG, 1-Palmitoyl-2-Oleoyl-sn-Glycero-3-[Phospho-rac-(1-glycerol)], Sodium salt) were purchased from Avanti polar lipids (Alabaster, USA). Cholesterol (3 β -Hydroxy-5-cholestene, C₂₇H₄₆O), DTT (DL-Dithiothreitol), and DiA (3,3'-Dioctadecyloxycarbocyanine perchlorate, C₅₃H₈₅ClN₂O₆) were obtained from Sigma (Zwijndrecht, The Netherlands). MTSET ([2-(trimethylammonio)ethyl]methanethiosulfonate, Anatrace, Inc., Maumee, OH, USA) and bio-beads (Bio-Beads SM-2 adsorbents, Bio-Rad Laboratories B.V., Veenendaal, The Netherlands) were a kind gift from Dr. Armağan Koçer (Biomade Institute, Groningen, The Netherlands). PD10 desalting columns were purchased from Amersham Biosciences (Roosendaal, The Netherlands). Glucose (D(+)-Glucose) and chloroform were obtained from Merck (Darmstadt, Germany). Parafilm (Parafilm M) was purchased from Alcan Packaging (Zutphen, The Netherlands).

Giant unilamellar vesicles containing MscL

Detergent mediated reconstitution. Vesicle composition was based on the best results we obtained for flat membranes (see Chapter 4). The lipid mixture (DPhPC:POPG:cholesterol of ratio 70:25:5 by weight, respectively) was dissolved in chloroform and put into a round bottom flask. A thin lipid film was obtained on the glass walls by evaporating the chloroform in a rotary evaporator under vacuum while rotating the flask with the maximum speed at room temperature for 30 min. The dried film was swelled to form vesicles by adding 2 mM MOPS-Tris buffer (pH 7) such that lipid concentration in the bulk becomes 20 mg/ml. Next, freeze-thaw method was applied to the vesicle solution, repeating the cycle 5 times (-196 °C and 50 °C). Resulting giant lipid vesicles were extruded through a 400 nm pore size polycarbonate filter. MscL channel proteins were incorporated in the vesicles using a detergent-mediated reconstitution method [21,22]. Briefly, the extruded vesicles were titrated with oxidant free Triton X100 detergent (10% stock, 155 mM) by adding 37.5 μ l detergent into 300 μ l lipid solution. 220 μ l of MscL protein stock solution (concentration of 0.18 mg/ml) was added to the detergent-saturated vesicle solution and was incubated for 30 minutes at 50 °C. Later, glucose solution in PBS was added in the mixture to a final concentration of 400 mM. Next, 200 mg wet weight of biobeads were added into the mixture and incubated in a rotary mixer for 4 hours at room temperature. By removing the biobeads, the detergent was removed from the solution, resulting in vesicle reformation containing MscL protein, i.e. proteovesicles.

Electroformation of GUV. Another way to form giant vesicles containing MscL is by using the electroformation method [23]. The previously prepared proteovesicle solution was diluted to a lipid concentration of 0.8 mg/ml in 2 mM MOPS-Tris buffer (pH 7). A thin lipid film was obtained by covering surfaces of conductive glass slides (ITO) with 2 μ l droplets of proteovesicles close to each other followed by partially dehydrating the buffer under vacuum in a vacuum desiccator for overnight at 4 °C. After the proteovesicle films are obtained, an electroformation cell was prepared. A 2-mm Teflon ring was waxed on both top and bottom face. One of the prepared ITO slides is placed on a home made holder and the Teflon ring is fixed to it. A buffer containing 300 mM glucose in 1 mM MOPS-Tris buffer pH 7.0 supplemented with 1 mM MgCl₂ is added into this chamber. The second ITO glass was closed on top of this unit carefully in order not to introduce any air bubbles in such a way that its lipid film side faced the buffer. ITO glasses were connected to copper electrodes and the whole cell unit is fixed with screws. An AC voltage was applied for 4 hours across the cell unit with stepwise increases from 0.1 to 1.1 V at 12 kHz frequency). At the end, in order to detach glass attached GUVs, the AC current was lowered to 4 Hz and voltage was raised to 2 V for 30 min. Vesicles formed in this way had a diameter ranging from a few micrometers to 15 μ m. These vesicles were well separated from each other.

Proteomembrane deposition onto a microhole

A Pyrex substrate of thickness 150-170 μ m containing microwells with a hole diameter of a few micrometers and depth of \sim 4.5 μ m was prepared using Reactive Ion Etching (see Chapter 4). A polystyrene cuvette, containing small compartments of \sim 0.8 ml (Lab-Tek™ Chambered Coverglass, VWR International B.V., Amsterdam, NL), was mounted on top of the Pyrex substrate using parafilm. The surface of the Pyrex was incubated with 0.01% PLL in PBS for about 3 hours at 4 °C. The PLL was rinsed with buffer and glucose-loaded proteovesicles containing MscL were added. Proteovesicles were labeled with DiA fluorophore by adding \sim 1 μ l of 400 μ g/ml of DiA/methanol stock solution in 1 ml vesicle solution. Single proteovesicles were trapped using optical tweezers and visualized using epifluorescence microscopy. They were manipulated in the vicinity of the hole of interest. Their collapse was monitored using epifluorescence microscopy. Next, calcein was added to the solution to a final concentration of \sim 0.2 mM.

5.5 Results and discussion

Before proceeding with the Pyrex substrates, the functionality of the MscL was first assessed at the single vesicle level by observing the diffusion of a fluorescence probe through the MscL protein, yielding a fluorescence intensity

change inside the vesicle. One concern is the stability of the vesicle when MscL is incorporated. Another concern is the loss of lipid packing regularity at the boundary with MscL.

Here, giant proteovesicles supported on the sample surface were considered. The fluorescently labeled vesicles were imaged prior to (Figure 5.5.A and B) and after calcein addition in the bulk solution (Figure 5.5.C). Looking at the vesicle cross section image (Figure 5.5.C), no calcein was observed in the vesicle interior. The vesicle remained intact and no diffusion was observed through the proteovesicle wall prior to the channel activation. Upon adding MTSET to the bulk solution to activate the channel, an increase of the fluorescence intensity in the

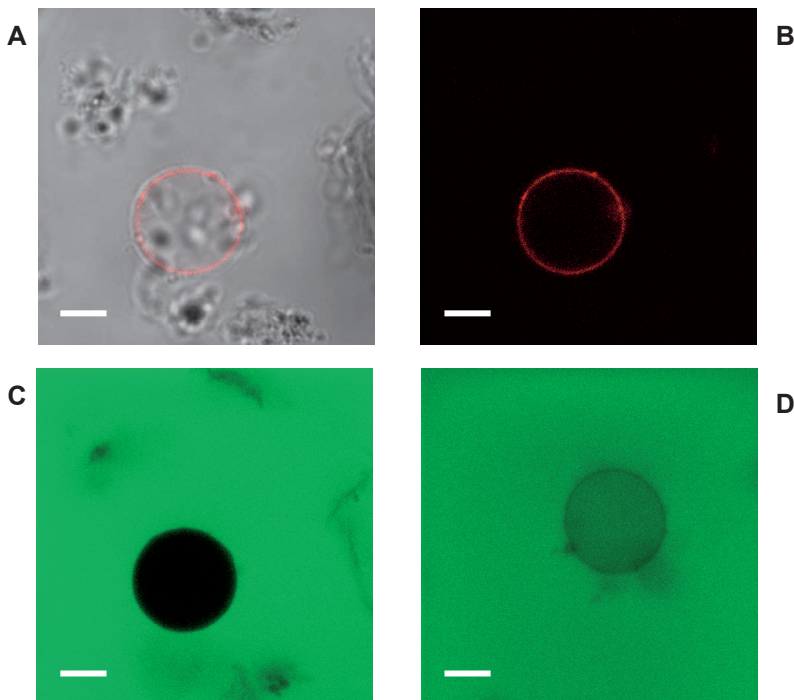


Figure 5.5. MscL functionality in a single vesicle visualized with CLSM. (A) Merge of white light and fluorescence image of the cross section of a single intact giant unilamellar vesicle containing MscL channel proteins. The vesicle was positioned at the bottom of the cuvette and labeled with DiA (red circle). (B) Fluorescence image as merge of the DiA fluorescence and calcein background fluorescence (no calcein was added yet). (C) Vesicle immersed in calcein (green color) prior to the channel activation. No dye was present in the vesicle. (D) Vesicle after activation of the MscL channel by addition of MTSET, resulting in dye diffusion into the vesicle. The scale bar is 5 μm .

interior of the vesicle was observed. A fluorescence image cross section of such a loaded vesicle is presented in Figure 5.5.D. This clearly demonstrates the diffusion of the calcein fluorophore into the vesicle through the activated MscL channels. Furthermore, the absence of Calcein in the vesicle prior to channel activation indicates the regularity of packed lipids in the vesicle wall, as well as the stability of the GUVs containing biomolecules.

Testing of the protein activity in vesicles was performed for each vesicle batch before applying them to the Pyrex sample by fluorescence efflux assay. To this end, first MscL was reconstitution into liposomes as explained before in the presence of a final concentration of 100 μ M calcein, a concentration at which calcein is self-quenching. The formed proteoliposomes were separated from the free calcein by performing a size exclusion chromatography. 5 μ l of proteoliposomes were added into 2 ml of buffer (10 mM sodium phosphate, pH 8, 150 mM NaCl, 1 mM EDTA) in a 4 ml cuvette and placed in a fluorometer and fluorescence was monitored at 520 nm (excitation at 490 nm). When channels were closed, there was a background fluorescence. However if channels were activated by the addition of MTSET, calcein was released from the vesicle interior and the resulting concentration decrease and dequenching upon entering the surrounding buffer could be monitored as an increase in fluorescence. The fluorescence intensity increased rapidly after the MscL activation, reaching within

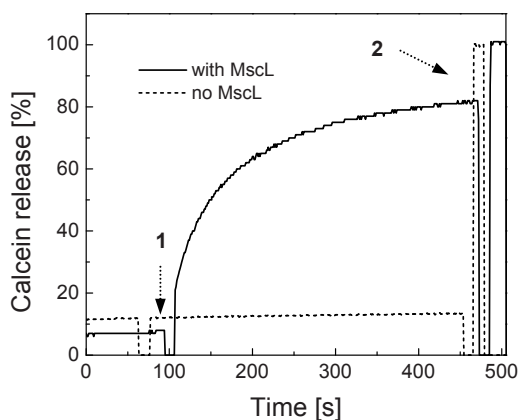


Figure 5.6. Fluorometric measurement of calcein efflux from giant lipid vesicles containing MscL channel proteins (solid line): (step 1) addition of MTSET in the bulk vesicle solution resulting in the release of calcein outside the vesicles due to opening of MscL channels, (step 2) addition of detergent in the vesicle bulk solution resulting in the vesicle burst. Dashed line presents efflux from vesicles without MscL proteins (control test).

the first minute ~ 50% of the final intensity plateau level after the vesicles were ruptured by adding Triton (see Figure 5.6). In these measurements, the concentration of MscL in the vesicles is random. Some vesicles may contain MscL while others do not have any protein. Therefore, the fluorometric efflux measurements represent an average activity.

Next, we proceeded with the Pyrex substrates containing microwells. Since we used holes with a size varying from 1 to several micrometers, giant vesicles having a diameter bigger than the hole size were required to efficiently collapse onto and seal the holes. We observed that the proteovesicle solution prepared with the detergent-mediated method had diameters ~ 1 - 2 μm and contained clustered vesicles. Although the same lipid composition (DPhPC:POPG:cholesterol of ratio 70:25:5 by weight) was used as in Chapter 4, where the hole sealing was optimal, the proteovesicle size and distribution appeared to be worse, resulting in clustered vesicles. This was mainly due to the use of additional components such as Triton detergent, biobeads, and MscL biomolecules during the vesicle preparation as compared to the procedure applied in Chapter 4. As a result, trapping with optical tweezers (see Chapter 3) and collapse of the proteovesicles on a surface in a controlled way was unsuccessful. To improve the efficiency and reproducibility of proteovesicle manipulation and collapse, additional treatment of the proteovesicle solution to increase the size and the vesicle distribution by using electroformation was implemented [23]. Vesicles formed in this way had a diameter ranging from a few micrometers to 15 μm . These vesicles were well separated from each other, enhancing the ability to manipulate and collapse vesicles using optical tweezers. Figure 5.7 shows a CLSM image of a membrane patch deposited on the Pyrex holes with diameter of 3 μm . Here, the membrane was labeled with DiA and immersed in buffer solution (PBS).

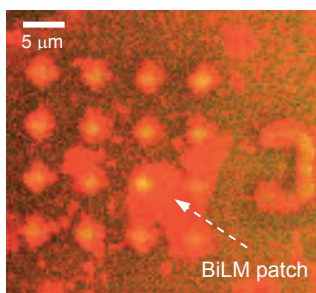


Figure 5.7. CLSM image of a membrane patch deposited on a 4×4 grid of 3 μm holes of the Pyrex substrate. The image is a merge of the fluorescence intensity obtained from the DiA (red color), staining the membrane only, and the fluorescence intensity from calcein added to the bulk solution (green color).

The collapsed giant vesicle was well spread over a wide region. Regions of stable membranes that were tightly sealing the holes were chosen to observe the dynamics of the diffusion through the MscL channel proteins. Water-soluble

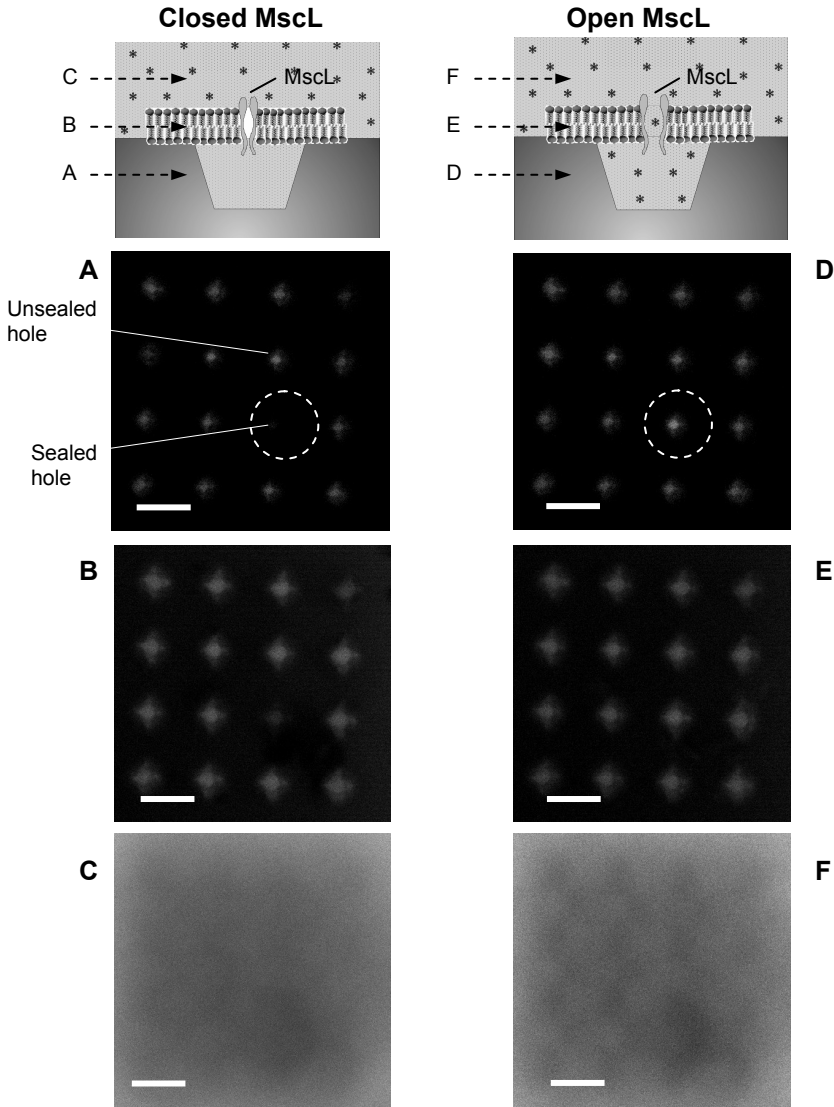


Figure 5.8. Schematic representation of a microwell in a Pyrex substrate, sealed with lipid membrane containing a MscL protein in the closed (top-left) and open (top-right) state. Horizontal arrows indicate the focus position for the CLSM images. 2D CLSM images of the Pyrex holes (diameter of 3 μm) covered with a lipid membrane where calcein was added in the bulk solution after sealing microwells. Images were obtained by focusing (A) inside the Pyrex wells, (B) on the Pyrex surface, and (C) in the bulk solution. CLSM images of the Pyrex wells in (A) loaded with calcein through the MscL channels after activating channel opening by adding MTSET (sealed holes presented in (A)). Images were obtained by focusing (D) inside the wells, (E) on the Pyrex surface, and (F) in the bulk solution. Holes of interest are enclosed by the dashed circle. The scale bar is 5 μm .

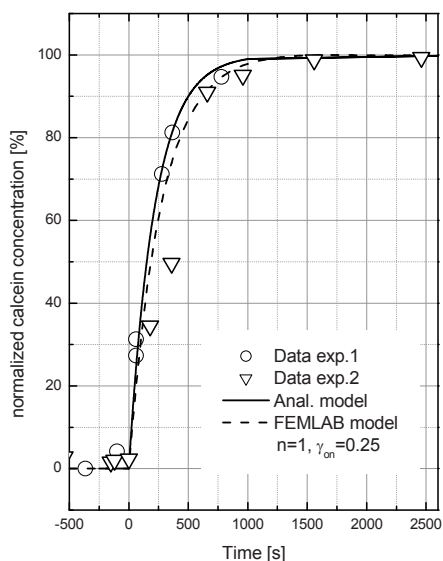


Figure 5.9. Dynamics of diffusion through the activated MscL channel proteins. MTSET was added at $t = 0$ s. (\circ) and (∇) are data points obtained experimentally for different samples. Dash line is obtained by simulating the diffusion through one MscL channel using FEMLAB software [24]. Solid line is derived from the diffusion equation (Eq. 5.5), considering a single MscL protein and a $\gamma_{on} = 0.25$. The calcein concentration inside the microwell is normalized to the bulk concentration.

calcein was added to the bulk solution. We then performed a Z-stack imaging and chose wells where no dye had diffused inside, indicating holes sealed with the lipid membrane. Figures 5.8.A, B, and C show these CLSM fluorescence images at different focusing depths. There is a clear difference in the fluorescence intensity between holes not covered with lipid membrane, appearing as bright spots due to loading with calcein solution, and holes that were sealed, appearing as dark spots (Figure 5.8.A).

The MscL channel was then activated by adding 5 μ l of 80 mM MTSET ([2-(trimethylammonio)ethyl]methanethiosulfonate) solution (dissolved in PBS) in \sim 400 μ l bulk medium. Depth profiles of the fluorescence intensity inside the sealed microwell were recorded in time to follow the dynamics of the dye diffusion into the microwell through the activated MscL channel, as shown in Figures 5.8.D, E, and F where images were taken 15 minutes after activating the channel opening. The imaging focus inside the microwell was \sim 2 μ m below the Pyrex surface (see Figure 5.8.D). The intensity inside the microwell increased as function of time, as expected (see Figure 5.9).

Figure 5.9 shows the representative data of the normalized fluorescence intensity in the microwell measured at different times prior to and after MscL channel

activation. When the channel was not activated, the intensity in the microwell was ~ 0 . The clear intensity increase after adding MTSET obviously indicates the passive dye diffusion into the microwell due to the opening of MscL channels. The intensity increased rapidly to about 50% of the final saturation value in the first 3 minutes after the channel was activated. In most cases the saturation value was ~ 80 -90% of the bulk intensity. An average time constant $\tau \sim 1000$ s was found. Compared to the bulk data shown in Figure 5.6, here the diffusion process is slower, which may be attributed to the lower number of MscL channels in the membrane patch.

The loading dynamics achieved for different sealed holes at different samples showed remarkably similar behavior, as shown in Figure 5.9, demonstrating the reproducibility of the experiment. The experimental data were curve fitted using the expression for $C(t)$ (Eq. 5.5), considering the actual experimental conditions, i.e. $D = 3.3 \times 10^{-10}$ m²/s, $d = 8.5$ nm, $S = 7.1 \times 10^{-18}$ m² (pore diameter of MscL protein of 3 nm), and $V = 1.5 \times 10^{-17}$ m³. Curve fitting of the measured data yielded $n\gamma_{on} = 0.25$. These results were confirmed by the results obtained by the simulations with FEMLAB, performed for the same experimental conditions.

The observed value of $n\gamma_{on}$ can be obtained for different values of n and γ_{on} as presented in Table 5.1.

Table 5.1. Probable combinations of n and γ_{on} yielding a factor $n\gamma_{on} = 0.25$.

$n\gamma_{on} = 0.25$	
n	γ_{on}
1	0.25
2	0.125
3	0.08
4	0.06

MscL can open as an iris of a variable diameter that opens and closes rapidly [13]. The protein stays open for a considerable time interval during a cycle. Therefore values of γ_{on} of 0.125 (indicating that the molecule stays open $\sim 12\%$ of the time) and smaller are less probable in our case. In addition, we can compare our results with electrophysiological data. In Figure 5.10, a representative patch clamping trace (solid black line) measured after charge-induced activation of the MscL channel opening is presented (courtesy of Armağan Koçer, BioMade Technology Foundation, Groningen, The Netherlands). The trace measures the ion flow through a single open MscL channel. The variations in the current represent opening and closing events of the channel. If the channel stays constantly open, the behavior could be modeled with a constant output current, as presented in Figure 5.10 by the dashed line. The step current after subtracting the

background (gray line in Figure 5.10) for a completely open channel should be ~ 60 pA, which for an applied voltage of 20 mV corresponds to a conductance of 3 nS, as known from literature [11]. Next we calculated the fraction of time the channel stayed open for a single channel in the case of patch measurements γ_{on}^{patch} . γ_{on}^{patch} can be calculated as the ratio of the integrated area under the patch curve (A_{patch}) divided by the area under the modeled curve (A_{model}) after subtracting the background area. The integration yielded a corrected A_{patch} and A_{model} of 12 pA·s and 55 pA·s, respectively. Hence, we found a $\gamma_{on}^{patch} \sim 0.21$, in close agreement with the value of γ_{on} we determined from our experiments ($\gamma_{on} = 0.25$). It should be noted that the time trace used here is relatively short compared to the on and off times. Also the choice of the current step of 60 pA can be debated, although small changes in this value only cause modest changes in the predicted γ_{on} (for a step current of 50 to 70 pA γ_{on}^{patch} varies from 0.32 to 0.21). Clearly for a more accurate estimation of γ_{on} better statistics are required.

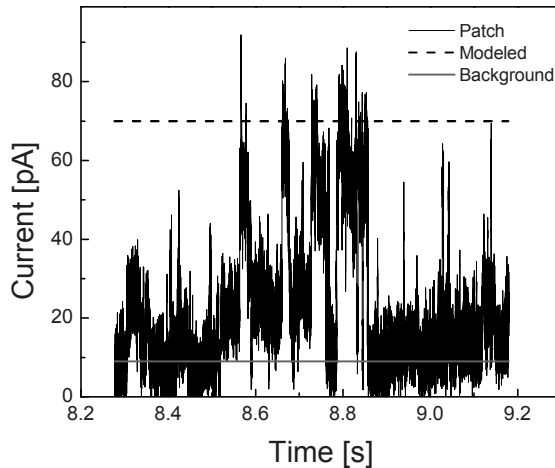
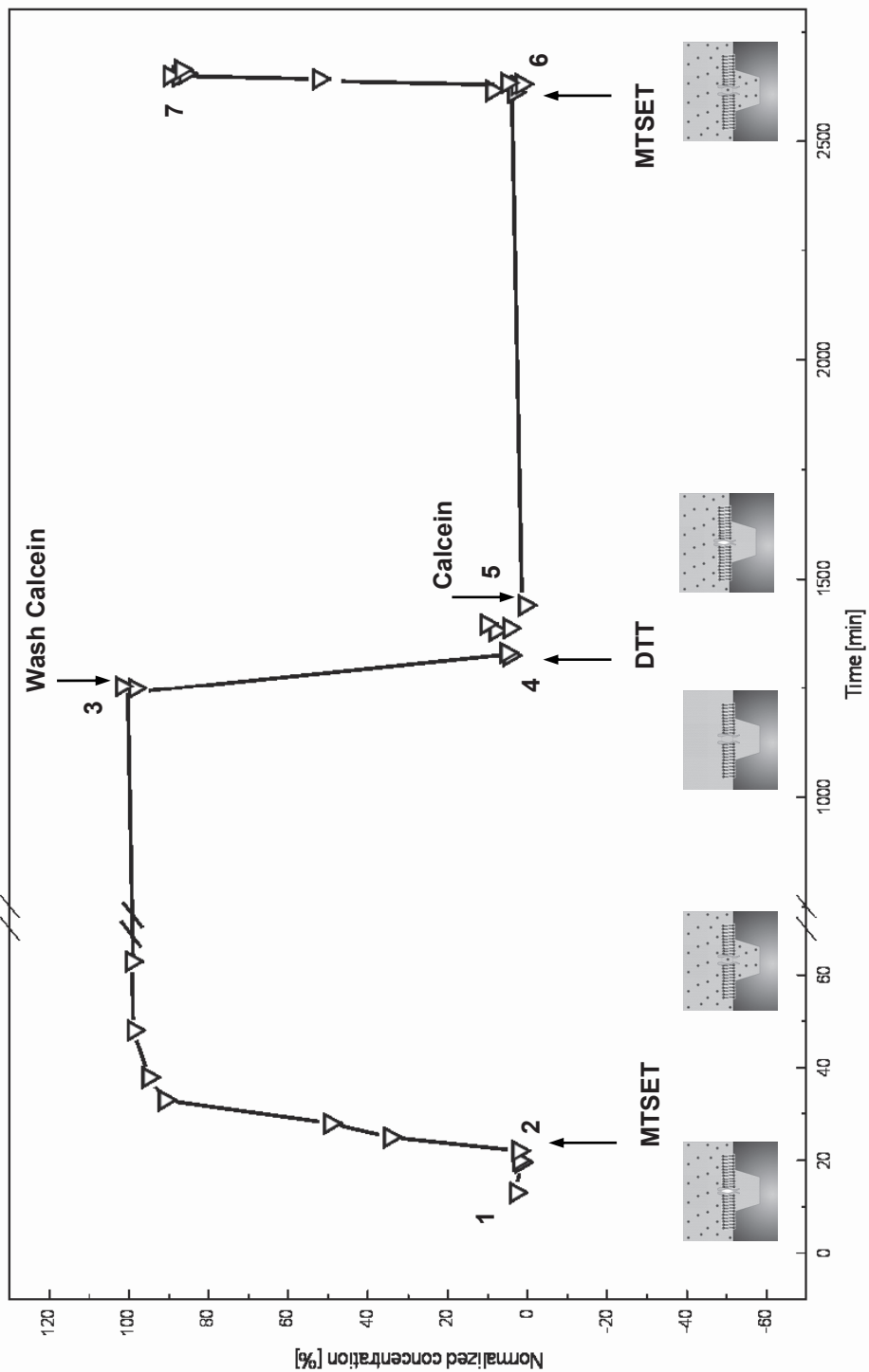


Figure 5.10. Diffusion through MscL in the presence of an external electrical field. Patch clamping trace (solid line) measured after charge-induced activation of a single MscL channel opening. Input voltage was ~ 20 mV. Modeled trace (dashed line) is for a channel that stays constantly open.

Nevertheless, this analysis suggests that we most likely have a single functioning MscL channel protein inserted in our artificial membrane. MscL functionality was initiated in a controlled manner by adding MTSET resulting in the opening of the channel in the absence of tension forces.

As a next step, the MscL activity was switched on- and off by activating- and deactivating the protein functionality upon addition of MTSET and DTT



respectively, as presented in Figure 5.11. The sealed microwell with a lipid membrane containing MscL was incubated in aqueous calcein solution. No diffusion of calcein through the proteomembrane inside the microwell was observed (step 1). The MscL activity was initiated by adding MTSET (step 2) which was accompanied with a fast diffusion of calcein through the MscL channel. The level of calcein in the microwell remained stable, meaning that the refreshment of the solute was facilitated by the channel that remained active. After one day the calcein was washed (step 3) from the cuvette using a flow system. While the nonsealed microwells were totally washed, a low calcein intensity was still present in the sealed microwell (see Figure 5.12) which reached the background level in less than 10 min. The sample was then washed with a DTT (DL-Dithiothreitol) solution to break the disulfide bonds between MscL and MTSET, thereby deactivating the MscL (step 4). After incubation with DTT for ~ 10-15 min the system was washed with buffer and calcein was added again in the bulk medium (step 5). No calcein diffusion into the sealed microwell was observed, indicating that the MscL channel was deactivated. Finally, on the third day, MscL activity was restored again by adding MTSET in the bulk solution (step 6), resulting in a fast diffusion of calcein into the microwell (step 7), as shown in

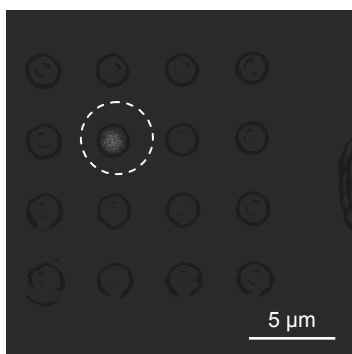


Figure 5.12. Pattern of microwells after washing the calcein from the bulk solution (between step 3 and 4 in Figure 5.11). The image is a merge of CLSM fluorescence with the white light image. The sealed microwell (bright spot) is indicated within the dashed ring, still showing fluorescence intensity from the calcein entrapped inside while the other microwells were totally washed (dark spots).

Figure 5.11 (facing page). Cyclic induced activity of the MscL channel protein. Normalized calcein concentration inside a Pyrex microwell sealed with a lipid membrane containing MscL during several steps. (1) Incubation in calcein bulk solution. (2) Initiation of MscL activity by adding MTSET in the bulk. (3) Calcein was washed from the cuvette by rinsing with buffer. (4) MscL activity was stopped by applying DTT solution in the cuvette. Finally, DTT was rinsed with buffer. (5) Addition of calcein in the bulk solution. The hole remained sealed. (6) Addition of MTSET to reactivate the MscL functionality. (7) Calcein diffusion inside the microwell via the re-activated MscL channel. Note the different time scales in the X-axis.

Figure 5.11.

This measurement demonstrates controlled loading into and release from the microwell through the nanovalve in a cyclic fashion by controlled switching of the MscL activity. Furthermore, these experiments show the excellent stability of the functional system. The proteomembrane remains stable and the biomolecule retained its activity in our artificial system for several days.

5.6 Conclusions

In this chapter, we have demonstrated the proof-of-principle of a novel hybrid system where in-vitro functionality of what is most likely a single MscL protein incorporated in an artificial bilayer lipid membrane sealing a microwell was observed.

We successfully demonstrated the functionality of the MscL channel protein incorporated in the membrane that seals the Pyrex microwell. We were able to deliberately trigger the functionality of the MscL proteins, inducing a controlled loading/release through the natural nano-valve. These are the first experiments to include a protein in such synthetic structures and demonstrate controlled release through a protein nanovalve in a remarkably stable proteomembrane.

The dynamics of calcein diffusion through the MscL channel from the bulk into the microwell was monitored with fluorescence microscopy. The measurements demonstrated rapid dye diffusion with a time constant $\tau \sim 1000$ s. The curve fitting of the experimental CLSM data with an analytical diffusion model as well as with a FEMLAB simulation model for diffusion by implementing the real experimental conditions yielded a $n_{\gamma_{on}} = 0.25$, indicating that the diffusion most probably occurred through a single MscL channel protein. Interestingly, the MscL channels appear to allow passive diffusion for about 25% of the time interval.

We were able to control the activity of MscL over several days, by switching it on- and off in a cyclic fashion, a property relevant for controlled drug delivery in nanodevices. Because of the high stability and controlled functionality, it opens new perspectives for other applications such as assay sensing systems. Such a system could also be used for fundamental purposes to study the properties of the biomolecules and their behavior, e.g. by observing at the diffusion through the membrane caused due to the conformational changes of the protein induced by an external stimulus.

So far, several studies on MscL single molecule activity were performed using mainly electrophysiological methods [11,14,16,25] and fluorometric efflux measurement. In the case of electrophysiological measurements, the measurement of ionic transport through the MscL is an active transport defined from the external applied field. In addition, the rapid opening and closing rate of the biomolecule induces limitations in real time screening of intermediate steps of

the biomolecule functionality. The fluorometric measurements rely on passive transport and give information on the bulk activity. In our system, we can obtain quantitative information about functionality of single biomolecules and monitor the passive transport kinetics in real time. The diffusion experiments also indicate that the biomolecule does not permit ion passage continuously, indicated by the factor $\gamma_{on} \sim 0.25$. Although there are hypotheses that the protein opens as an iris of variable diameter [13], no experimental evidence is available for single cyclic functionality.

The linking of biophysics and nanofabrication allows biomolecular manipulation to study dynamic transport processes at the single molecule level. The results achieved here are unique and is a major first step towards a biohybrid spherical vehicle as a movable nanocontainer with tunable functionality, where the activity can be triggered from outside the vehicle. In the next two chapters we focus on the development of self-standing spherical hybrid vehicles by implementing the method developed here.

Acknowledgement

We acknowledge the support of Dr. Armağan Koçer from BioMade Technology Foundation (Groningen, The Netherlands) who kindly prepared the giant vesicles containing MscL proteins, performed efflux fluorometric tests, and provided the patch-clamp trace in the framework of a collaboration.

References

- [1] M.K. Jain, *Introduction to Biological Membranes*, 2nd edition, ed. 'A Wiley-Interscience publication', USA, ISBN 0-471-84471-3, 1988.
- [2] M. Sondermann, M. George, N. Fertig, and J.C. Behrends, High-resolution electrophysiology on a chip: Transient dynamics of alamethicin channel formation, *Biochimica et Biophysica Acta*, 2006, **1758**, 545-551.
- [3] V. Borisenko, T. Loughheed, J. Hesse, E. Füreder-Kitzmüller, N. Fertig, J.C. Behrends, G.A. Woolley, and G.J. Schütz, Simultaneous Optical and Electrical Recording of Single Gramicidin Channels, *Biophysical Journal*, 2003, **84**, 612-622.
- [4] C. Kung and P. Blount, Channels in microbes: so many holes to fill, *Molecular Microbiology*, 2004, **53**, 373-380.
- [5] A. Burykin and A. Warshel, *Biophysical Journal*, 2003, **85**, 3696-3706.
- [6] J.P. Allen, G. Feher, T.O. Yeates, H. Komiya, and D.C. Rees, Structure of the reaction center from *Rhodobacter sphaeroides* R26: The protein subunits, *Proc. Natl. Acad. Sci. USA*, 1987, **84**, 6162-6166.
- [7] F.M. Goñi and H. Ostolaza, *E. coli* α -hemolysin: a membrane-active protein toxin, *Brazilian Journal of Medical and Biological Research*, 1998, **31**, 1019-1034.

- [8] M. Akeson, D. Branton, J.J. Kasianowicz, E. Brandin, and D.W. Deamer, Microsecond Time-Scale Discrimination Among Polycytidylic Acid, Polyadenylic Acid, and Polyuridylic Acid as Homopolymers or as Segments Within Single RNA Molecules, *Biophysical Journal*, 1999, **77**, 3227-3233.
- [9] J. Schmidt, Stochastic sensors, *Journal of Materials Chemistry*, 2005, **15**, 831-840.
- [10] A. Aksimentiv, J.B. Heng, G. Timp, and K. Schulten, Microscopic Kinetics of DNA Translocation through the Synthetic Nanopores, *Biophysical Journal*, 2004, **87**, 2086-2097.
- [11] A. Koçer, M. Walko, W. Meijberg, and B.L. Feringa, A Light-Actuated Nanovalve Derived from a Channel Protein, *Science*, 2005, **309**, 755-758.
- [12] E. Perozo, Gating prokaryotic mechanosensitive channels, *Nature Reviews / Molecular Cell Biology*, 2006, **7**, 109-119.
- [13] S. Sukharev and A. Anishkin, Mechanosensitive channels: what can we learn from 'simple' model systems?, *TRENDS in Neurosciences*, 2004, **27**, 345-351.
- [14] S.I. Sukharev, P. Blount, B. Martinac, and C. Kung, Mechanosensitive Channels of *Escherichia coli*: The MscL Gene, Protein, and Activities, *Annu. Rev. Physiol.*, 1997, **59**, 633-657.
- [15] K. Yoshimura, A. Batiza, and C. Kung, Chemically Charging the Pore Constriction Opens the Mechanosensitive Channel MscL, *Biophysical Journal*, 2001, **80**, 2198-2206.
- [16] A. Koçer, M. Walko, E. Bulten, E. Halza, B.L. Feringa, and W. Meijberg, Rationally Designed Chemical Modulators Convert a Bacterial Channel Protein into a pH-Sensory Valve, *Angew. Chem. Int. Ed.*, 2006, **45**, 3126-3130.
- [17] H.C. Berg, *Random Walks in Biology*, Princeton University Press, New Jersey, USA, 1983, ISBN 0-691-08245-6.
- [18] P. Paradisi, R. Cesari, F. Mainardi, and F. Tampieri, The fractional Fick's law for non-local transport processes, *Physica A*, 2001, **293**, 130-142.
- [19] N. Yoshida, M. Tamura, and M. Kinjo, Fluorescence Correlation Spectroscopy: A New Tool for Probing the Microenvironment of the Internal Space of Organelles, *Single Molecules*, 2000, **1**, 279-283.
- [20] G. Chang, R.H. Spencer, A.T. Lee, M.T. Barclay, and D.C. Rees, Structure of the MscL Homolog from *Mycobacterium tuberculosis*: A Gated Mechanosensitive Ion Channel, *Science*, 1998, **282**, 2220-2226.
- [21] J-L. Rigaud, B. Pitard, and D. Levy, Reconstitution of membrane proteins into liposomes: application to energy-transducing membrane proteins, *Biochimica et Biophysica Acta*, 1995, **1231**, 223-246.
- [22] D. Lévy, A. Gulik, A. Bluzat, and J-L. Rigaud, Reconstitution of the sarcoplasmic reticulum Ca^{2+} -ATPase: mechanisms of membrane protein insertion into liposomes during reconstitution procedures involving the use of detergents, *Biochimica et Biophysica Acta*, 1992, **1107**, 283-298.
- [23] P. Girard, J. Pécréaux, G. Lenoir, P. Falson, J-L. Rigaud, and P. Bassereau, A new method for the Reconstitution of Membrane Proteins into Giant Unilamellar Vesicles, *Biophysical Journal*, 2004, **87**, 419-429.
- [24] FEMLAB software, COMSOL AB, Stockholm, Sweden, 2006, www.comsol.com.
- [25] P. Moe and P. Blount, Assessment of potential stimuli for mechano-dependent gating of MscL: Effects of pressure, tension and lipid headgroups, *Biochemistry*, 2005, **44**, 12239-12244.

CHAPTER SIX

DEVELOPMENT OF THE SCAFFOLD

This chapter describes the fabrication of sub-micron sized spherical polymeric and glass scaffolds containing nanoholes. The influence of process parameters on hole dimensions is explored.

6.1 Introduction

Previous chapters described hybrid systems based on Pyrex substrates containing arrays of micrometer size wells that were sealed with a bilayer lipid membrane in which biomolecules were incorporated. To further develop free-standing individual hybrid systems for drug delivery and sensing applications, we pursued the fabrication and characterization of spherical scaffolds. As described in Chapter 1, one of the basic features in the design is the hollow impermeable polymer scaffold with a single small hole through which a payload can be loaded into or released from the scaffold.

Here we present the development of polymeric scaffolds based on sub-micron hollow polystyrene beads using Focused Ion Beam drilling [1]. We also developed micron-sized scaffolds based on glass. Hollow glass scaffolds, commercially available in large volumes, may be interesting for studying single molecule processes where bleaching is less critical since the bead volume is bigger than the excitation volume. We also made flat polystyrene substrates containing arrays of microwells to obtain additional information about the etching rate of polystyrene and to explore the reproducibility of hole drilling with FIB, parameters relevant for automated fabrication of HPS scaffolds arranged on a predefined pattern.

6.2 Choice of the scaffold

The scaffold is an important component of the hybrid device we wish to develop. First we define a set of requirements for the scaffold compatible with the design presented in Chapter 1; these requirements dictate the choice of scaffold material.

As discussed in Chapter 1, different scaffold architectures have been developed for drug delivery vehicles (DDV). In our design, we have implemented a hollow structure as the basis of the DDV, resembling the cell membrane that encloses a certain volume. The advantage of such a scaffold is that more payload can be encapsulated inside the vehicle compared to other commonly-used scaffold types.

Scaffold material. For optimal in vivo performance, the scaffold material should be:

- water-insoluble, to provide structural stability and effective functionality inside the body.
- biocompatible, to prevent recognition by the host medium, thus enabling the intended specific functionality of the DDV.

- non-toxic, to avoid any injurious effect on cells.
- biodegradable with a desired degradation time, to enable excretion of the components of the DDV after it has completed its function.
- bioinert (surface) [2] to allow a long circulation time.
- impermeable, to prevent any undesired leak through the scaffold wall.

For such applications, organic materials such as polymers are preferable due to the ability to tailor their properties such as hydrophilicity, lifetime, and biocompatibility, to achieve the aforementioned properties.

Scaffold size. The requirement that the DDV has to circulate inside the body using the blood circulation imposes limitations on the size. The scaffold should be smaller than a few micrometers, that is, on the sub-cellular scale, in order to easily penetrate through the narrow blood vessels. Previous work on testing in-vitro DDV as 'smart injectable particulates' based on inorganic scaffolds have indicated that particles with size $< 5 \mu\text{m}$ can safely circulate through the vascular system [3]. Depending on the application, particles $< 200 \text{ nm}$ are preferred to reach the specific diseased sites. Smaller particles can traverse the endothelium of blood vessels in solid tumors and can extravasate into the interstitial spaces, resulting in a high accumulation [4].

Defined geometry and number of the holes. As presented in the design in Chapter 1, a hole in the scaffold will serve as the 'gate' that controls any exchange between the scaffold interior and the bulk. The hole is designed to be sealed by a lipid membrane in which biomolecules are embedded. Synthetic flat artificial bilayer lipid membranes or purified real cell membranes have the drawback of low stability. The reduction of the supporting hole area increases the membrane stability [5]. Therefore, hole dimensions in sub-micrometer range are preferred in our design. The membrane is the natural support for active molecules that enable DDV bioactivity. Single holes in the scaffold are preferred for ease of fabrication and to make the system less susceptible to leakage due to the membrane rupture.

The design thus calls for an impermeable and biocompatible polymeric scaffold with a diameter $< 5 \mu\text{m}$, containing a single hole with a size up to a few hundreds of nanometers. A polystyrene based scaffold fulfills the set of requirements, with the exception of biodegradability. We start with commercially available hollow polystyrene beads of $\sim 1 \mu\text{m}$ outer diameter.

6.3 Materials and methods

Sample preparations

Hollow polystyrene scaffolds. Commercially available hollow polystyrene (HPS) beads (Polysciences, Warrington, PA, USA), having an inner diameter of 800 nm and wall thickness of 100 nm, were used as scaffolds. These beads contain water inside and are suspended in water solution. The beads were further diluted with de-ionized water to a particle concentration of 10^7 beads/ml [6].

A modified optically transparent holder was prepared to support the polystyrene beads for the FIB experiment. Standard coverslip glasses (thickness of 170 μm and diameter of 30 mm, Menzel-Gläser, Braunschweig, Germany) were used, on which a very thin titanium layer (10 nm) was deposited using sputtering technique (Sputterke apparatus, MESA+, The Netherlands). The conductive layer was used to enable a charge flow and reduce the local sample surface charging that occurs during FIB processing. Due to the interaction between the ion beam and the charge accumulated on the surface, beam deflections may occur, causing spatial and temporal inaccuracy in the etching process.

To locate the fabricated beads for further optical observations, thin triangle-shaped markers were deposited on top of the sample using a micro patterned photo resist mask and standard electroplating methods [7,8].

The suspension of HPS beads was sonicated for a few minutes and a droplet of this solution was placed on the prepared support and left for more than 24 hours to dry at 26 °C. Optically separated beads were chosen for FIB processing (see Figure 6.1).

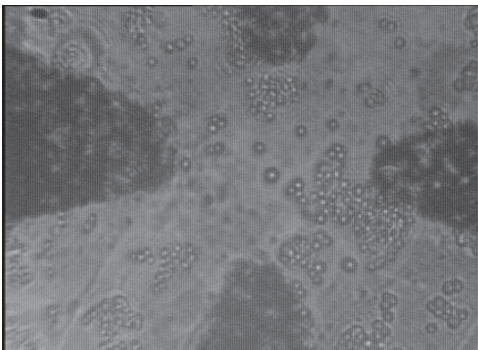


Figure 6.1. Pattern of dried polystyrene scaffolds on a metal-coated (Ti) coverslip glass with markers (black triangular shapes).

In addition to the Ti-coated samples, substrates coated with a 10 nm thick gold/palladium (Au/Pd content respectively 80/20) layer were prepared. Sputtering of the Au/Pd layer is done with a Polaron SEM coating system (a facility of MESA+ cleanroom) with pressure $\sim 8 \times 10^{-2}$ mbar and current ~ 6 mA. The gold layer deposited in this way does not adhere as well as the Ti layer.

However, gold coated samples show better optical transparency than the titanium coated substrates. Samples containing dried HPS beads supported on such gold-coated substrates were prepared in the same way as described above.

FIB processing

Experimental procedure. The prepared sample of dried HPS scaffolds was placed on a metal holder of the FIB machine and a silver layer or conductive tape was used to make the connection between the Ti-surface of the sample and the metal holder. Next, the sample was positioned in the working chamber of the FIB machine. A low current of gallium ions (the lowest settings: 1 pA and 1.5 pA respectively with the FEI FIB 200 [9] and FEI FIB Nova 600 NanoLab [10]) was used to achieve a low etching rate of the polystyrene material. The accelerated ion beam was focused on the bead surface, etching the material mechanically. The FIB was also used to image the beads before and after the etching process.

Determination of the etching time. The etching time of a single hole was determined by following the beam profile with the real time monitor, which indicates the actual 2D-profile of the etched region. A change in material type or a change in topology of the etched material causes a difference in the intensity of the emitted secondary electrons or ions. An alternative to real time monitoring is by using snap-shot imaging. Each time before a snap-shot image was made the etching process was stopped and continued after the scanning was finished. In this case, the etching of a feature was followed based on real-time images received from a very fast single scan. Yet, another way to monitor etching of the single hole of the scaffold is by following the current change recorded with an end-point detector. With such a method, the average brightness in the etching area is measured in real time, resulting in a typical end-point detection. Here, an insulator should appear of lower intensity than a conductor since the conductor has a higher secondary electron yield than the insulator. Attempts to follow the etching process of a single hole on the upper wall of the HPS scaffold with an end-point detector were not successful, since the current changes were not significant, even when penetrating the second wall of the bead and the metal layer. Fluctuations of the current were present during the whole etching process, making it difficult to predict the current increase due to the etching of the polystyrene material.

6.4 Results

Hollow polystyrene scaffolds with single holes. An image of a polystyrene scaffold into which a single hole was etched using a 1 pA gallium ion current is shown in Figure 6.2.A.

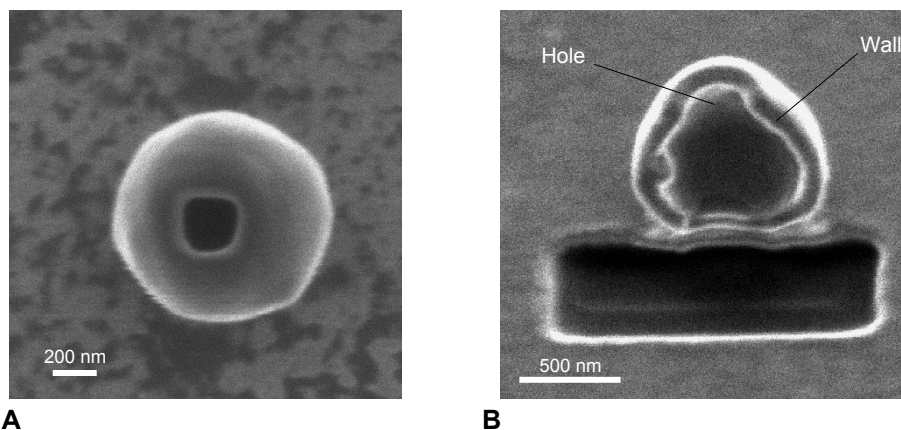


Figure 6.2. (A) FIB image of a dried HPS scaffold (outer diameter of 1 μm , wall thickness of 100 nm) with a hole of $250 \times 260 \text{ nm}^2$ in it. The hole was etched using a current of 1 pA. (B) FIB image of the HPS scaffold with a hole (see A), which is half etched and rotated.

The scaffold outer diameter is 1 μm . The dimensions of the hole are $250 \times 260 \text{ nm}^2$ and the time required to etch the hole through the 100 nm thick wall was ~ 17 sec. The etching was controllable with respect to the number of holes and the dimensions of the hole. The polystyrene scaffold remained stable while etching with FIB. Furthermore, the scaffold maintains its position on the sample, despite the local ionic charging of the polystyrene surface that occurs during the etching. To check the interior of the HPS scaffold structure after a hole was created, we removed one half of the bead by etching with the same current for about 93 seconds and imaging the scaffold at an angle, as presented in Figure 6.2.B. Clearly, the scaffold remained hollow and the hole exists only on the top of the scaffold, as intended. No structural damage to the scaffold, apart from the holes could be observed. It was also possible to fabricate polystyrene scaffolds with two holes without damaging the integrity of the structure (see Figure 6.3).

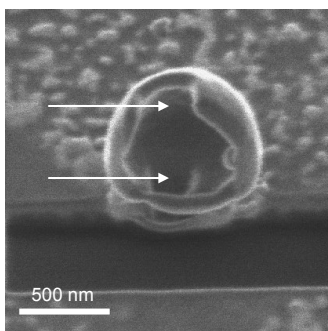


Figure 6.3. FIB image of a half HPS scaffold (outer diameter of $0.9 \mu\text{m}$) containing two holes (indicated by white arrows, hole dimensions are $200 \text{ nm} \times 200 \text{ nm}$).

Next, the dependency between the etching time and the hole surface area was measured. Also the smallest area holes that could be drilled using FIB were explored. In these experiments, the lowest FIB current (1.5 pA) was used. Figure 6.4 shows the required etching time as a function of the surface area of a single square hole.

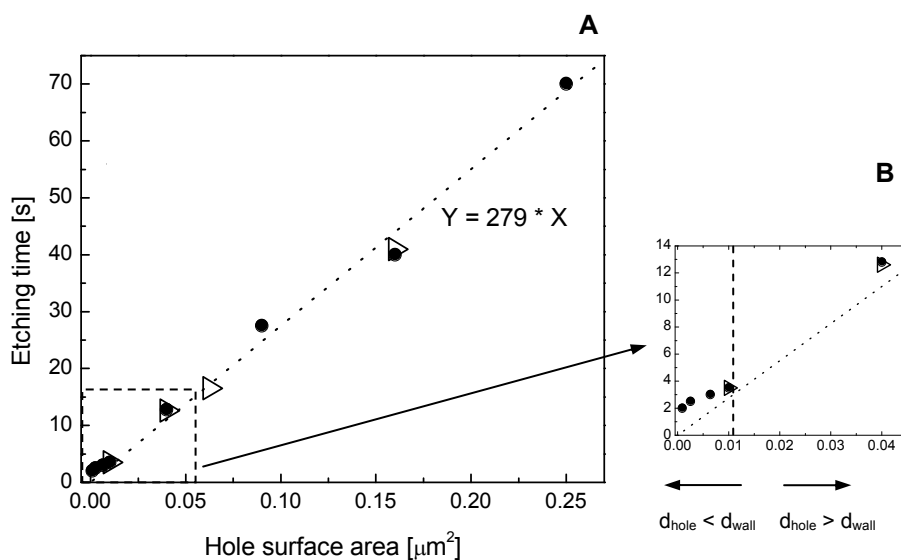


Figure 6.4. (A) Time required for etching of single square holes as function of the hole surface area: (●) shows the data obtained with FEI FIB Nova 600 nano lab using a minimum etching current of 1.5 pA and the dotted line is a linear fit of these data; (▷) shows the data obtained with FEI FIB 200 using a minimum etching current of 1 pA . (B) Zoom in of the graph in (A) for holes with a surface area starting from 30×30 to $200 \times 200 \text{ nm}^2$. The vertical dashed line represents the boundary where $d_{\text{hole}} = d_{\text{wall}}$.

Assuming that the wall thickness of the HPS bead is the same for all the beads, for a constant etching current one expects a linear behavior of the FIB etching time versus etched surface area. A linear fit of the etching time versus etched surface area yields a correlation coefficient of ~ 0.99 , which enables etching time prediction for a given hole surface area. Square holes with sizes varying from 30 to 500 nm were drilled, demonstrating a drilling dynamic range larger than one order of magnitude. In addition, square holes were drilled on several polystyrene scaffolds using the FEI FIB 200, see Figure 6.4. The results achieved with both FIB instruments show similar behavior, despite the difference in their currents. This may be due to the differences in the beam diameter between the two FIB machines and the re-deposition of the etched material [1,11] occurring during the etching process.

Redeposition. For hole sizes $d_{hole} < 100$ nm, there is a deviation from the linear fit, as indicated in Figure 6.4.B. The size of these holes is smaller than the wall thickness of the scaffold, $d_{wall} = 100$ nm. In such a case, the re-deposition rate of the etched material [1,11] that occurs during the etching process is expected to be higher compared to the case of holes with a size $d_{hole} \gg d_{wall}$. If there is a small hole in a thick wall, the chance the material escapes the hole is smaller. We found that during the very first second, drilling of holes down to 30 nm was not possible.

Elongated holes. An elongated profile of the etched holes was observed for sizes < 100 nm. For instance, drilling of a 50×50 nm² hole yielded a profile of $\sim 50 \times 56$ nm² (see Figure 6.5.A). Scanning of such a small surface may yield an increase of the surface charge. Hence, deflections of the beam might occur, resulting in a beam instability that could cause the observed elongation.

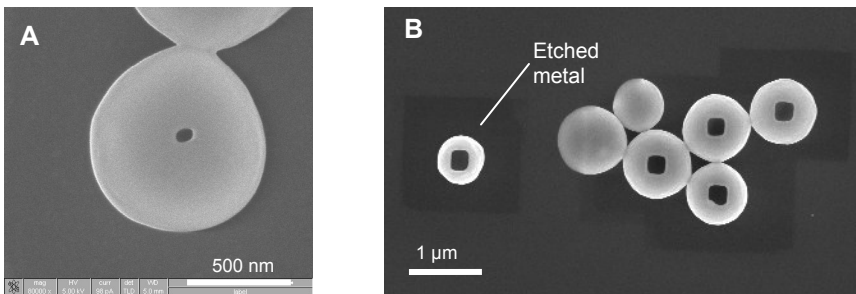


Figure 6.5. (A) SEM image of a 50 nm hole etched for 2 seconds. Note the elongated profile of the hole. (B) FIB image of HPS scaffolds with single holes. Note the slightly damaged (etched) metal coating areas around the scaffolds with single holes. Etching current was 1.5 pA.

Bead instability. The stability of the bead that was being etched is another factor that influences the drilling process. While processing with FIB, the scaffolds did

not always maintain their initial position. We observed that beads were displaced or rotated due to local charging around them. During the focusing on the bead we damage the metal area as can be seen from the black region in Figure 6.5.B. In the case of beads supported on a gold surface, which was not as stable as Ti, a slightly longer time was required to etch a given hole.

6.5 Discussion and conclusions

In this chapter we fabricated a spherical (sub)micrometer polymeric scaffold containing a single nanohole. The scaffold was made of polystyrene with typical dimensions of $\sim 1 \mu\text{m}$ outer diameter and wall thickness of $\sim 100 \text{ nm}$. Machining of single nanoholes on such hollow polymer scaffolds was performed, for the first time to our knowledge, with a focused gallium ion beam.

Etching of single holes was performed in a controlled manner. We drilled single square holes of desired dimensions varying from 30 to 500 nm on several polystyrene scaffolds in 2 to 70 seconds per hole using the lowest beam currents. A linear behavior between the etched surface area and etching time was found, allowing prediction of etching time for a given hole surface area and wall thickness.

The polystyrene scaffolds showed a good positioning stability and maintained the integrity of their structure, remaining hollow after FIB processing. We observed that the surface discharging is important for both scaffold stability and the beam etching efficiency. Damage of the metal coating around the scaffold may be an additional factor that causes bead instability, influencing the etching process.

Glass scaffolds containing microholes were developed using FIB drilling (see Appendix C). We drilled square holes with dimensions of ~ 1 to $3 \mu\text{m}$ using high beam currents of 48 to 350 pA in ~ 1 to 20 minutes. The glass scaffolds were more unstable than polystyrene ones due to the use of higher etching currents.

An array of holes in a polystyrene coated substrate was additionally fabricated using FIB drilling (Appendix C), providing additional information on polystyrene etching on surfaces that have a better defined geometry and stability. Here we explored the etching rate of polystyrene for different hole sizes for a thicker layer than HPS scaffold wall and using higher etching currents. Holes with a size varying from 200 to 400 nm were drilled through a $1 \mu\text{m}$ thick polystyrene layer using ion currents varying from 1 to 11 pA.

References

- [1] J. Orloff, M. Utlaut, and L. Swanson, *High Resolution Focused Ion Beams: FIB and its Applications*, Kluwer Academic / Plenum Publishers, New York, USA, ISBN 0-306-47350-X, 2003.
- [2] M.C. Woodle, Controlling liposome blood clearance by surface-grafted polymers, *Advanced Drug Delivery Reviews*, 1998, **32**, 139-152.
- [3] M.H. Cohen, K. Melnik, A.A. Boiarski, M. Ferrari, and F.J. Martin, Microfabrication of Silicon-Based Nanoporous Particulates for Medical Applications, *Biomedical Microdevices*, 2003, **5 (3)**, 253-259.
- [4] O. Ishida, K. Maruyama, K. Sasaki, and M. Iwatsuru, Size-dependent extra vacation and interstitial localization of polyethyleneglycol liposomes in solid tumor-bearing mice, *International Journal of Pharmaceutics*, 1999, **190**, 49-56.
- [5] M. Mayer, J.K. Kriebel, M.T. Tosteson, and G.M. Whitesides, Microfabricated Teflon Membranes for Low-Noise Recordings of Ion Channels in Planar Lipid Bilayers, *Biophysical Journal*, 2003, **85**, 2684-2695.
- [6] TechNote 206, Bangs Laboratories, Inc, Fishers, IN, USA, <http://www.bangslabs.com/technotes/206.pdf>.
- [7] A.H.B. de Vries, High Force Magnetic Tweezers For Molecular Manipulation Inside Living Cells, *Ph.D. Thesis*, 2004, University of Twente, Enschede, The Netherlands, 45-49.
- [8] A.H.B. de Vries, J.S. Kanger, E.B. Krenn, and R. van Driel, Patterned electroplating of micrometer scale magnetic structures on glass substrates, *Journal of Microelectromechanical Systems*, 2004, **13**, 391-395.
- [9] FEI FIB 200, MASER Engineering B.V., Enschede, The Netherlands, 2006, <http://www.maser.nl/equipmentlest.pdf>.
- [10] FEI FIB Nova 600 NanoLab, FEI, Eindhoven, The Netherlands, 2006, http://www.fei.com/Portals/_default/PDFs/content/2006_06_Nova600NanoLab_pb.pdf
- [11] S. Reyntjens, R. Puers, A review of focused ion beam applications in microsystem technology, *Journal of Micromechanics and Microengineering*, 2001, **11**, 287-300.

CHAPTER SEVEN

NANOFABRICATED BIOMIMETIC DEVICES

We successfully developed hybrid nanodevices based on spherical polystyrene scaffolds. We loaded the scaffold through a single nanometer scale access hole that was drilled in the scaffold, sealed the hole with a lipid membrane, and demonstrated controlled efflux of a fluorescent dye through a protein nanovalve inserted in the membrane.

7.1 Introduction

This chapter describes the development of an integrated hybrid device based on a nonbiological scaffold combined with lipid membranes modified with functional proteins. In the previous chapter, we presented the fabrication of well-defined nanometer size holes in spherical polymeric and glass scaffolds as a basis towards individual integrated biomimetic devices. Here, we describe the loading with aqueous solutions of these devices incorporating biomolecules with a tunable functionality. In this way, we are able to create devices carrying a payload and incorporating a biological nanovalve that can be triggered at will.

7.2 Methods to load scaffolds

Loading a payload into a micro-scaffold by means of a nanometer size hole presents several difficulties. When immersing a scaffold in a hydrophilic solution, air inside the scaffold resists the loading process because of the atmospheric pressure and the small hole dimensions, contributing to an increase of surface tension forces. The unfavorable wetting properties of the hydrophobic polystyrene scaffolds are additional obstacles to the diffusion of the solution in the scaffold. Such problems are well known in microfluidic devices [1].

One way to load this micro-scaffold is to use a sub-micro needle, while an alternative is to find a way to reduce the forces opposing the diffusion. Two possibilities exist for the later: reducing the tension forces that occur in the region of the nanohole and/or reducing the pressure inside the scaffold.

Reduction of the tension forces involves the use of chemical methods. Small changes in the viscosity of the solution by adding a small percentage of a higher viscosity solution such as ethanol results in a significant reduction of tension forces, which promotes loading of the scaffold. Such a method has been applied for filling carbon nanotubes [2].

Loading procedures at reduced pressures involves methods such as the channel outgas technique, which was successfully applied for filling hydrophobic polymeric microfluidic structures with an aqueous solution [1]. In this method, the sample was immersed in solution and the atmospheric pressure above the sample was reduced by vacuuming. The advantage of such a technique is that no chemical modification is required.

We used a combination of chemical modification and the channel outgas technique to load our micro-scaffolds.

7.3 Modeling the diffusion through a nanohole in a scaffold

We present an analytical model for the diffusion of a solute into a spherical scaffold through the nanoholes based on Equations 5.3 and 5.4 (Chapter 5) derived from Fick's law [3,4].

In the case of a hollow spherical polystyrene scaffold with a volume V , separated from the bulk medium by a wall of thickness d_h that contains a single nanohole of cross section S_h (see Figure 7.1.A), the diffusion of solutes into the scaffold interior is dependent on the diffusion through the nanohole.

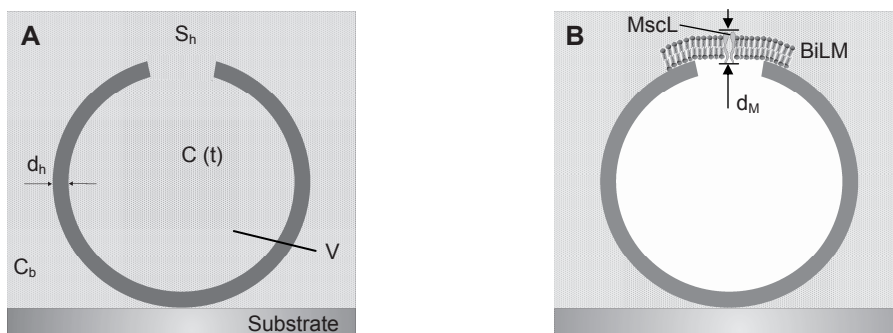


Figure 7.1. Schematic of a hollow scaffold with a single nanohole immersed in aqueous solution. (A) Open hole, (B) hole sealed with a bilayer lipid membrane (BiLM) containing a MscL channel protein.

Since the volume V is much smaller than that of the bulk, the bulk concentration is assumed constant. Hence, considering as boundary conditions the initial concentration $C(t=0)=0$, while the final concentration equals the bulk concentration C_b , which remains constant, the time dependent concentration $C(t)$ of the solute in the scaffold interior at a certain time t is written in analogy with Eq. 5.4 (see Chapter 5) as:

$$C(t) = \left[1 - e^{-D \frac{S_h t}{d_h V}} \right] C_b \quad [7.1]$$

where D is the diffusion coefficient.

Based on Eq. 7.1, we first calculate $C(t) = f(t)$ in the case of diffusion through an open hole in a HPS scaffold with an inner diameter of $0.8 \mu\text{m}$, a solute with a diffusion coefficient of $3.3 \times 10^{-10} \text{ m}^2/\text{s}$ (calcein in PBS buffer) [5], $d_h = 100 \text{ nm}$, S_h

$\sim 200 \times 200 \text{ nm}^2$, and $V = 0.27 \times 10^{-18} \text{ m}^3$. The change in the concentration $C(t)$ as function of time is illustrated in Figure 7.2.A.

If the hole in the scaffold is sealed by a lipid membrane containing protein nanochannels such as MscL [6-8], the diffusion of the solutes into the scaffold is dependent on the diffusion through the protein channel, which is now the limiting factor. The diffusion from Eq. 7.1 can be modified in this case (in analogy with Eq. 5.5, Chapter 5) as:

$$C(t) = \left[1 - e^{-\frac{D n S_M \gamma_{on} t}{d_M V}} \right] C_b \quad [7.2]$$

where γ_{on} is a factor that describes the fraction of time during which a channel remains open and diffusion occurs, n is the number of nanopores embedded in the membrane, d_M is the length of the protein channel (see Figure 7.1.B), and S_M is the protein opening cross-section. Considering the same solute and scaffold

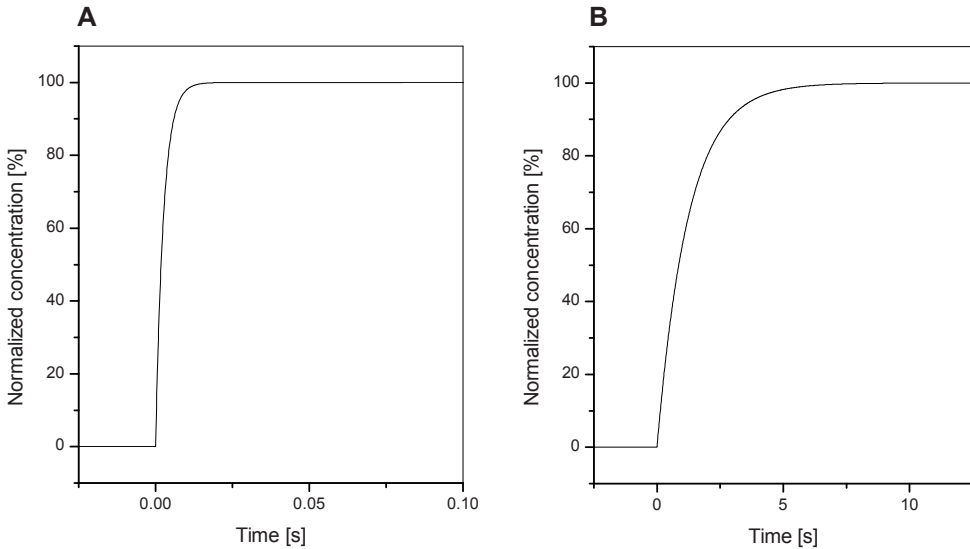


Figure 7.2. Theoretical time course of diffusion of a solute into a polystyrene scaffold (A) via an open square hole as derived analytically from Eq. 7.1; (B) via a MscL channel imbedded in a bilayer lipid membrane that seals the hole (see Eq. 7.2) by considering a single protein channel behaving as a valve that remains open for 25% of the time.

volume as above, a single MscL channel protein having a length ~ 8.5 nm [9], channel cross section of 7.1×10^{-18} m² (corresponding to a pore diameter of 3 nm [7]), and $\gamma_{on} \sim 0.25$, the change in the concentration as function of time is illustrated in Figure 7.2.B.

Based on Eq. 7.1 and 7.2, assuming that $n = 1$ and $\gamma_{on} = 1$ in Eq. 7.2, the diffusion into the scaffold is dependent on the ratio (S_h / d_h) and (S_M / d_M) , respectively. Using the parameters that were included in Figure 7.2.A and B, the relative ratio $(S_h / d_h) / (S_M / d_M) \sim 1000$, which means that the diffusion through the protein channel occurs 1000 times slower than through the hole in the scaffold. So, the limitations due to the diffusion through the hole S_h in the scaffold are neglected in Eq. 7.2.

As can be seen in Figure 7.2, the diffusion occurs very fast (< 1 s) in the case of a sub-micrometer size scaffold containing a single hole (200 nm size) in the scaffold. This fast filling makes it difficult to monitor such a process using CLSM. Although the diffusion occurs much slower through a single MscL channel pore, requiring several seconds, considering the small dimensions of the scaffold, factors such as stage drift in the Z direction, finding the right focus plane (through the center), laser intensity instabilities, and dye bleaching due to continuous laser scanning makes it practically difficult to monitor such dynamics, e.g. by measuring the fluorescence intensity in time in a spot inside the scaffold.

7.4 Materials and methods

Materials

Fluorescent solid polystyrene beads (diameter ~ 1.3 μ m) in which FITC (fluorescein isothiocyanate) dye is distributed uniformly in the bead matrix, 900 nm diameter solid polystyrene beads which have a modified surface with carboxyl groups (COOH), and hollow polystyrene (HPS) beads of inner diameter of 800 nm and wall thickness of 100 nm were purchased from Polysciences (Warrington, PA, USA). FITC labelled biotin was obtained from Sigma (Zwijndrecht, The Netherlands). Rhodamine123 was purchased from Molecular Probes (Leiden, The Netherlands). MTSET ([2-(trimethylammonio)ethyl]methanethiosulfonate, Anatrace, Inc., Maumee, OH, USA) was a kind gift from the Biomade Technology Foundation (Groningen, The Netherlands).

FITC-coated solid polystyrene beads. The carboxylate-modified solid polystyrene beads were coated with streptavidin by covalent coupling and were re-suspended in PBS solution. A 100 μ l solution of streptavidin-coated beads (bead concentration of 2.4×10^9 beads/ml) was incubated for about 15 minutes at room temperature with 50 μ l fluorescent-labelled biotin solution (biotin concentration of 0.5 mg/ml). After incubation, the beads were washed 4 times

with PBS in order to wash away the uncoupled dye (each time spinning down the beads for 5 minutes at 10000 rpm, discarding the old PBS and adding new PBS for the next wash). The washed beads were re-suspended in 100 μ l PBS. The result was the formation of a thin fluorescent layer on the surface of the polystyrene beads. DABCO (1,4-Diazabicyclo [2.2.2] octane, chemical formula $C_6H_{12}N_2$) was added to the mixture to help maintain a stable dye fluorescence intensity for a longer time.

Scaffolds with single holes. Hollow polystyrene and glass scaffolds were supported on titanium/gold-coated transparent substrates and single holes were drilled using focused ion beam drilling in the same way as described in Chapter 6.

Construction of the cuvette. A Teflon cuvette supported by metal holders on both upper and lower sides was constructed to accommodate the sample containing the scaffolds during their incubation in the solution. A schematic of the cuvette is shown in Figure 7.3.

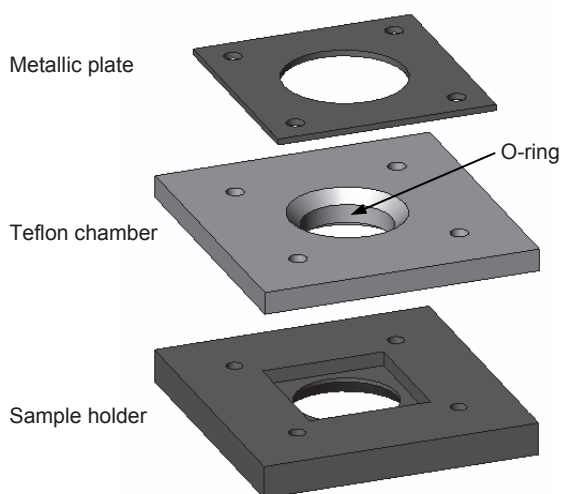


Figure 7.3. Schematics of the cuvette used for CLSM measurements. The cuvette consists of a metallic holder where the sample is supported, a Teflon chamber with an O-ring at the bottom that presses on the sample, and a metallic top plate.

Preparation of giant unilamellar lipid vesicles. Unilamellar lipid vesicles were prepared using the freeze-thaw method. MscL channel proteins were incorporated in the lipid vesicles by applying the detergent mediated method [10-11]. Finally, by using electroformation [12], giant lipid proteovesicles were prepared. A detailed description of the vesicle preparation is given in section 5.4.

Membrane deposition on the hole in a scaffold. Hollow polystyrene or glass beads were fixed on a gold-coated 170 μ m thick transparent substrate. Single holes of diameter varying from 100 to 400 nm for polystyrene beads and 1 to 2

μm for the glass beads were drilled on beads that were optically distinguishable from the others as shown in the previous chapter. The substrate with beads was mounted on the Teflon cuvette (see previous section) and incubated with 0.01% PLL in PBS solution overnight at 4 °C. The PLL was rinsed from the cuvette by washing with buffer. Ethanol solution was added in the cuvette to a final concentration of 2%. The sample was placed for about 2 hours in a desiccator that was maintained in vacuum using a laboratory pump (Laboport[®], KNF Neuberger GmbH, Freiburg, Germany). The ethanol was rinsed from the sample by washing with buffer.

Glucose loaded (400 mM) giant unilamellar lipid vesicles containing MscL were added in the cuvette. Vesicles were first fluorescently labeled with DiA fluorophore by adding $\sim 1 \mu\text{l}$ of 400 $\mu\text{g/ml}$ of DiA/methanol stock solution in 1 ml vesicle solution. Single vesicles were trapped with optical tweezers using the minimum trapping laser output power (0.2 W) and directed to the top of the beads to induce collapse. Minimum laser power was used to prevent the local increase of the temperature due to heating of the metal layer when the optical trap was on (or in the vicinity of) the surface. White light transmission and epifluorescence imaging were used to address a vesicle to a certain bead and to monitor vesicle collapse on this bead, similar to the case of the flat substrates.

After membrane deposition, the sample was transported to the CLSM microscope for further processing. About 70 μl of 15 mM calcein stock solution in phosphate buffer (pH 8) were added to $\sim 2 \text{ ml}$ bulk vesicle solution in the cuvette.

No ethanol and vacuum processing steps were applied for glass scaffolds.

7.5 Results and discussion

We demonstrate successful loading of polystyrene and glass scaffolds containing a single hole with aqueous dye solution. We also show that effective sealing of the holes with a bilayer lipid membrane was achieved. Finally, we demonstrate the biofunctionality of such a hybrid device.

7.5.1 Loading of the scaffold

Hollow polystyrene scaffolds. We used confocal fluorescence microscopy to observe loading of the polystyrene scaffolds with aqueous solutions of fluorescent dyes. Measurements were performed using a Confocal Laser Scanning Microscope (CLSM) (Zeiss LSM 510, Carl Zeiss, Oberkochen, Germany). The technique was first tested to establish its utility for imaging small polystyrene scaffolds, for distinguishing between the fluorescence inside and outside the

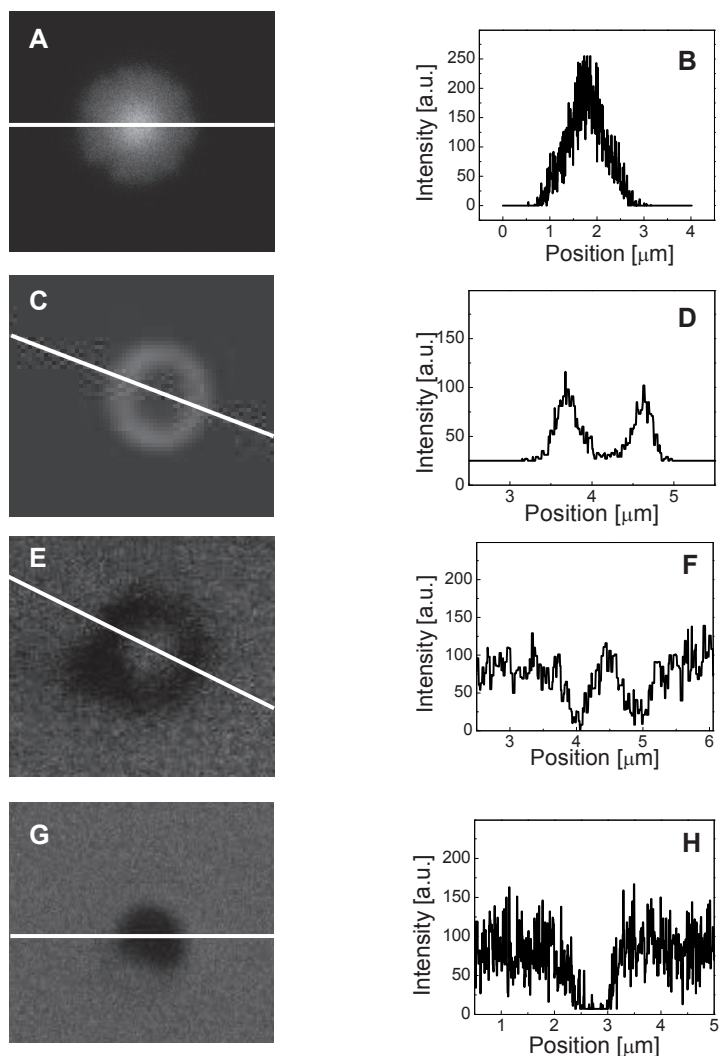


Figure 7.4. Characterization of scaffold loading. CLSM image through the center of (A) a fluorescent solid PS bead, which is immersed in a water; (C) a fluorescently labelled PS bead immersed in a water; (E) a HPS scaffold filled with aqueous solution of Rhodamine 123 containing ethanol; (G) a HPS scaffold with no hole, enclosing water and immersed in 2% ethanol-Rhodamine 123 solution. (B), (D), (F), and (H) present the fluorescence intensity profiles across the lines as indicated in image (A), (C), (E) and (G), respectively.

scaffold, and for discriminating between different confocal slices through the scaffold. Thus, control measurements were first performed on beads with various fluorescence properties for testing the spatial resolution of the CLSM (see Figure 7.4.A, B, C, and D). Here, confocal slices through the center of the beads were acquired. The image was chosen from a stack of slices made at different depths (step size of 250 nm). The results obtained showed that the resolution of the CLSM is sufficient to distinguish between the fluorescence inside and outside the polystyrene scaffolds.

We further applied this technique on polystyrene scaffolds and analysed the fluorescence intensity from the confocal slice close to the center of a scaffold. Figure 7.4.E depicts the fluorescence image of a scaffold with a hole loaded with aqueous Rhodamine 123 solution containing ethanol. Loading occurred within a few seconds after immersing the dried HPS scaffolds in the dye solution containing 2% ethanol. The addition of ethanol was required to lower the surface tension. No filling was observed when using water only. A fluorescence intensity profile across the fluorescent image of Figure 7.4.E is presented in Figure 7.4.F. As expected, the fluorescence intensity shows a Gaussian distribution, which indicates that the inner volume of the scaffold is filled with dye. The minimum intensity occurs at the position of the shell. It should be noted that the dimensions of the scaffold are close to the optical resolution of the microscope, which prevents observation of sharp transitions between the non-fluorescent wall and the fluorescent solution. Furthermore, the fluorescence intensity inside the scaffold (see Figure 7.4.F) is comparable with the intensity of the background, as expected. Loading of scaffolds was also obtained by immersing them in vacuum. These scaffolds were previously submerged in aqueous dye solution containing 2% ethanol, which was rinsed with buffer after vacuuming.

As a control, scaffolds that did not contain a hole were measured. No fluorescence could be observed in these scaffolds indicating that the loading of the scaffolds was accomplished by transport through the holes only. Additional measurements were performed to further test the permeability of the scaffold wall. HPS beads, which enclose water, were incubated in a cuvette with an aqueous dye solution supplemented with 2% ethanol for more than a week. Fluorescence measurements were performed in several scaffolds for different time intervals and no change of the fluorescence intensity was observed inside the scaffolds (see Figure 7.4.G and 7.4.H). Hence, no observable diffusion occurred through the wall of the polystyrene scaffold, indicating the impermeability of the scaffold.

Hollow glass scaffolds. In addition to HPS scaffolds, HG scaffolds containing a single micrometer size hole and supported on gold surfaces were loaded with aqueous dye solution. Figure 7.5.B depicts a confocal slice through the centre of a HG bead loaded with calcein. Loading of scaffolds through holes with a size of 1 μm and bigger required no treatment with ethanol or vacuum as in the case of HPS scaffolds.

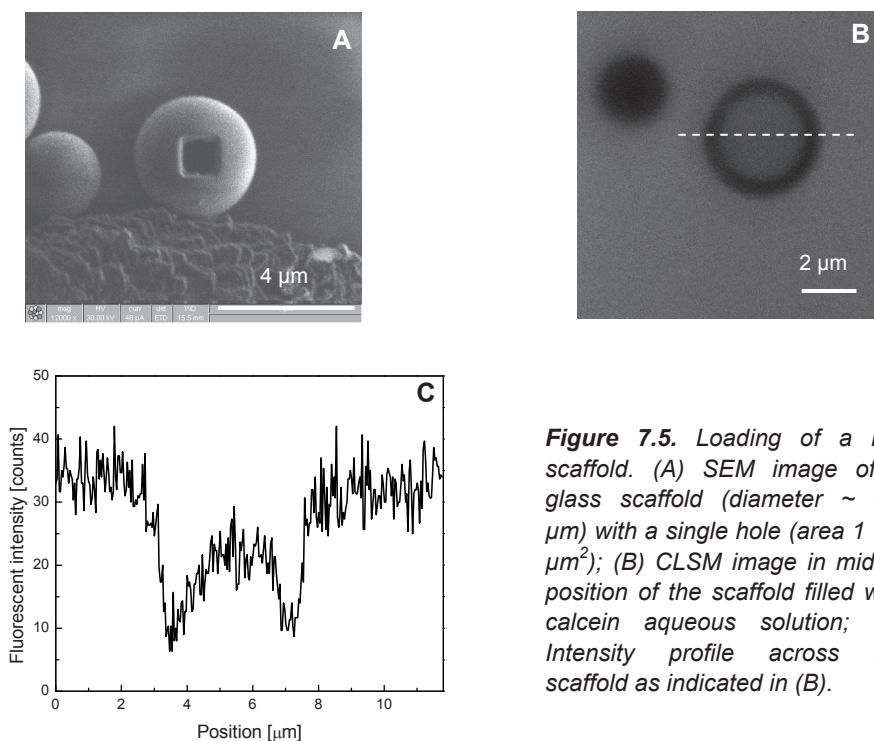


Figure 7.5. Loading of a HG scaffold. (A) SEM image of a glass scaffold (diameter $\sim 3.7 \mu\text{m}$) with a single hole (area $1 \times 1 \mu\text{m}^2$); (B) CLSM image in middle position of the scaffold filled with calcein aqueous solution; (C) Intensity profile across the scaffold as indicated in (B).

7.5.2 Sealing the scaffold with a lipid membrane

In Chapter 4, we demonstrated sealing of a hole in a flat Pyrex substrate with a lipid membrane. Here we go a step further towards realization of a self-contained device by sealing a single hole in a spherical polystyrene scaffold with a bilayer lipid membrane. We also present successful sealing of spherical glass scaffolds.

HPS scaffold. First, the hole was sealed (see Figure 7.6.A) with the membrane as described in the methods section. Later, calcein dye was added in the bulk solution to probe the quality of sealing and the membrane quality by monitoring any passive diffusion of calcein via the hole into the buffer-loaded bead.

Figure 7.6.B shows a confocal image of a polystyrene scaffold containing a single hole (bead diameter $\sim 1.2 \mu\text{m}$, hole surface area of $300 \times 300 \text{ nm}^2$) that was sealed with a lipid membrane. This image is a confocal slice through the centre of the scaffold. There was no fluorescence intensity inside the scaffold, which appears as a black region in Figure 7.6.B, indicating that the hole was sealed by the lipid membrane and that the membrane has no defects or pores that could

lead to passive diffusion of calcein into the scaffold. There was a clear difference when comparing it with a loaded scaffold that was not sealed with lipid membrane (Figure 7.6.D).

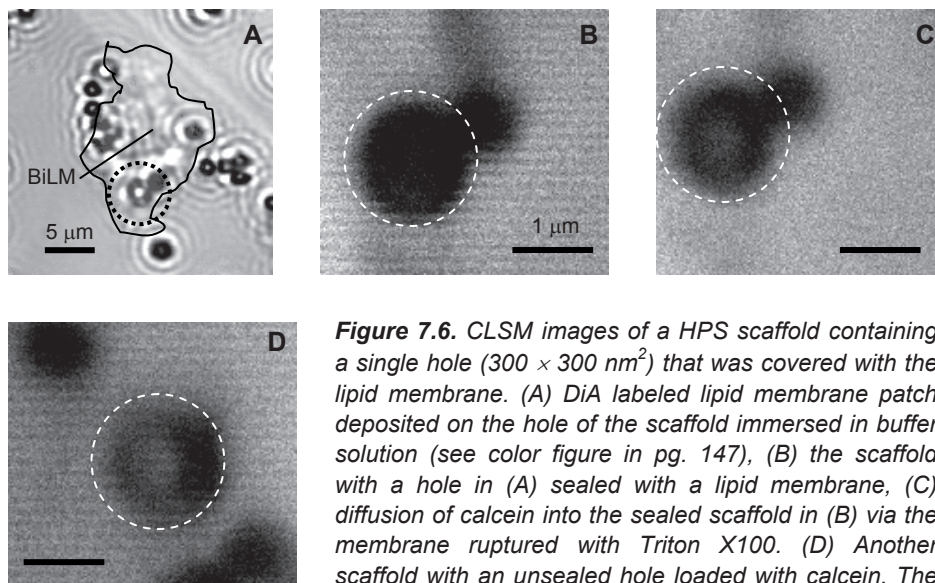


Figure 7.6. CLSM images of a HPS scaffold containing a single hole ($300 \times 300 \text{ nm}^2$) that was covered with the lipid membrane. (A) DiA labeled lipid membrane patch deposited on the hole of the scaffold immersed in buffer solution (see color figure in pg. 147), (B) the scaffold with a hole in (A) sealed with a lipid membrane, (C) diffusion of calcein into the sealed scaffold in (B) via the membrane ruptured with Triton X100. (D) Another scaffold with an unsealed hole loaded with calcein. The scaffolds of interest are enclosed by dashed circles. Images in (B), (C), and (D) are confocal slices through the center of the scaffolds.

After sealing the hole with the membrane and adding the calcein, the sample was kept at 4°C for more than 2 weeks. The hole remained sealed as no significant diffusion of dye into the scaffold was observed, demonstrating the stability of the sealing membrane. Furthermore, the membrane remained stable despite the presence of destructive factors such as surface tension, mechanical disturbance, and vibrations occurring during sample transportation. Upon addition of $80 \mu\text{l}$ of 10% Triton X100 solution in water to 2 ml bulk medium, the sealed scaffold was loaded with calcein, as presented in Figure 7.6.C. The Triton ruptured the membrane and consequently, the dye molecules could passively diffuse into the unloaded scaffold.

In Figure 7.7, the normalized fluorescence intensity in the sealed HPS scaffold measured at different time intervals prior to and after addition of Triton is presented. Prior to the Triton addition, the intensity in the scaffold was at the background level. A step-like increase in intensity occurred after the rupture of the membrane. The intensity increase after adding Triton indicates the passive dye

diffusion into the scaffold due to the membrane rupture. There is a clear intensity increase upon the addition of Triton, as presented in Figure 7.7.

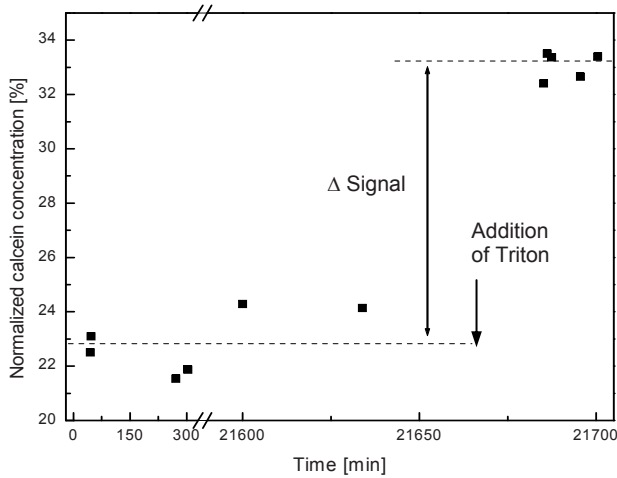


Figure 7.7. Normalized calcein concentration in the sealed scaffold prior to and after Triton addition. Note the long time stability of the membrane. Different time scales in X-axis are used to better visualize membrane stability and rupture. Calcein concentration is normalized to the bulk concentration. The arrow indicates the time of Triton addition in the bulk solution for rupturing the membrane.

The saturation fluorescence intensity level inside the scaffold after membrane rupture reaches about 33% of the bulk intensity. Different factors could influence such a low intensity. The losses caused by the polystyrene (scattering) when light is refracted through its wall could result in a decrease of the excitation power that reaches the interior of the scaffold when compared to the bulk. The same holds also for the fluorescence light of the excited fluorophores within the hollow bead. An additional factor could be the round geometry of the scaffold and probably the nonuniformity in the wall surface roughness that might yield additional scattering. Furthermore, the gold coating underneath the scaffold might cause fluorescence quenching. Finally, averaging the intensity, which shows a Gaussian distribution, for a region of interest inside the scaffold instead of considering a line profile yields a further decrease of the intensity.

HG scaffold. In addition, glass scaffolds with a hole were tested by sealing the hole with a membrane. Figure 7.8.B presents a confocal image of a glass scaffold containing a single hole (outer diameter $\sim 5.35 \mu\text{m}$, hole surface area $1 \times 1 \mu\text{m}^2$) that was sealed with lipid membrane. After isolation (see Figure 7.8.A), calcein

was added to the bulk solution to probe the quality of sealing and membrane integrity. The absence of calcein intensity inside of the scaffold demonstrates that the hole was sealed by the membrane.

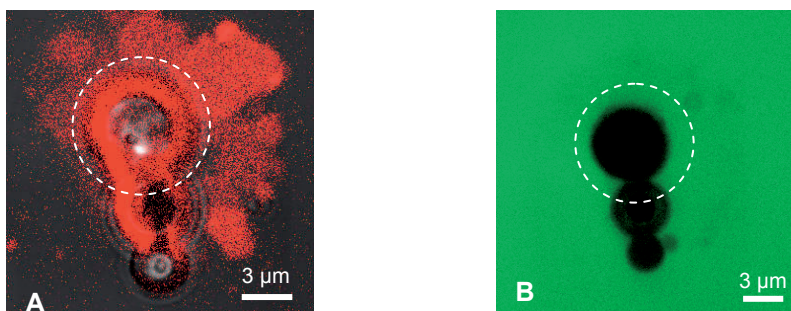


Figure 7.8. CLSM images of a HG scaffold (diameter $\sim 5.35 \mu\text{m}$) containing a single hole (area $1 \times 1 \mu\text{m}^2$) that was covered with a lipid membrane. (A) DiI-labeled lipid membrane patch deposited on the hole of the scaffold immersed in buffer solution. (B) Sealed scaffold in (A) immersed in calcein aqueous solution. The scaffold of interest is enclosed by the dashed circle. Images are confocal slices through the scaffolds.

7.5.3 Functionalization of the spherical hybrid vehicles

After sealing the hole with a lipid membrane, we demonstrated functionalization of the membrane with MscL channel protein, and monitored the externally triggered functionality of the protein.

HPS scaffolds. The functionality of MscL protein in a membrane deposited on the hole of a spherical scaffold was monitored using CLSM. The HPS scaffold containing a single hole was loaded with buffer and the hole was sealed in a controlled fashion with the lipid proteomembrane using optical tweezers. Next, calcein was added to the bulk solution and the sealed scaffolds were selected for monitoring the MscL activity. Figure 7.9.A presents a CLSM image of a HPS scaffold containing a single hole (scaffold diameter $\sim 1 \mu\text{m}$, hole surface area $\sim 300 \times 300 \text{ nm}^2$) that was sealed with a lipid membrane. Prior to the channel activation no calcein diffused inside the scaffold (appearing as a black region in Figure 7.9.A), demonstrating a good seal of the nanohole with lipid membrane. The seal remained intact for > 1 day at $4 \text{ }^\circ\text{C}$. The activity of MscL channel protein was initiated by adding $25 \mu\text{l}$ of 80 mM MTSET solution (dissolved in PBS) to 2 ml bulk medium. Figure 7.9.B presents a CLSM image of the HPS scaffold loaded

with calcein through the MscL channel a few minutes after activating the channel opening.

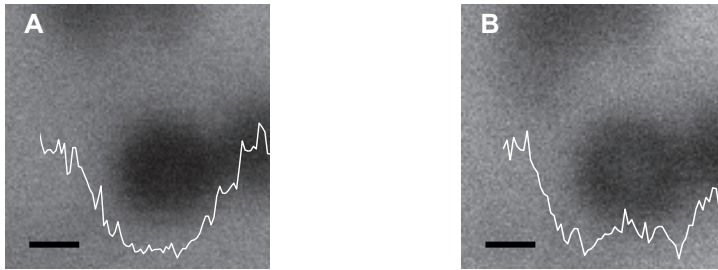


Figure 7.9. CLSM images of a HPS scaffold containing a single hole that was covered with a lipid membrane containing MscL protein. (A) Scaffold immersed in calcein solution, prior to MscL activation. No calcein diffusion inside the scaffold occurred. (B) Diffusion of calcein into the sealed scaffold in (A) via the activated MscL channel protein. Images are confocal slices through the center of scaffold. The white lines are intensity profiles of cross sections through the scaffold centers. Due to combination of two data sets in these pictures, the scaling of the intensity profiles could be a bit different. Scale bar is 0.5 μm .

Figure 7.10 shows the normalized fluorescence intensity in the sealed HPS scaffold measured at different time intervals, prior to and after activation of the MscL protein. Prior to MscL activation, the intensity in the scaffold was at the background level. The intensity increased significantly after addition of the MTSET, as a result of passive dye diffusion into the scaffold via the opening of the MscL channel.

However, MscL activity could not be observed for every HPS scaffold sealed with a proteomembrane (2 out of 20 showed activity). This may be due to the absence of MscL protein in the membrane region that covers the hole, a scenario that could be improved by optimizing the preparation method in order to increase the protein concentration in the vesicles. Referring to the results achieved with other techniques such as patch-clamp, up to 10 - 20 MscL proteins were found in a 1 μm^2 membrane patch [13]. Therefore, the probability to have a protein in a $\sim 300 \times 300 \text{ nm}^2$ patch decreases proportionally with the surface area decrease, which is about one order of magnitude.

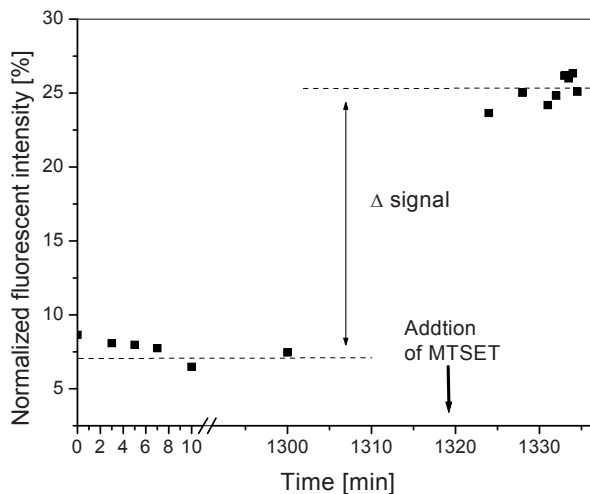


Figure 7.10. *Calcein intensity in the sealed scaffold normalized to the bulk intensity prior to and after the activation of MscL channel protein upon addition of MTSET. Data points were obtained by averaging the fluorescence intensity inside the scaffold.*

7.6 Conclusions

In this chapter we have presented the development of a novel spherical hybrid nanodevice by combining a nonbiological scaffold containing a hole with a biofunctionalized lipid membrane that seals the hole. In such a device, the scaffold loading, biomodification and protein channel gating were performed in a controllable fashion. Besides the polystyrene scaffold used here, other polymer materials with better specific biocompatibility and biodegradability properties could also be used.

We were able to load the hydrophobic scaffolds with hydrophilic solution. This indicates that, in principle, we are able to load any sort of drug in our hydrophobic scaffold. Furthermore, measurements showed that the polystyrene scaffolds were impermeable for small fluorophores.

We successfully functionalized the scaffold by sealing the hole with an artificial lipid membrane containing functional MscL channel protein. The membrane deposition was performed in a controlled fashion by directing a proteovesicle to collapse onto the hole using an optical trap. A good sealing of the hole in the scaffold was achieved and the proteomembrane remained remarkably stable for more than 2 weeks until we deliberately ruptured the membrane. This period is

much longer compared to currently achieved membrane systems [14]. We deliberately triggered the MscL protein activity, inducing a controlled loading/release through the MscL nano-valve.

Our nanodevice is a robust system and is likely to be relevant for drug delivery applications in clinical settings. The ability to control release from our device by ambient pH change and the sensitivity to a small ambient pH change could find application in targeted drug delivery, such as targeting tumor cells. It is well known that the pH around the tumor tissue is lower than the physiological pH (pH 7.4) [15], which could allow specific delivery of chemotherapeutic agents of our device to tumors. Our device shows advantages when compared to vesicles and polymersomes. Liposomes suffer from limited stability [17] and are leaky structures due to the effect of osmolarity [16], whereas polymersomes are not a natural support for biomolecules.

This device is a free-standing system that could freely move and potentially be used for drug delivery. Such a device could be manipulated and transported in different positions, therefore allowing flexibility in operation. The fact that the device has a defined volume allows quantification of diffusion processes. If other particles such as cells and vesicles could be brought in contact with the device, a local exchange between the two systems can occur. Such enclosed information exchange can be interesting to better understand and study specific interactions between them.

A high throughput of our nanodevice could be achieved by patterning the scaffolds on a support to enable automated processing, as demonstrated with the flat polystyrene substrates in Chapter 6.

Acknowledgement

We would like to thank Dr. Armağan Koçer from BioMade Technology Foundation (The Netherlands) who kindly prepared the giant vesicles containing MscL proteins in the framework of a collaboration.

References

- [1] J. Monahan, A.A. Gewirth, and R.G. Nuzzo, A method for Filling Complex Polymeric Microfluidic Devices and Arrays, *Analytical Chemistry*, 2001, **73**, 3193-3197.
- [2] A.V. Eletskiĭ, Carbon nanotubes, *Physics - Uspekhi*, 1997, 40, 899-924.
- [3] H.C. Berg, Random Walks in Biology, Princeton University Press, New Jersey, USA, 1983, ISBN 0-691-08245-6.
- [4] P. Paradisi, R. Cesari, F. Mainardi, and F. Tampieri, The fractional Fick's law for non-local transport processes, *Physica A*, 2001, **293**, 130-142.

- [5] N. Yoshida, M. Tamura, and M. Kinjo, Fluorescence Correlation Spectroscopy: A New Tool for Probing the Microenvironment of the Internal Space of Organelles, *Single Molecules*, 2000, **1**, 279-283.
- [6] C. Kung and P. Blount, Channels in microbes: so many holes to fill, *Molecular Microbiology*, 2004, **53**, 373-380.
- [7] S. Sukharev and A. Anishkin, Mechanosensitive channels: what can we learn from 'simple' model systems?, *TRENDS in Neurosciences*, 2004, **27**, 345-351.
- [8] S.I. Sukharev, P. Blount, B. Martinac, and C. Kung, MECHANOSENSITIVE CHANNELS OF *ESCHERICHIA COLI*: The MscL Gene, Protein, and Activities, *Annu. Rev. Physiol.*, 1997, **59**, 633-657.
- [9] G. Chang, R.H. Spencer, A.T. Lee, M.T. Barclay, and D.C. Rees, Structure of the MscL Homolog from *Mycobacterium tuberculosis*: A Gated Mechanosensitive Ion Channel, *Science*, 1998, **282**, 2220-2226.
- [10] J-L. Rigaud, B. Pitard, and D. Levy, Reconstitution of membrane proteins into liposomes: application to energy-transducing membrane proteins, *Biochimica et Biophysica Acta*, 1995, **1231**, 223-246.
- [11] D. Lévy, A. Gulik, A. Bluzat, and J-L. Rigaud, Reconstitution of the sarcoplasmic reticulum Ca^{2+} -ATPase: mechanisms of membrane protein insertion into liposomes during reconstitution procedures involving the use of detergents, *Biochimica et Biophysica Acta*, 1992, **1107**, 283-298.
- [12] P. Girard, J. Pécréaux, G. Lenoir, P. Falson, J-L. Rigaud, and P. Bassereau, A new method for the Reconstitution of Membrane Proteins into Giant Unilamellar Vesicles, *Biophysical Journal*, 2004, **87**, 419-429.
- [13] M.K. Doven, J.H.A. Folgering, V. Krasnikov, E.R. Geertsma, G. van den Bogaart, and B. Poolman, Distribution, Lateral Mobility and Function of Membrane Proteins Incorporated into Giant Unilamellar Vesicles, *Biophysical Journal*, 2005, **88**, 1134-1142.
- [14] M.C. Peterman, J.M. Ziebarth, O. Braha, H. Bayley, H.A. Fishman, and D.M. Bloom, Ion Channels and Lipid Bilayer Membranes Under High Potentials Using Microfabricated Apertures, *Biomedical Microdevices*, 2002, **4**, 231-236.
- [15] K. Ulbrich and V. Šubr, Polymeric anticancer drugs with pH-controlled activation, *Advanced Drug Delivery Reviews*, 2004, **56**, 1023-1050.
- [16] J. Mönkkönen, J. Liukkonen, M. Taskinen, T.D. Heath, and A. Urtti, Studies on liposome formulations for intra-articular delivery of clodronate, *Journal of Controlled Release*, 1995, **35**, 145-154.
- [17] J.C.M. Lee, H. Bermudez, B.M. Discher, M.A. Sheehan, Y.Y. Won, F.S. Bates, and D.E. Discher, *Biotechnol. Bioeng.*, 2001, **73**, 135.

CHAPTER EIGHT

CONCLUSIONS AND OUTLOOK

We present and discuss some perspectives about improvements and further developments of the drug delivery system developed during this project.

8.1 Conclusions

We have successfully developed a spherical hybrid vehicle that could potentially be used for drug delivery, diagnostics purposes, and sensing applications. This vehicle consists of a 1 μm polymeric scaffold in which a submicron hole was realized using FIB drilling and further sealed with a lipid membrane that was functionalized with a MscL channel protein. We have demonstrated that such a hybrid system is remarkably stable, and believe that it may be a potential candidate for various clinical applications.

We also developed a hybrid flat platform containing microwells sealed with a bilayer lipid membrane (BiLM). Membrane deposition onto microwells was obtained by collapsing unilamellar vesicles in a controlled fashion using optical tweezers (OT). To the best of our knowledge, this is the first time OT have been used to induce controlled vesicle collapse. Trapping of the vesicles was realized by increasing the refractive index inside the vesicles by loading with glucose. The electrostatic interaction between the negatively charged vesicles and the positively charged substrate facilitated controlled vesicle collapse.

The dimensions of the hole in our system were scaled down to $\sim 1 \mu\text{m}$. The reduction of the free standing membrane area positively influences the membrane stability [1,2]. The sealing membranes remained stable for \sim one week, a significant advance over the stability of a few hours of planar membranes developed so far [1-4]. In all traditional systems, both sides of the compartments separated from the membrane are accessible [5-10]. In our system, the microwells comprise a small and well-defined volume, accessed only from outside the membrane. In such a system, the concept of a defined volume allows optical quantification of a transport process through the membrane.

We successfully demonstrated the functionality of the MscL channel protein incorporated in the sealing membrane, thus forming a very stable proteomembrane. These are the first experiments to include a protein in such synthetic structures and demonstrate controlled release. Kinetic measurements demonstrated rapid dye diffusion with a time constant $\tau \sim 1000 \text{ s}$. Comparison of the experimental data with an analytical diffusion model and a FEMLAB simulation model indicates that the diffusion most probably occurred through a single MscL channel protein. This agrees well with the electrophysiological measurements indicating that MscL channels in the “active” state are open for 25% of the time.

We were able to reproducibly control the activity of MscL, which remained stable for several days, by switching it on- and off in a cyclic fashion, a property relevant for controlled drug delivery in nanodevices. This hybrid platform is unique, and has significant potential as a high throughput assay system.

We realized, for the first time to our knowledge, single nanoholes on a polystyrene microscaffold using focused ion beam drilling. We found single holes could be etched in a controllable way both in number and size. We also drilled single square holes of desired dimensions varying from 30 to 500 nm on several polystyrene scaffolds. A linear behavior between the etched surface area and etching time was found, providing information about the polystyrene scaffold etching. This allows prediction of etching time for a given hole surface area and wall thickness.

Finally a self-standing spherical hybrid nanodevice was successfully developed by combining an impermeable polystyrene scaffold with a single hole sealed with a lipid membrane where MscL channel protein was embedded. The scaffold loading, biomodification, and channel protein gating were performed in a controllable fashion. We were able to load the hydrophobic scaffolds with hydrophilic solution, indicating that in principle many different types of drugs could be used. The hybrid vehicle remained stable for more than 2 weeks. We deliberately triggered the MscL protein activity, inducing a controlled loading/release through the MscL nano-valve.

8.2 Outlook

We discuss some aspects aimed at the improvement and further development of our hybrid systems and possible applications.

8.2.1 Improvement of the throughput

Because of the serial nature of preparation of our hybrid drug delivery vehicle (DDV), the throughput is relatively low. For *in vitro* experiments and especially for real drug delivery applications, a much higher throughput is needed.

Scaffold fabrication

Massively parallel fabrication of scaffolds with holes could be achieved using an automated FIB drilling process. A requirement to use this procedure is that etching parameters such as etching area and time, and lateral spacing between scaffolds should be known. Etching area and time can be determined based on the results achieved in Chapter 6. Well-defined lattice spacing could be realized by fabricating a substrate with a regular pattern of wells where scaffolds physically align themselves, e.g. due to gravity. Preliminary tests indicated a preference of the scaffolds to align in the wells, as shown in Figure 8.1.A. Another possibility to pattern the scaffolds on a surface is by means of chemical bonding between the scaffolds and gold spots patterned on the substrate (see Figure 8.1.B). By breaking this chemical bonding, e.g. upon pH change, release of scaffolds from the surface could be achieved.

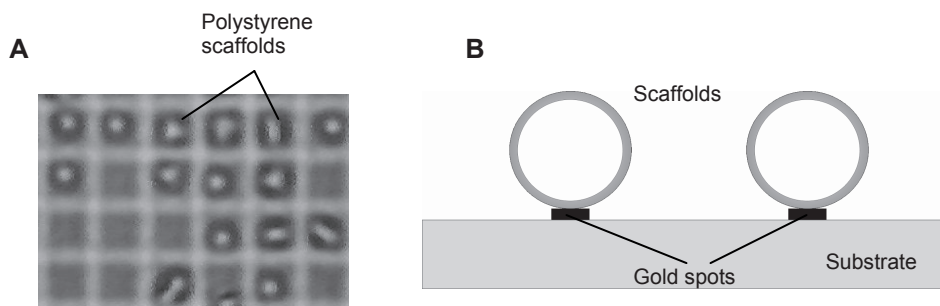


Figure 8.1. (A) Pattern of polystyrene scaffolds (diameter $\sim 1 \mu\text{m}$) aligned in the microwells. Hole-to-hole distance is $4 \mu\text{m}$. (B) Schematic of scaffolds bound chemically on patterned spots on a flat substrate.

The abovementioned automated FIB drilling process is suited to increase the throughput for *in vitro* experiments. Although the throughput in this way can be significantly improved, compared to the need in real drug delivery applications a long processing time is required for producing sufficiently large numbers of scaffolds and the associated costs are very high (e.g. to produce 10^6 scaffolds with holes, ~ 11 days FIB processing time could be required by considering 1 s etching time per hole, and the cost could be a few tens of thousands euro). Therefore, a bulk production of the scaffolds with holes and low cost production is needed. An alternative way to the FIB drilling might be a chemical method. One possibility could be to grow polymeric scaffolds on pillars (see Figure 8.2) upon swelling a polymer film; subsequent release would result in free scaffolds with holes, improving in this way the scaffold throughput. An additional method could be to use solvents to make pores in the nonporous scaffolds produced.

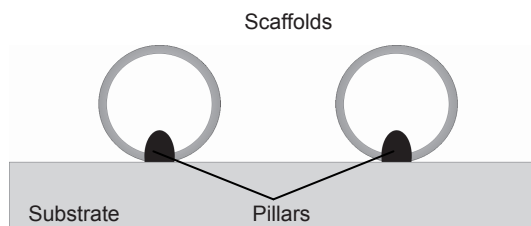


Figure 8.2. Schematic representation of grown polymeric scaffolds with single holes.

Membrane deposition

So far we used optical tweezers manipulation to induce vesicle collapse on a hole in the conditions of a low free vesicle collapse. An easy and fast way to deposit membrane on several holes is to directly use the free collapse of the vesicles. This could be achieved by proper selection of lipid composition. In Chapter 3, different vesicle compositions were investigated, where Asolectin based vesicles demonstrated a significant uncontrolled collapse. By producing Asolectin based giant vesicles and flowing them on the substrate with holes or arrays of scaffolds with holes could result in fast membrane deposition onto multiple holes. As a result, the throughput for membrane deposition could be improved.

Biomolecule concentration

We observed that the probability of having a channel protein in the membrane sealing a hole in the polystyrene scaffold was very low. This problem could be

solved by increasing the protein concentration in the vesicles. Another possibility could be to first seal the holes with bare lipid membranes and fuse to such membranes small vesicles having a high protein concentration. In this way, the protein incorporation in the sealing membrane could be enhanced.

8.2.2 Further development of the spherical hybrid vehicle

To further improve the performance of our spherical hybrid vehicle, its biofunctionality could be further enhanced, e.g. by adding the targeting and microcirculation ability to this system. Targeting could be realized by adding specific biomolecules such as antibodies that recognize specific molecules on a target cell. The microcirculation could be realized by combining energy producing biomolecules with motor proteins that convert the energy into mechanical movement. For example, incorporation of photosynthetic complexes in the membrane could create a protonation (H^+) gradient inside the vehicle. The embedded ATPase (a rotary enzyme) in the membrane can utilize this gradient and produce ATP. A flagellar motor incorporated in the membrane could consume the locally produced ATP and perform mechanical movements, thereby pulling the vehicle with it.

Additional improvements for *in vivo* applications include the use of biodegradable scaffolds with a tunable biodegradation rate and bioinert surfaces. Biodegradability allows clearance of the degraded molecules by the reticulo-endothelial system (RES). The bioinert surface could be provided by coating the vehicle surface with polyethylene glycol polymer to prevent its recognition by the RES system.

Our nanodevice is a robust system that could potentially be used for drug delivery applications in clinical settings. For example, by incorporating in the membrane a pH-sensitive channel protein, a controlled release from the vehicle by ambient pH change could occur when targeting tumor tissue, where the pH around the tumor is lower than the physiological pH (pH 7.4) [11].

8.2.3 Hybrid flat platforms

New developments

An additional configuration of a flat substrate containing microwells is presented in Figure 8.3.A. It consists of a glass support that is covered with a metal layer, e.g. titanium and a polystyrene insulating layer deposited on top.

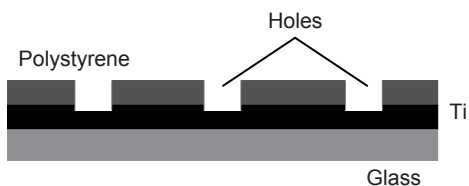


Figure 8.3. Schematic of a new flat substrate configuration.

Microwells are etched through the polystyrene layer. This configuration could enable the combination of optical imaging and electrophysiological measurements to monitor transport through the membrane that seals the microwells. The metal layer can be connected with one of the electrodes and the current can flow only through the holes. Attempts for realization of this structure have been made and the fabricated substrates are presented in Appendix C.

Applications of hybrid flat platforms as an assay system

In Chapter 5 we showed protein functionality in our hybrid flat substrate. The conformational changes of the protein, resulting in formation of a pore, were induced by the pH environmental changes from outside the well. The method allowed optical quantification of the diffusion through the protein. Extending this idea to a chambered system that has multiple compartments (see Figure 8.4) could allow multiple detection of protein conformation changes triggered by multiple external changes. For example, varying the pH change for different

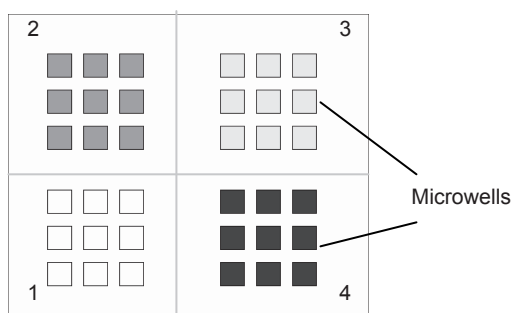


Figure 8.4. Schematic of a hybrid flat substrate for assay applications. In four compartments, different colors of the wells represent different concentration of a solute diffused from the bulk into the microwells.

compartments could yield different behaviors of protein functionality, such as size of pore opening, time interval of opening, range of the pH that causes protein conformational changes, etc., that reflects the rate of diffusion in the microwells. A microfluidic flow cuvette could be used to simultaneously and independently flow solutions with different pH through different chambers. Integration of hybrid flat substrates with the microfluidic flow cuvette could suppress the membrane disturbances from the bulk medium, increasing the membrane stability. Also, a much smaller sample volume is required and the flow process can be faster and more reliable. Instead of a pH change, a cell could be brought in close contact with the membrane to probe a specific interaction and monitor any possible exchange between them.

References

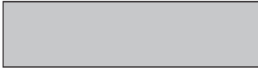

- [1] J. Schmidt, Stochastic sensors, *Journal of Materials Chemistry*, 2005, **15**, 831-840.
- [2] M. Mayer, J.K. Kriebel, M.T. Tosteson, and G.M. Whitesides, Microfabricated Teflon Membranes for Low-Noise Recordings of Ion Channels in Planar Lipid Bilayers, *Biophysical Journal*, 2003, **85**, 2684-2695.
- [3] M.C. Peterman, J.M. Ziebarth, O. Braha, H. Bayley, H.A. Fishman, and D.M. Bloom, Ion Channels and Lipid Bilayer Membranes Under High Potentials Using Microfabricated Apertures, *Biomedical Microdevices*, 2002, **4**, 231-236.
- [4] C. Schmidt, M. Mayer, and H. Vogel, A Chip-Based Biosensor for the Functional Analysis of Single Ion Channels, *Angew. Chem. Int. Ed.*, 2000, **39**, 3137-3140.
- [5] W. Hanke and W.-R. Schlue, *Planar Lipid Bilayers: Methods and Applications*, ed. D.B. Sattelle, Academic Press Limited, London, ISBN 0-12-322994-4, 1993.
- [6] W.A. Vercoutere, S. Winters-Hilt, V.S. DeGuzman, D. Deamer, S.E. Ridino, J.T. Rodgers, H.E. Olsen, A. Marziali, and M. Akeson, Discrimination among individual Watson-Crick base pairs at the termini of single DNA hairpin molecules, *Nucleic Acids Research*, 2003, **31**, 1311-1318.
- [7] L.-Q. Gu, O. Braha, S. Conlan, S. Cheley, and H. Bayley, Stochastic sensing of organic analytes by a pore-forming protein containing a molecular adapter, *Nature*, 1999, **398**, 686-690.
- [8] J.J. Kasianowicz, E. Brandin, D. Branton, and D.W. Deamer, Characterization of individual polynucleotide molecules using a membrane channel, *Proc. Natl. Acad. Sci. USA*, 1996, **93**, 13770-13773.
- [9] A. Meller, L. Nivon, E. Brandin, J. Golovchenko, and D. Branton, Rapid nanopore discrimination between single polynucleotide molecules, *Proc. Natl. Acad. Sci. USA*, 2000, **97**, 1079-1084.
- [10] B. Baumeister, N. Sakai, and S. Matile, Giant artificial ion channels formed by self-assembled, cationic rigid-rod β -barrels, *Angew. Chem.*, 2000, **112**, 2031-2034.
- [11] K. Ulbrich and V. Šubr, Polymeric anticancer drugs with pH-controlled activation, *Advanced Drug Delivery Reviews*, 2004, **56**, 1023-1050.

APPENDICES

Appendix A

Fabrication of flat Pyrex substrates

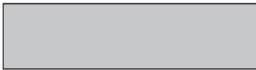

Samples containing arrays of microwells were prepared based on RIE technique as follows:

1. Starting with a 4" Pyrex wafer. (1) 
2. Standard cleaning (cleaning with acid solution and rinsing with de-ionized water (DI))
3. Photolithography, including following steps:
 - Baking 120 °C for 10 min.
 - Vapour HMDS
 - Apply Photo resist olin 908/35 at 1000 rpm for 30 sec.
 - Prebake 10 min. at 50 °C
 - Exposure 30 sec.
 - Development 50 sec.(30 sec 1, 20 sec. 2)
 - Quick dump rinse
 - Microscope check
 - Additional development depending on result of microscope check.
 - Postbake 5 min. 95 °C followed by 30 min. 110 °C
 - Microscope check
4. Dry etching (machine plasma therm 790) using parameters as follows:
CHF₃: 27; O₂: 3
Power: 350 (4) 
Pressure: 20 mTorr
Temperature: 20 °C
Etching time: 8 hours
5. Dicing of the wafer applying these steps:
 - Application of a dicing foil on both sides of the wafer
 - Dicing in 4 parts
 - Removal of dicing foil backside
6. Measuring substrate thickness:
 - HF etching for 20 min
 - Measuring substrate thickness
 - HF etching for the needed thickness
 - Measuring substrate thickness
 - HF etching for the needed thickness
7. Removal of the dicing foil on the front side with acetone and 100% HNO₃
 - Application of dicing foil to the backside
 - Dicing in the given dimension
 - Removing dicing foil and package for delivery

Appendix B

Silicon sample with a single hole

An insulating Si_3N_4 layer of thickness 170 nm was deposited on the top of a silicon wafer (thickness $\sim 525 \mu\text{m}$). A square region of the silicon wafer was etched until reaching the insulating layer. The thinned platform area was $\sim 80 \times 80 \mu\text{m}^2$. The sample was further oxidized to facilitate chemical surface modification. The recipe for sample processing is presented below.

Process	Parameters	
Substrate selection - Silicon <100> DSP	<ul style="list-style-type: none"> • Diameter: 100 mm • Thickness: $525 \mu\text{m} \pm 25 \mu\text{m}$ • Resistivity: 5 - 10 Ωcm • Type: p 	
Standard cleaning	<ul style="list-style-type: none"> • Fuming HNO_3 (100%): 5 min • Fuming HNO_3 (100%): 5 min • Quick Dump Rinse • Boiling 95°C HNO_3 69%: 10 min • Quick Dump Rinse 	
Etching HF (1%) Native Oxide	<ul style="list-style-type: none"> • Etch time: ~ 1 min • Quick Dump Rinse 	
LPCVD Si_3N_4 deposition- low stress Thickness = 170 nm	<ul style="list-style-type: none"> • SiH_2Cl_2 flow: 70 sccm (standard cubic centimeters per minute) • NH_3 flow: 18 sccm • Temperature: 850°C • Pressure: 200 mTorr 	
Photolithography Bottom side	<ul style="list-style-type: none"> • Vapour HexaMethylDiSilazane (HMDS) • Dehydration bake (120°C): 5 min • Apply photoresist Olin 907-17 at 4000 rpm • Prebake: 90 s at 95°C • Exposure Time: 6 s • Development: 30 s beaker 1, 15 - 30 s beaker 2 • Quick Dump Rinse • Postbake: 30 min at 120°C 	
Plasma etching Si_3N_4	<ul style="list-style-type: none"> • Electrode temp.: 10°C • CHF_3 flow: 25 sccm 	

Bottom side

- O₂ flow: 5 sccm
- Pressure: 10 mTorr
- Power: 75 W
- Etch rate SiN = 50 nm/min (for V_{DC}=-460V)

Stripping of Olin PR - standard

- Time: 20 min
- Visual microscopic inspection

HF Etching (1% Native Oxide)

- Etch time: > 1min

Etching of Silicon by KOH - standard
t = 530 min

KOH:DI = (1:3): 25 wt% KOH: 500 g KOH in 1500 ml DI water

- Temperature: 75 °C
- Etch rate Si <100> = 1µm/min



Cleaning RCA-1 (NH₄OH/H₂O₂/H₂O)

NH₄OH:H₂O₂:H₂O (1:1:5) vol%

- Temperature 70 - 80 °C
- Max. cleaning time 10 min

Standard cleaning See 2nd step

Wet Oxidation of Silicon at 1150°C

- Temperature: 1150 °C
- Gas: H₂O + N₂
- t = 1 hr

PECVD of SiO₂

Parameters:

- Electrode temp. = 300 °C
- 2% SiH₄/N₂ flow = 200 sccm
- N₂O flow = 710 sccm
- Pressure = 650 mTorr
- Power = 60 W
- Deposition rate = 37 nm/min

Top side
t = 30 s

Appendix C

C.1 Additional FIB – processed structures

In addition to polystyrene, scaffolds based on hollow glass (HG) beads were fabricated using focused ion beam drilling. They are optically transparent and enclose a larger inner volume compared to the hollow polystyrene scaffolds. HG scaffolds are interesting as self-standing spherical structures for the study of protein conformational changes, looking at the transport of molecules through the membrane that seals the hole, and drug delivery (*in vitro* [1] and oral [2]) applications.

Arrays of holes in a polystyrene coated substrate were also fabricated using FIB drilling. The aims of preparing this structure included obtaining additional information on the etching rate of polystyrene when using high etching currents for different hole sizes through a thick polystyrene layer, and exploring the reproducibility of hole etching using FIB drilling, relevant for automated fabrication of HPS scaffolds arranged on a predefined pattern. A feature of the FIB equipment is that the etching process can be performed automatically when programmed via the software. In this way, defining certain etching parameters such as etching area and time as well as the lateral spacing between holes, hole arrays can be drilled in an automated way. Third, this structure could facilitate the use of both optical and electrophysiological measurements, enabled by the transparency of the sample and the presence of the metal layer at the bottom of the hole, to observe any ionic transport through the membrane that covers the hole.

C.2 Materials and methods

Sample preparations

Hollow glass scaffolds. Hollow glass (HG) beads were purchased as powder form Polysciences (Warrington, PA, USA). They are polydisperse, with diameter variations from sub-micrometer to more than 30 μm (see Figure 1).

Cross-sectional profiles of different beads showed a variation in the wall thickness from 200 nm for small beads to $\sim 2 \mu\text{m}$ for big beads. The same supports as in the case of HPS beads were used for supporting the HG beads. The sample was prepared by mixing a small amount of bead powder (< 1 gram) with ~ 1.5 ml water. A small droplet of this dilution was placed on the centre of the sample and left there to dry at the room temperature (24 $^{\circ}\text{C}$). After drying, the beads maintained their position upon reincubation in water.

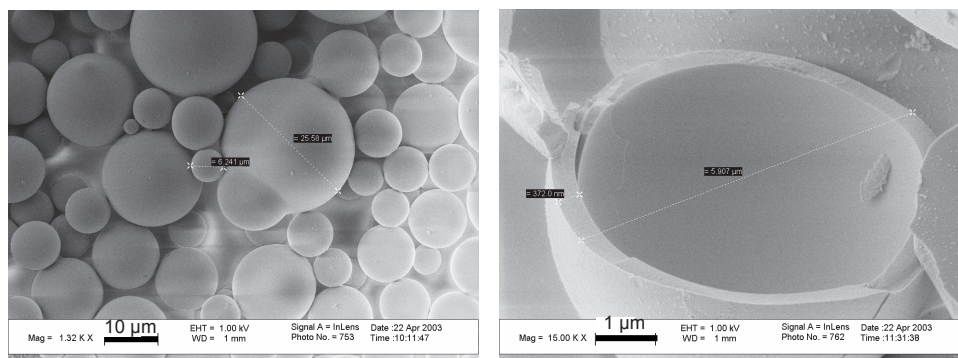


Figure 1. SEM image of (left) polydispersed HG beads and (right) a mechanically broken hollow glass bead (diameter of 5.9 μm and wall thickness of ~ 370 nm) supported on a Silicon substrate.

Flat polystyrene substrates. A thin Ti layer (10 to 40 nm) was deposited on a round coverslip glass (thickness of 170 μm). Poly(styrene) polystyrol material ($[-\text{CH}_2\text{CH}(\text{C}_6\text{H}_5)-]_n$, Janssen Chimica, Tilburg, The Netherlands) was dissolved in toluene at a concentration of 12% (w/w). A homogeneous polystyrene layer of 1 μm thickness was deposited on the top of the Ti layer by spin-coating 0.5 ml polystyrene solution at 5000 rpm for about 30 seconds. The layer thickness was estimated using a spectrophotometer (UV-2401PC, Shimadzu, Japan) by measuring the transmittance spectrum of the polystyrene layer [3].

FIB processing

In the case of HG scaffolds, an etching current varying from 48 to 350 pA was used to etch single holes. FIB was also used to make series of holes of desired sizes and lateral spacing, in the polystyrene-Ti coated sample. The polystyrene was etched until the Ti layer was exposed. Low currents (1 to 11 pA) were used to enhance control during etching. The etching was performed either in series mode (i.e. milling each hole completely one by one) or automatically in parallel mode (etching stepwise repeatedly from every hole until all the polystyrene material from the hole region was etched away). The second procedure enables a faster array processing due to the automated operation.

C.3 Results

Hollow Glass scaffolds. Figure 2 shows a glass scaffold where a single hole was etched. The time required to etch a $1.25 \times 1.25 \mu\text{m}^2$ hole was ~ 2 min using a

current of 48 pA. Etching of holes was controllable in number and size and scaffolds were stable. Single square holes with a size varying from 1 to 3 μm were drilled on several HG scaffolds (see Figure 3).

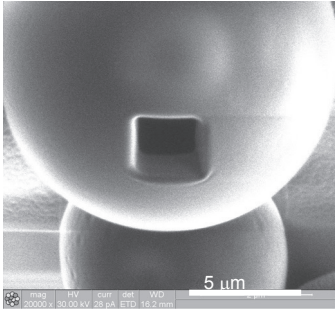


Figure 2. SEM image of a HG scaffold with an outer diameter $\sim 6.3 \mu\text{m}$ and wall thickness $\sim 0.56 \mu\text{m}$, in which a single square hole ($1.25 \times 1.25 \mu\text{m}^2$) was drilled. Etching current was 48 pA and the etching time was 2 minutes.

For a given hole size, the etching time on different scaffolds was not predictable due to the variety on their wall thickness (see Figure 3). Etching time could also be influenced by the charging effect associated with beam deflections or drifting of the scaffold, resulting in a longer etching time (see Figure 3.B). Glass scaffolds showed a higher instability than polystyrene scaffolds, which may be due to high etching currents ($> 93 \text{ pA}$) used for glass scaffolds, resulting in a surface charging.

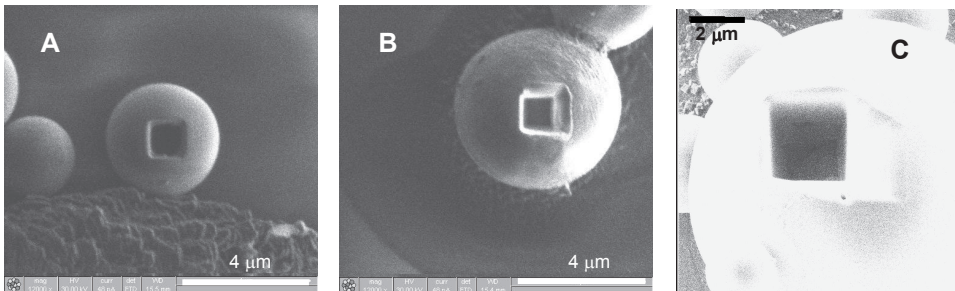


Figure 3. FIB images of HG scaffolds in which single square holes were drilled. (A) $\Phi_{\text{HG}} \sim 3.6 \mu\text{m}$, $d_{\text{wall}} \sim 0.2 \mu\text{m}$, $t_{\text{etch}} \sim 1 \text{ minute}$, $S_{\text{hole}} \sim 1 \times 1 \mu\text{m}^2$, $I_{\text{etch}} \sim 48 \text{ pA}$. (B) $\Phi_{\text{HG}} \sim 5.4 \mu\text{m}$, $d_{\text{wall}} \sim 0.4 \mu\text{m}$, $t_{\text{etch}} \sim 4 \text{ minutes}$, $S_{\text{hole}} \sim 1 \times 1 \mu\text{m}^2$, $I_{\text{etch}} \sim 48 \text{ pA}$. (C) $\Phi_{\text{HG}} \sim 14 \mu\text{m}$, $d_{\text{wall}} \sim 2 \mu\text{m}$, $S_{\text{hole}} \sim 3 \times 3 \mu\text{m}^2$, $t_{\text{etch}} \sim 20 \text{ min}$: during the first 5 min $I_{\text{etch}} \sim 150 \text{ pA}$ was used and for the other 15 min I_{etch} was 350 pA. Φ_{HG} , d_{wall} , S_{hole} , I_{etch} , t_{etch} denote the outer diameter of the hollow glass scaffold, wall thickness, hole size, etching current, and etching time, respectively.

Flat polystyrene substrates. Figure 4 shows a flat polystyrene sample containing an array of 7×7 holes etched in series. The average time required to etch a single hole of $200 \times 200 \text{ nm}^2$, using a current of 4 pA, was ~ 47.5 seconds. We gained information on the etching rate of polystyrene by measuring the time required to etch through the polystyrene layer until reaching the Ti. The time required to etch a $200 \times 200 \text{ nm}^2$ hole through a $1 \mu\text{m}$ polystyrene layer was ~ 5 minutes, 47.5 seconds, and 12 seconds using a current of 1, 4, and 11 pA, respectively. For a $400 \times 400 \text{ nm}^2$ hole, the time required was 5 minutes and 54 seconds by etching with a current of 4 pA and 11 pA, respectively. The variations in etching time for the same hole areas was $< 4\%$, indicating good reproducibility. An array of $200 \times 200 \text{ nm}^2$ holes (7×7) was also etched using parallel mode, i.e. a software-automated procedure. The etching results were similar with the case when series mode was used, whereas the total etching procedure was faster.

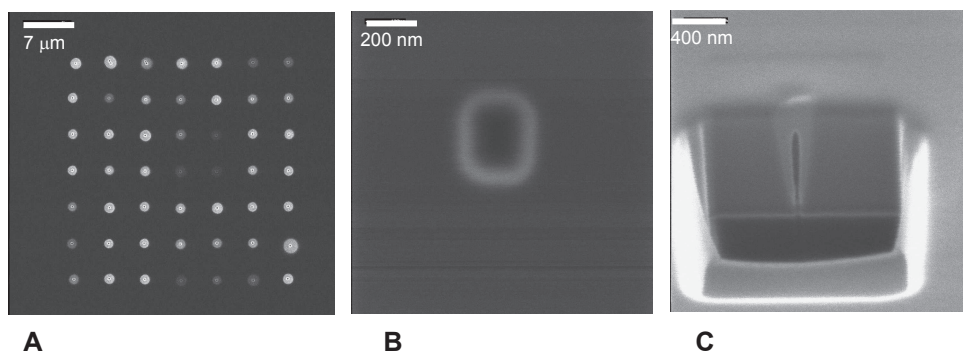


Figure 4. FIB image of (A) a flat substrate coated with a $1 \mu\text{m}$ thick polystyrene layer where an array of square holes (size of $200 \times 200 \text{ nm}^2$, hole-to-hole center spacing of $5 \mu\text{m}$) were etched in series mode. Etching current was 4 pA and the average etching time per hole was 47.5 seconds. Note the charging of the polystyrene around the hole, indicated by the white spots, known as ‘Halo’ effect. (B) Zoom in of a single hole in (A). (C) Depth profile of the hole in (B) filled with gallium, etched half-width vertically and rotated under an angle.

References

- [1] M.H. Cohen, K. Melnik, A.A. Boiarski, M. Ferrari, and F.J. Martin, Microfabrication of Silicon-Based Nanoporous Particulates for Medical Applications, *Biomedical Microdevices*, 2003, **5 (3)**, 253-259.
- [2] M. Ferrari, P.J. Dehlinger, F.J. Martin, C.F. Grove, and D.R. Friend, Particles for Oral Delivery of Peptides and Proteins, US Patent No. 6,355,270, March 12, 2002.
- [3] J.S. Kanger, Waveguide Spontaneous and Coherent Raman Spectroscopy on (Bio)Molecules at the Surface, *Ph.D. Thesis*, 1996, University of Twente.

Appendix D

Color figure

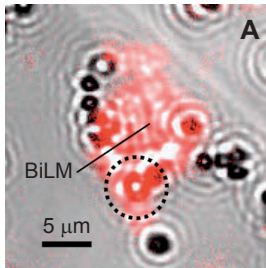


Figure 7.6. (A) CLSM image of a DiA labeled lipid membrane patch deposited on the hole ($300 \times 300 \text{ nm}^2$) of the scaffold immersed in buffer solution. The scaffold of interest is enclosed by the dashed circle.

Summary

In medical science and health care, development of new approaches to specifically treat a disease without damaging healthy tissue is of high importance. In this context, the use of drug delivery vehicles that can recognize a disease cell and can specifically and locally deliver a therapeutic agent to that cell offers a good perspective. In this thesis we present the design, fabrication, and characterization of a new hybrid vehicle for controlled drug delivery.

In Chapter 1, the design of such a hybrid vehicle is presented. The new hybrid vehicle is based on a spherical polymeric scaffold with micrometer dimensions that contains a nanohole that is sealed with a biofunctional membrane. The scaffold can contain e.g. a drug, while the nanohole and the biofunctionalised membrane facilitate the controlled release and can potentially be used for specific targeting. Before the final hybrid vehicle was realized, we first developed a hybrid flat platform consisting of arrays of microwells in a flat Pyrex substrate sealed with a biofunctional membrane in order to explore the system properties.

In Chapter 3 methods to deposit a bilayer lipid membrane (BiLM) onto a microwell are explored. It was found that the use of vesicle collapse was most successful. Collapse of negatively charged unilamellar lipid vesicles on positively (using PLL) charged surfaces showed a fast and efficient membrane formation facilitated by the electrostatic interaction of the vesicles with the surface. The method generated a BiLM with a uniform thickness of ~ 6 nm.

In Chapter 4, the realization of the flat platform containing microwells sealed with a stable bilayer lipid membrane is reported. We used optical tweezers (OT) for vesicle manipulation and controlled collapse of vesicles onto microwells in a PLL coated substrate. Epifluorescence and TIRF measurements showed a total vesicle collapse and a fast dynamics of the collapse process, with a time constant ~ 200 ms. A good seal of microwells is demonstrated using vesicles composed of DPhPC-POPG-Cholesterol lipids (70:25:5% wt.-%). The membrane showed a temporal stability of more than one week. This extremely high stability is associated to the small hole size of the microwell.

The successful incorporation of an MscL channel protein into the membrane is presented in Chapter 5. The controlled load/release of calcein from the microwell through MscL channel protein is observed by using MTSET, a small molecule that triggers the opening of the channel protein. Fluorescent measurements showed rapid calcein diffusion with a time constant $\tau \sim 1000$ s. Data analysis yielded a $n_{\text{on}} = 0.25$, indicating that the diffusion most probably occurred through a single MscL

channel protein that remains open for ~ 25% of the time interval. This value is close to the one found from electrophysiological measurements analysis. The remote switching on-and-off of MscL nanovalve activity is demonstrated when MTSET-and-DTT was added outside the microwell.

In Chapter 6, the fabrication of the spherical polymeric scaffold is presented. The controlled fabrication of nanoholes in hollow polystyrene scaffolds (outer diameter ~ 1 μm and wall thickness ~ 100 nm) is realized by using a focused ion beam. Single square holes of desired dimensions varying from 30 to 500 nm are drilled on several polystyrene scaffolds in 2 to 70 seconds per hole respectively using the lowest beam currents (1.5 pA). A linear behavior between the etched surface area and etching time is found.

The realization of the novel hybrid vehicle is reported in Chapter 7. In this work, loading of the scaffold through the fabricated nanohole, hole sealing with a proteomembrane, and MscL channel protein activation are described. The addition of 2% ethanol in the aqueous dye solution outside the HPS scaffold resulted in loading of the scaffold. The polystyrene scaffolds were found to be impermeable for small fluorophores.

We sealed the nanohole with an artificial lipid membrane containing functional MscL channel proteins. The proteomembrane remained remarkably stable for more than 2 weeks until deliberately rupturing the membrane by adding Triton. A controlled load and release of solutes in or out of the sealed scaffold is realized through the protein nanovalve by adding MTSET outside the scaffold to activate the protein.

In Chapter 8, conclusions about the development of the hybrid structures, their applications, improvements and future developments are presented.

Samenvatting

De ontwikkeling van nieuwe methoden om zeer specifiek ziekten te genezen zonder daarbij schade aan gezond weefsel aan te richten is een belangrijk aandachtsgebied binnen de medische wetenschap en de gezondheidszorg. Het gebruik van medicijn afgifte systemen die zieke cellen in het lichaam herkennen en vervolgens specifiek en lokaal medicijnen afgeven bieden hierin een goed perspectief. In dit proefschrift wordt het ontwerp, de realisatie en de karakterisatie van een nieuw hybride systeem voor medicijn afgifte gepresenteerd.

In hoofdstuk 1 wordt het ontwerp van een dergelijk hybride systeem gepresenteerd. Het systeem is gebaseerd op een micrometer grote polymeer capsule die een nanometer grote opening bevat welke is afgesloten met een gefunctionaliseerd membraan. Daar waar de capsule bijvoorbeeld een medicijn kan bevatten maakt de opening met het membraan de gecontroleerde afgifte van het medicijn mogelijk. Voordat het uiteindelijke ontwerp van het hybride systeem gerealiseerd is, is eerst een vlakke variant van dit systeem gemaakt. Deze bestaat uit een matrix van microgaatjes in een pyrex substraat afgesloten met een membraan. Dit systeem is vervolgens gebruikt om de systeem eigenschappen te bestuderen.

In hoofdstuk 3 zijn verschillende methoden voor het aanbrengen van membranen op de microgaatjes in het substraat onderzocht. De methode die het beste resultaat geeft is gebaseerd op het laten openspringen van lipide vesicles op het substraat. Het gebruik van negatief geladen enkel laag lipide vesicles in combinatie met een positief geladen substraat (d.m.v. PLL) laat, vanwege de electrostatische interactie tussen vesicle en substraat, een snelle en efficiënte membraan formatie zien. Met deze methode worden dubbellaags lipide membranen gevormd met een uniforme dikte van ~ 6 nm.

Hoofdstuk 4 beschrijft de realisatie van de pyrex substraten met daarin de microgaatjes en het afsluiten van de microgaatjes met behulp van een membraan. Er wordt gebruik gemaakt van een optische pincet voor het manipuleren van de lipide vesicles en het gecontroleerd laten openspringen van de vesicles op een microgaatje in het met PLL gecoat substraat. Epifluorescentie en TIRF metingen laten zien dat het openspringen van de vesicles een snelle dynamica heeft (tijdsconstante ~ 200 ms) en dat de vesicle zich volledig ontvouwd op het substraat. Een goede afdichting van het microgaatje door het membraan is verkregen bij het gebruik van vesicles gemaakt van DPhPC-POPG-Cholesterol lipiden (70:25:5% wt.-%). Het membraan

bleek stabiel voor meer dan een week. Deze extreem hoge stabiliteit wordt toegedicht aan de kleine dimensies van het microgaatje.

Het succesvol inbrengen van een MscL kanaal eiwit in het membraan wordt beschreven in hoofdstuk 5. Experimenten tonen aan dat door gebruik te maken van MTSET, een klein molecuul die het kanaal van het MScL eiwit opent, het mogelijk is om op een gecontroleerde manier het microgaatje te vullen met calcein. Ook is het mogelijk om op deze manier calcein gecontroleerd te laten ontsnappen uit het microgaatje. Fluorescentie metingen geven een tijdsconstante van ~ 1000 s voor de diffusie van calcein uit het microgaatje. Data analyse geeft vervolgens een $n_{\text{open}} = 0.25$, wat betekent dat de diffusie van calcein heeft plaatsgevonden door slechts een enkel MScL eiwit die gedurende 25% van de tijd "open" staat. Deze waarde licht dicht bij waarden die gevonden zijn door middel van electrophysiologische metingen aan hetzelfde molecuul. Het herhaaldelijk openen en dichtens van het MScL kanaal wordt gedemonstreerd door middel van het toevoegen van MTSET en DTT.

In hoofdstuk 6 wordt de fabricage van de sferische polymeer capsule beschreven. Een "focussed ion beam" is gebruikt om openingen in holle polystyreen bolletjes (diameter 1 micrometer, wanddikte 100 nm) te maken. Vierkante gaatjes met afmetingen variërend van 30 tot 500 nm zijn geëtsd in 2 respectievelijk 70 seconden bij een zeer lage ionen stroom (1.5 pA). Er is een lineair verband gevonden tussen het oppervlak van het gaatje en de tijd die nodig is om het gaatje te etsen.

Tenslotte wordt in hoofdstuk 7 de realisatie van het nieuwe hybride systeem gepresenteerd. Het laden van de capsule door de nanometer opening, het afdichten van de opening met een membraan, en het functionaliseren van het membraan met behulp van een MScL kanaal eiwit worden beschreven. Om de holle polystyreen capsules te vullen met een waterige oplossing is 2% ethanol toegevoegd. De wanden van de capsule bleken niet permeabel voor kleine fluorescerende molekulen.

De opening in de capsule is vervolgens afgedicht met een lipide membraan die MScL eiwitten bevat. Het membraan was zeer stabiel voor meer dan twee weken totdat het membraan opzettelijk kapot werd gemaakt met behulp van Triton. Tenslotte laat dit hoofdstuk zien hoe op een gecontroleerde wijze door middel van het MScL eiwit en MTSET stoffen geladen en afgegeven kunnen worden in of uit de capsule.

In hoofdstuk 8 worden de conclusies gegeven en tevens de toepassingen van de ontwikkelde hybride systemen, mogelijke verbeteringen en toekomstige ontwikkelingen besproken.

List of abbreviations

AFM	atomic force microscopy
BiLM	bilayer lipid membrane
BLM	black lipid membrane
CLSM	confocal laser scanning microscopy
DDV	drug delivery vehicle
DNA	deoxyribose nucleic acid
DPHPC	1,2-Diphytanoyl-sn-Glycero-3-Phosphocholine
DTT	dithiothreitol
FIB	focused ion beam
GUV	giant unilamellar vesicle
Hepes	4-(2-Hydroxyethyl)piperazine-1-ethanesulfonic acid
HG scaffold	hollow glass scaffold
HPS scaffold	hollow polystyrene scaffold
NA	numerical aperture
MscL	mechanosensitive channel of large conductance
MTSET	[2-(trimethylammonio)ethyl]methanethiosulfonate
OT	optical tweezers
OPOE	N-Octyl-oligo-oxyethylene
PA	1-Stearoyl-2-Oleoyl-sn-Glycero-3-Phosphate
PBS	phosphate buffered saline
PEG	polyethylene glycol
PLL	poly-L-lysine hydrobromide
PMMA	poly(methyl methacrylate)
POPG	1-Palmitoyl-2-Oleoyl-sn-Glycero-3-[Phospho-rac-(1-glycerol)]
PS	polystyrene
RES	reticulo-endothelial system
RIE	reactive ion etching
RNA	ribonucleic acid
SDS	sodiumdodecylsulphate
SFM	scanning force microscopy
SEM	scanning electron microscope
TIRF	total internal reflection fluorescence

Acknowledgments

Finally, I have come to the end of my thesis. I would like to acknowledge many people who supported me during this project. My deepest gratitude goes to:

My supervisor Hans Kanger for guiding me throughout the thesis work, valuable suggestions, fruitful discussions, tactful and respectful supervision.

My promoter Vinod Subramaniam for his enormous support, enthusiasm about the project, and kind assistance during the writing of this thesis.

Jan Greve for his optimism and continuous encouragement at the beginning of this project.

Dr. Armağan Koçer from BioMaDe Technology Foundation for her great work on MscL, her support and enthusiasm about this project, long working evenings, and social talks.

My special thanks to Henk-Jan van Manen for his assistance with CLSM; Anthony de Vries and Tomasz Bak for preparing the metal coated substrates; Kees van der Werf for the AFM work and technical support; Stefan Schlautmann for fabrication of silicon chips; Kirsten van Leijenhorst-Groener and Rolf Vermeij for their assistance in chemical lab; Yanina Cesa for sharing the electrical set-up; Cees Otto for his kind supervision during the preparation of a proposal; Aufried Lenferink for his technical assistance.

I would also like to thank Bert Otter and Vishvas Gadgil for the FIB work, Huib van Vossen from MESA⁺ Institute for kindly supplying the mask used to fabricate the Pyrex substrates; Robert Wijn from Lionix B.V. for fabrication of Pyrex substrates and his kind support in the cleanroom; Michel Duits from Physics of Complex Fluids who kindly provided the rotary evaporator apparatus; Laura Vogelaar from the Membrane Technology Group who kindly supplied the PMMA substrates; Zheng Zhang for the kind collaboration, and Fenghua Meng for the discussions about the project.

My sincere greetings to my roommates Jurgen, Chandrashekhar, Maryana, and Bart, for having a great time; SMD members Mathilde and Marieke for the constructive discussions and sharing the OT set-up; Cytometry group members and Yvonne (G.) for the nice time we had together, especially in France is unforgettable: Lily for the Chinese lessons; Frans for his kindness and '*voor de lekkere thee*'; and finally Sylvia Winters, the most joyful person I have ever known, for her kind assistance and support.

I had a wonderful time and I always enjoyed the discussions, jokes, and parties in the BPE group. Many thanks to the Dutch people for their hospitality, *erg bedankt!*

I am infinitely thankful to my parents and my brother for their love, support, and the joy they brought in my life. I am enormous grateful to my dear Aurel who supported me all the time and for being always there for me.

Alma

Publications

Journals

1. A. Dudia, J.S. Kanger, and V. Subramaniam, Nanofabricated biomimetic structures for smart targeting and drug delivery, *Nanobiotechnology*, 2005, 1(3), 281-282.
2. A. Dudia, A. Koçer, V. Subramaniam, and J.S. Kanger, Biohybrid polymeric vehicles for controlled drug delivery, *to be submitted*.
3. A. Dudia, A. Koçer, V. Subramaniam, and J.S. Kanger, Biofunctionalized membranes sealing microwells in flat platforms for sensory applications, *to be submitted*.
4. A. Dudia, V. Subramaniam, and J.S. Kanger, Focused ion beam drilling of microwells in polymeric flat substrates, *in preparation*.
5. A. Dudia, V. Subramaniam, and J.S. Kanger, Nanofabricated glass scaffolds for drug delivery applications, *in preparation*.

Peer-reviewed conference proceedings

1. A. Dudia, J.S. Kanger, and V. Subramaniam, Polymeric hybrid microstructures for smart targeting and drug delivery, In *Technical Proceedings of the NSTI Nanotech Conference*, pp. 136-139, Anaheim, CA, USA, 2005. [isbn: 0-9767985-0-6]

Oral presentations

1. A. Dudia, J.S. Kanger, and V. Subramaniam. Nanofabricated biomimetic structures for smart targeting and drug delivery. *The NanoBio-Europe 2005: International Congress & Exhibition on Nanobiotechnology*, Münster, Germany, September 22, 2005 (Invited Talk).
2. A. Dudia, J.S. Kanger, J. Greve, and V. Subramaniam. Polymer based artificial cells as hybrid structures aimed for smart targeting and active drug delivery. *The ALW/FOM/VvBBMT – Meeting on Molecular and Cellular Biophysics*, Lunteren, The Netherlands, September 27, 2004.
3. A. Dudia, J.S. Kanger, and J. Greve. The artificial cell. *The 9th Dutch Annual Conference on BioMedical Engineering*, Papendal, The Netherlands, October 8, 2002.

Other conference contributions

1. A. Koçer, A. Dudia, B. Feringa, W. Meijberg, J.S. Kanger, and V. Subramaniam. Remote Controlled Nanovalve in Flat lipid bilayers. *The NanoNed/MicroNed Symposium II*, Eindhoven, The Netherlands, November 17, 2006 (Book of Abstracts and Oral Presentation).
2. A. Koçer, A. Dudia, B. Feringa, W. Meijberg, J.S. Kanger, and V. Subramaniam. Transmembrane Responsive Systems: Mechanosensitive Channel of Large Conductance, MscL. *The Nano-MicroNed Flagship Meeting*, Groningen, The Netherlands, June 20, 2006 (Oral Presentation).
3. A. Dudia, J.S. Kanger, and V. Subramaniam. An approach to a hybrid artificial cell: nanofabrication and manipulation. *The Annual Dutch Meeting on Molecular and Cellular Biophysics*, Lunteren, The Netherlands, October 10-11, 2005 (Poster Presentation).
4. A. Dudia, J.S. Kanger, and V. Subramaniam. Polymeric hybrid microstructures for smart targeting and drug delivery. *The NSTI Nanotech Conference*, Anaheim, CA, USA, May 8-12, 2005 (Poster Presentation).
5. A. Dudia, J.S. Kanger, and V. Subramaniam. Polymer based hybrid artificial cells as submarines for smart drug delivery. In *Proceedings of the 11th Dutch Annual Conference on BioMedical Engineering*, pp. 146-147, Papendal, The Netherlands, October 4-5, 2004 (Poster Presentation).
6. Z. Zhang and A. Dudia. How to power an artificial cell with nano-sized engines based on biological principles? *The 10th Dutch Annual Conference on BioMedical Engineering*, Papendal, The Netherlands, October 28, 2003 (Oral Presentation: Won great idea award for the best project proposal).
7. A. Dudia, J.S. Kanger, and J. Greve. Polymer nanocontainer: toward an artificial cell. In *Proceedings of the 10th Dutch Annual Conference on BioMedical Engineering*, pp. 77-79, Papendal, The Netherlands, October 27-28, 2003 (Poster Presentation).
8. A. Dudia, J.S. Kanger, and J. Greve. Polymer based micro container: Toward an Artificial Cell. *The European Research Conference on Bionanotechnology*, Granada, Spain, July 9-14, 2003 (Book of Abstracts & Poster Presentation).
9. A. Dudia, J.S. Kanger, and J. Greve. The artificial cell. In *Proceedings of the 9th Dutch Annual Conference on BioMedical Engineering*, pp. 32-34, Papendal, The Netherlands, October 6-7, 2002.

